Passive Characterization of Unknown Spaces Using Large-Volume Pixelated CdZnTe

by

David I. Goodman

A dissertation submitted in partial fulfillment
of the requirements for the degree of
Doctor of Philosophy
(Nuclear Engineering and Radiological Sciences)
in The University of Michigan
2019

Doctoral Committee:

Professor Zhong He, Chair
Dr. Erik Brubaker, Sandia National Laboratory
Professor Jeffrey A. Fessler
Professor Sara Pozzi

David I. Goodman

digoodma@umich.edu

ORCID iD: 0000-0001-8958-5970

To those who took the time to teach me why.

ACKNOWLEDGEMENTS

I joined the Orion Group in 2014 alongside two of the brightest, hardest-working people I have ever known. Bennett Williams and Jiawei Xia have motivated me to put forth my best work and somehow managed to survive my barrage of odd questions. I would like to thank Jiawei in particular for helping conduct several PuBe measurements and Bennett for always making travel more enjoyable. Daniel Shy provided insights into high-energy gamma-ray imaging, with particular focus on event sequencing. I also want to thank friends outside of school, too numerous to list, who have made my nine years as a college student enjoyable.

Progress in the Orion Radiation Measurement Group is built upon the shoulders of many giants. In particular, Dr. Steven Brown not only answered many of my imaging questions when starting graduate school, but more importantly taught me 'why'. Dr. Jiyang Chu helped build my background in the math behind image reconstruction. Dr. Michael Streicher and Dr. Yuefeng Zhu both taught me the physics behind CdZnTe detectors and ensured that research systems were fully functional before experimental campaigns.

Over my brief tenure in the Nuclear Engineering Community I have been lucky to have such caring, and intelligent, mentors. Karen Miller and Eric Flynn from Los Alamos Dynamics Summer School helped provide me with strong research fundamentals on a combined, multidisciplinary project. Erik Brubaker from Sandia National Laboratory helped introduce me to gamma-ray imaging and provided several, useful insights in my thesis. Professor Sara Pozzi and Jeff Fessler were excellent committee

members who provided valuable feedback on monthly reports and group meetings. I also want to thank both David Chichester and Jeff Sanders from Idaho National Laboratory for facilitating plutonium measurements at ZPPR. David also facilitated the interesting measurements using strong, ^{192}Ir and ^{137}Cs sources. Finally, I want to thank Professor Zhong He for making the Orion Research Group so collegial. Without such a friendly, and knowledgeable, environment I would not have learned half as much.

This material is based upon work supported by the National Science Foundation Graduate Research Fellowship Program under Grant No. DGE 1256260 and the Consortium for Verification Technology under DOE NNSA award number DE-NA0002534. Any opinion, findings, and conclusions or recommendations expressed in this material are those of the author and do not necessarily reflect the views of the National Science Foundation nor the DOE.

TABLE OF CONTENTS

LIST OF FIGURES

Figure

LIST OF TABLES

Table

ABSTRACT

Radioactive material is often encountered in unknown configurations across the fields of international safeguards, treaty verification, industry and emergency response. These disparate problems, ranging from small scale, commercial waste classification to wide-spread, post-detonation response, center around the same goal: extracting as much useful information as possible about radioisotopes and their surroundings in some unknown space. These classic nuclear questions of 'who', 'what', 'where', 'why' and 'how' have been asked for many decades. However, recent developments in high-performance, 3-D position-sensitive Cadmium Zinc Telluride (CdZnTe) detectors enable these old questions to be answered in new ways.

Shielding-induced perturbations in photon spectra can be recorded and analyzed to characterize the non-radioactive material around a source. Directional spectra, extracted using either Compton or coded aperture imaging, can characterize complex objects containing multiple, shielded sources. Spectra from strong sources, such as radiological dispersal devices, are similarly perturbed by atmospheric shielding during transport through hundreds of meters of air. Atmosphere-induced, spectral perturbations can be used to estimate standoff and localize sources in 3-D space from a single measurement. Once localized, the effects of solid angle and atmospheric shielding can be corrected for to estimate absolute source activity. Atmospheric scatter, in the form of skyshine, can also be used to localize sources in heavily shielded scenarios without a direct line-of-sight. Strong gamma-ray sources were similarly localized in 3-D space using mobile, helicopter mounted CdZnTe detectors. Direct comparisons between imaging and naïve, non-imaging source localization techniques are made for

these mobile measurements.

Neutron emitting objects, like those encountered in safeguards and treaty verification, can be detected using new, low-noise, digital CdZnTe detectors. Coarse, 1-D fast neutron source localization was demonstrated using a four crystal, CdZnTe array. Gamma rays from neutron-induced interactions were also used to generate a qualitative, spatially-resolved estimate of shielding isotopics.

Finally, high-spatial resolution coded aperture imaging was used to quickly characterize plutonium objects at spatial scales smaller than 1 cm^2. High-energy resolution CdZnTe gamma-ray spectra were then coupled with the commercial software FRAM to estimate special nuclear material isotopics. When combined, these techniques enable spatially-resolved estimation of special nuclear material grade.

CHAPTER I

Introduction

1.1 Motivation

Radioactive material is commonly encountered in unknown configurations. Commercial nuclear power frequently generates low-level, radioactive waste. Low-level waste, often in the form of contaminated, everyday objects, is stored in metal drums [1]. Accurate quantification of total drum radioactivity, which depends on the distribution of both radioactive and non-radioactive waste, is needed to avoid the expensive, over-classification of waste [2]. Overly conservative safety margins, stemming from uncertainties in the spatial distribution of waste, complicate this process. For international safeguards the International Atomic Energy Agency (IAEA) must verify the use of special nuclear materials (SNMs). SNMs, defined collectively as plutonium, ^{233}U and greater than 20% enriched ^{235}U, must be carefully monitored throughout the commercial nuclear fuel cycle due to their potential use in nuclear weapons [3]. However, IAEA safeguards measurements are complicated in realistic measurements where the distribution of radioactive sources, and shielding, are unknown [4, 5]. Attribute-based, dismantlement treaties are similarly complicated by poorly defined source-shielding geometries. For example, detection of four commonly-measured warhead attributes, SNM mass, isotopics, age and symmetry, are affected by shielding [6]. Similarly, the currently accepted definition of warhead dismantle-

ment, the separation of SNM and high-explosives, hinges on accurately verifying the presence, or lack thereof, high-explosives around SNM [7]. Emergency responders face similar problems when determining whether an unknown object contains radioisotopes or explosives. Similar non-radioactive attributes of a radioactive object, like high-explosives, guides subsequent emergency response.

Unknown spaces characterized using radiation signals can span across several orders of magnitude in scale. Most commercial waste classification, international safeguards, treaty verification and emergency-response problems are on the spatial scales of roughly 1 m^3. Contrastingly large, 1 km^3, unknown spaces are commonly encountered after the detonation of a radiological dispersal or improvised nuclear device (RDD/IND). RDD/IND detonations produce very large source terms, up to thousands of curies for a RDD and roughly 10^8Ci/kt at one hour post IND detonation, with complicated contamination fields spanning hundreds-to-thousands of meters [8–11]. Quantitative information on the strength and spatial distribution of these large-scale, radioactive contamination events enables improved emergency response [12, 13].

These disparate problems, ranging from small-scale, commercial waste classification to wide-spread, post-detonation response, all center around the same goal: extracting as much useful information as possible about radioisotopes and their surroundings in some unknown space. In practice, these poorly-defined spaces are typically referred to as 'black-boxes'.

1.2 Overview of Problem

Numerous questions can be posed about black-boxes. In this work, the wide scope is pared down to a few specific questions assuming a radiological source has already been detected. Given that radioactivity has been detected, what isotope is it? Where is it inside the black-box? What potential non-nuclear shielding is around it? And finally, how much is there? These classic nuclear questions of 'who', 'what', 'where',

'why' and 'how' have been asked for many decades. However, the recent development of high-performance, digital, 3-D position-sensitive Cadmium Zinc Telluride (CdZnTe) detectors enables these old nuclear questions to be answered in new ways.

1.3 Contributions of this Work

This thesis focuses on passively probing radioactive black-boxes using state-of-the-art, digital, 3-D position-sensitive CdZnTe detectors. Chapter II discusses the interaction of photons and neutrons with matter alongside how radiation is recorded using 3-D, position-sensitive CdZnTe detectors. It also provides the basic mathematical framework behind the image reconstruction techniques and algorithms used in this work. Chapter III builds on the work by *Streicher et. al* [14] which explores how shielding perturbs recorded, gamma-ray spectra. This shielding characterization framework is extended to directional spectra, extracted using both Compton and coded aperture imaging, and is used to approach realistic problems containing multiple sources in the field-of-view (FOV). Chapter IV discusses how the far-field, atmospheric scatter of gamma-rays from strong, radioactive sources affects recorded spectra. The systematic, energy-dependent downscatter and absorption of photons is then used to estimate source standoff, and therefore activity, from a single-view measurement. Skyshine is also used to localize a source without a direct line-of-sight. Chapter V discusses the localization of strong, radioactive sources using mobile, airborne CdZnTe detectors. Chapter VI builds on the work by *Streicher et. al* [15] which describes how nuclear recoils from fast neutron scatter in CdZnTe are detectable using low-noise, digital, application-specific integrated circuits (ASICs). This work extends simple detection to imaging where rough, 1-D fast neutron source localization is experimentally demonstrated. Chapter VII shows how high-energy, neutron-induced gamma rays can be detected using high-dynamic-range ASICs. Qualitative, spatially-resolved mapping of shielding isotopics is then experimentally demonstrated

in a simple toy problem. Chapter VIII builds on preliminary work by *Streicher et. al* [16] and demonstrates, for the first time, the compatibility of high-resolution, digital CdZnTe system with the commercial software FRAM v5.2 used to estimate SNM isotopics. Chapter IX discusses how high-spatial-resolution, coded aperture imaging techniques pioneered by *Brown* [17] can be leveraged on bright, plutonium objects. Finally, it discusses how coded aperture imaging and FRAM v5.2 can be potentially combined to produce spatially-resolved estimates of material isotopics. Combined, these chapters, which leverage the intrinsic capabilities of digital CdZnTe systems, offer novel and meaningful ways to passively extract information from radioactive black-boxes. Chapter X discusses some additional, tractable problems that can be solved using 3-D, position-sensitive CdZnTe detectors.

CHAPTER II

Radiation Interaction Physics and CdZnTe Detectors

2.1 Radiation Interactions with Matter

Passive characterization of some radioactive, black-box first requires the detection of radiation leaking out of its surface. This thesis focuses on extracting signals from both leaked photons and neutrons across several energy decades. The interaction mechanisms for both photons, from tens of keV to several MeV, and neutrons, from fractions of an eV to several MeV, are discussed below.

2.1.1 Photons

Photons primarily interact with matter via interactions with atomic electrons where the dominant interaction type is controlled by incident photon energy as discussed by [18]. Low-energy photons are primarily absorbed by atomic electrons. After this process, known as photoelectric absorption, the atomic electron is ejected from its shell with energy corresponding to the difference between the incident photon energy and electron shell binding energy. The subsequent vacancy in the electron shell is filled by free or higher orbital electrons. This filling process, using more loosely bound electrons, emits characteristic x-rays with energy corresponding to the differ-

ence between the final and initial electron energy. The energies of emitted x-rays are unique to each element, and can be used to detect the elemental composition of shielding [19]. Relative photoelectric cross sections for elements trend with atomic number Z^n where n varies between four and five.

As photon energy increases Compton scatter overtakes photoelectric absorption to become the predominant photon interaction with matter. In Compton scatter, photons interact with atomic electrons, scattering through some angle θ_{scat}, without depositing their full energy. Neglecting the electron binding energy and assuming a free electron, the incident photon energy E_0, photon scatter angle θ_{scat} and outgoing photon energy E' are correlated through the Compton scatter formula

$$E'(E_0, \theta_{scat}) = \frac{E_0}{1 + \frac{E_0}{m_o c^2}(1 - cos(\theta_{scat}))} \tag{2.1}$$

where the unique, energy-angle relationship can be leveraged by techniques such as Compton imaging [20]. As Compton scatter occurs with atomic electrons, the relative cross section scales with atomic number Z. The relative angular distribution of outgoing, Compton-scattered photons is described by the Klein-Nishina formula [21]. As incident photon energy increases, outgoing, scattered photons become more-and-more forward biased. This preferential, forward scattering can be useful when trying to detect a photon source through a thick, scatter-dominated medium.

Pair production becomes kinematically possible as incident photon energy exceeds the rest mass of two electrons (1.022 MeV). Elemental, pair production cross sections roughly scale with atomic number squared and become comparable to Compton scatter cross sections at several MeV. During pair production, the incident photon is absorbed near the atomic nucleus, producing an electron-positron pair. Excess photon energy is stochastically shared between the newly created electron and positron kinetic energies [22]. The energetic positron and electron slowly lose energy to the

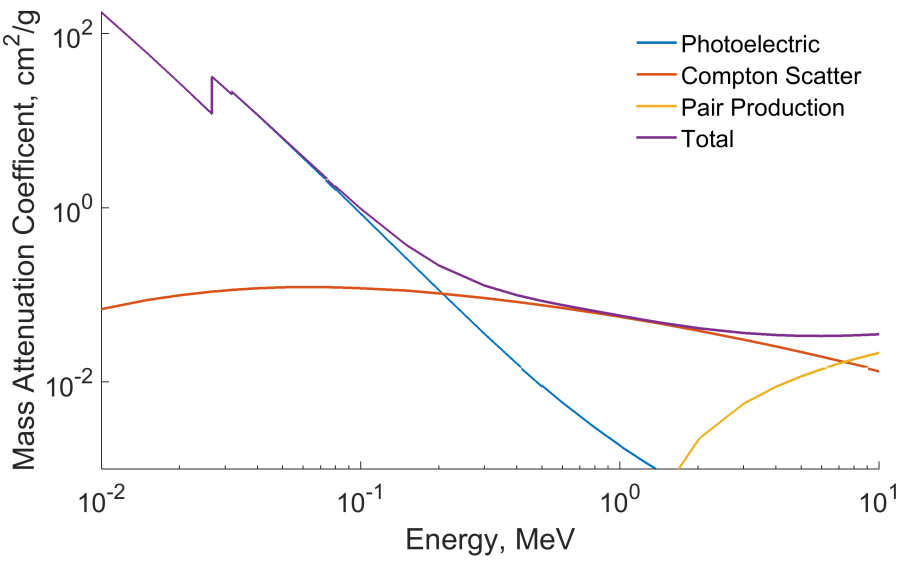

Figure 2.1: Relative CdZnTe mass attenuation coefficients, which are related to individual cross sections through the material density $\rho_{CdZnTe} = 6.1$ g/cm^3, as a function of incident photon energy [89]. Photoelectric absorption is the dominant interaction until ∼200 keV where Compton scatter takes over. The pair production cross section becomes larger than Compton scatter at ∼7.5 MeV.

medium until reaching thermal energies. After thermalization, the newly generated positron annihilates with an electron, producing two, roughly-collinear 511 keV photons. Relative interaction cross sections for CdZnTe, the common, room-temperature radiation detector used in this work, are shown in Fig. 2.1 across a wide energy range of interest.

2.1.2 Neutrons

Neutrons are uncharged particles that, in contrast with photons, interact with the nucleus of an atom. The dominant neutron interaction varies strongly with incident energy. Incident energies can be broken down into two regimes, consisting of fast and thermal neutrons.

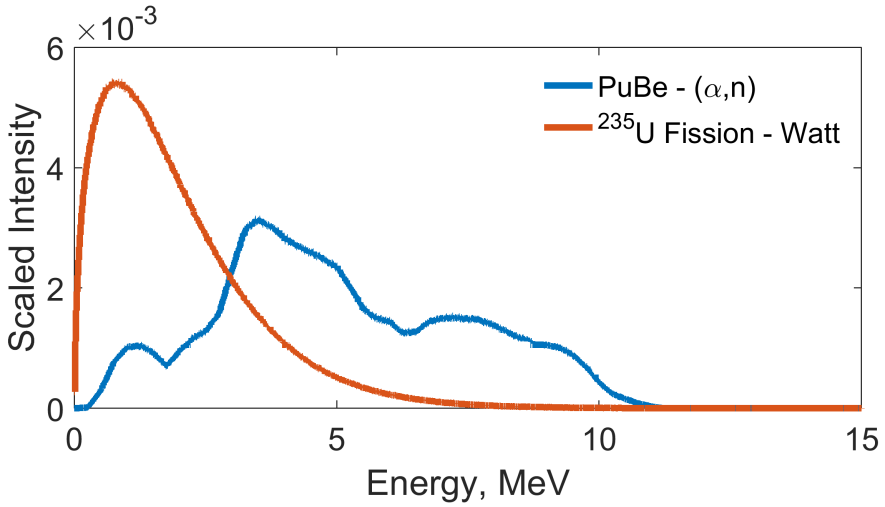

Figure 2.2: Neutron emissions from the fission of ^{235}U and a PuBe (α, n) source. The average energy of the PuBe source exceeds that from fission.

2.1.2.1 Fast Neutrons

Fast neutrons are primarily emitted through fission of nuclear material, such as plutonium and uranium, and (α, n) interactions with low atomic number elements. Other, less prominent neutron production mechanisms, such as photofission, are ignored in this work. Fission neutrons are emitted following a Watt spectrum with an average and most probable energy of roughly 2 and 1 MeV respectively [23]. Furthermore, fission emits multiple neutrons in coincidence with an average emission number of 2.406 for induced fission on ^{235}U [24]. In (α, n) neutron sources, energetic alpha particles penetrate the Coulomb barrier and interact with a low atomic number nucleus, emitting a neutron. Generally, with the exception of interactions in lithium, (α, n) neutrons are emitted with an average energy greater than that of fission [18]. Furthermore, in contrast to fission, (α, n) neutrons are emitted with multiplicity of one. The energy spectra of (α, n) neutrons depend both on the energy of the emitted α particle and energetics, or Q-value, of the reaction. Fig. 2.2 compares the emitted neutron spectra from the fission of ^{235}U and a plutonium-beryllium (PuBe), (α, n) neutron source [25].

Fast neutrons predominantly interact with atomic nuclei through elastic and inelastic scattering. In elastic scatter a neutron scatters off an atomic nucleus, deflecting by some angle θ in the lab frame. The incident neutron energy, E_n, and the kinetic energy of the recoil nucleus, E_R, are related through

$$E_R = \frac{4A}{(1+A)^2} cos^2(\theta) E_n \tag{2.2}$$

where A is the mass number of the scattering nucleus [18]. For a fixed, incident neutron energy and nucleus, the largest possible energy deposition occurs in backscatter where $\theta = 180°$. Furthermore, for high mass number elements, like Cd where $A \simeq 110$, the maximum energy deposited by a single neutron scatter is small at roughly $0.04E_n$. This differs substantially from photons where all, incident energy can be lost in a single interaction.

In inelastic scatter the target nucleus is rearranged into an excited state, absorbing some of the kinetic energy of the incident neutron [24]. The now excited nucleus can de-excite via emission of characteristic gamma rays. The energy of these gamma rays corresponds to the difference between nuclear energy levels traversed by the nucleus during de-excitation. The cross sections for elastic and inelastic neutron scatter both depend strongly on both the scattering nucleus and incident neutron energy. Many resonances, sharp peaks or dips in energy-dependent cross sections, occur when the incident neutron energy matches a discrete, nuclear energy level [26]. Furthermore, there is some threshold energy, corresponding to the differences in nuclear states, required for inelastic neutron scatter below which the cross section vanishes.

2.1.2.2 Slow Neutrons

As fast neutrons propagate through media they lose kinetic energy to the environment through scattering until reaching thermal energies of roughly 0.025 eV. During

this process of thermalization, interactions such as radiative capture (n, γ), where a nucleus absorbs a neutron and emits a gamma ray, or other capture reactions, such as (n, α), become more probable. Generally for low-energy, thermal neutrons the absorption cross sections trends with $1/v$ where v is the incident neutron velocity. This can be explained heuristically as it is proportional to the amount of time a neutron spends within the range of interaction of a nucleus. After capture, the new nucleus may have excessive energy, which is released through the emission of characteristic gamma rays. The energy of these characteristic gamma rays correspond to the differences between nuclear energy levels which are unique to each nucleus. This emission of characteristic gamma rays through neutron interactions can be used to extract isotope-specific information about material around neutron sources in an unknown object.

2.2 Semiconductor Radiation Detectors

Energy resolution, the accuracy with which a detector can measure the incident energy of radiation, is inherently limited by intrinsic, Poisson statistical fluctuations in information carrier generation [18]. As discussed before, photons from radioactive decay, x-rays and neutron capture can be uniquely identified through their unique energy fingerprint. Therefore detectors with good energy resolution are desired to accurately identify the energy, and therefore origin, of recorded photons. Scintillators, a common subset of radiation detectors, are intrinsically limited by the energy-inefficient generation of information carriers through the generation, and subsequent recording of, scintillation light and detector non-proportionality [27]. In contrast, many more information carriers can be generated for the same deposited energy in semiconductor-based detectors with excellent proportionality across a wide energy range. Therefore, semiconductor detectors are commonly used for high-performance radiation measurements where energy resolution is critical.

Common semiconductor-based radiation detectors are made of silicon and ultra-pure germanium. Silicon based detectors are typically thin, with low atomic number $Z = 14$, limiting their use to predominately low-energy photon and charged particle detection. Ultra-pure germanium detectors, known as high purity germanium (HPGe), have higher relative atomic number, $Z = 32$, moderate density, $\rho = 5.3$ cm^3, and can be manufactured large enough to offer appreciable efficiency in high-energy, photon detection [18]. Furthermore, HPGe detectors provide the 'gold-standard' in energy resolution, offering roughly 0.2-0.3% full-width-at-half-maximum (FWHM) at 662 keV, for fieldable, coaxial detectors [28]. However, HPGe detectors must be cooled to liquid nitrogen temperatures for operation due to the small band gap between the conduction and valance band. This cooling, whether accomplished through liquid nitrogen or mechanical means, greatly complicates the in-field deployment of HPGe detectors.

CdZnTe, a room-temperature, ternary semiconductor, is an attractive alternative to HPGe. CdZnTe is denser, $\rho = 6.1$ cm^3, and has a larger effective atomic number, $Z_{\text{eff}} = 50$, such that it has higher, intrinsic photon detection efficiency than HPGe for the same detector volume [29]. Room temperature operation without cryogenic cooling greatly simplifies measurement logistics behind the in-field use of CdZnTe relative to HPGe. Furthermore, bulky cryogenic cooling systems place a lower-floor on the effective weight of fieldable, HPGe-based detector systems. This size and weight floor further limits the practical use of large, HPGe-based systems in many applications. Furthermore, recent improvements in CdZnTe crystal growth and readout have drastically closed the historical gap between CdZnTe and HPGe energy resolution and efficiency [30]. As such, this work focuses on leveraging, 3-D position-sensitive CdZnTe detectors systems across a wide, black-box, problem space.

2.2.1 Detection of Radiation Ionization Events

The process from radiation interaction to event readout in a semiconductor-based, radiation detector is described below.

2.2.2 Charge Induction

When radiation interacts in a semiconductor, it generates electron-hole pairs in the material conduction and valence bands respectively. Detectors are biased such that generated, electron-hole pairs immediately drift through the detector bulk. The motion of these charge carriers, not the final collection at electrode surfaces, is what generates electrical signals read out at each respective electrode. Induced charge on detector electrodes by moving charge is explained by the Shockley-Ramo Theorem [31, 32]. When radiation interacts in a semiconductor detector, the total induced charge on an arbitrary electrode from drift of N charge carriers is

$$Q = \sum_{j=1}^{N} -q_j(\phi_0(\boldsymbol{x}_{f,j}) - \phi_0(\boldsymbol{x}_{i,j})) \tag{2.3}$$

where q_j is the charge of the j^{th} carrier (-1/+1 for electrons and holes respectively) and $\phi_0(\boldsymbol{x}_{i,j})$ and $\phi_0(\boldsymbol{x}_{f,j})$ are the corresponding weighting potentials at the beginning and end of the j^{th} carrier's drift from spatial position $\boldsymbol{x}_{i,j}$ to $\boldsymbol{x}_{f,j}$. For a given semiconductor, the number of generated electron-hole pairs is linearly-related to the deposited photon energy through the ionization energy [18]. Detailed discussion on the concept of weighting potential for radiation detectors is provided in [33]. Total induced charge Q is recorded on an event-by-event basis and histogrammed to form energy spectra. In a perfect detector the total induced charge Q is proportional to only the number of generated charge carriers N. If both electrons and holes are fully collected, the combined change in weighting potential for each electron-hole pair is one. In CdZnTe, however, only electrons drift through a non-negligible change

in weighting potential due to severe hole trapping [34]. Furthermore, electrons are stochastically trapped by crystal defects, such as grain boundaries or tellurium inclusions, while drifting towards the anode. Combined, these effects cause the induced charge Q to be a function of both the number of generated charge carriers N and the mean change in weighting potential traversed by electrons which is a strong function of drift distance, degrading estimates of incident gamma-ray energy. Luckily, the electron drift distance dependence on induced charge can be mitigated through careful design of electrode geometry.

Single-polarity charge sensing detectors are designed to be insensitive to the movement, or lack thereof, of holes. Historically Frisch or coplanar grid systems were used to mitigate the influence of holes in CdZnTe using simple readout techniques [35, 36]. Lack of hole movement can be similarly ignored using detectors instrumented with a large array of small, pixelated anodes and a planar cathode [37]. For pixelated detectors, the anode weighting potential changes rapidly within one pixel pitch of the anode, and relatively slowly towards the cathode. This causes the majority of charge induction to occur right by the anode surface. As electrons from all events, independent of depth, drift through this anode layer the magnitude of induced charge is effectively decoupled from electron drift distance. Furthermore, electronic noise from electrode capacitance, which is another factor that fundamentally limits detector energy resolution, is smaller for pixelated readouts than coplanar grids due to the smaller footprint of individual electrodes.

However, pixelated anode geometries are not without shortcomings. Each pixelated anode and the planar cathode must be independently read out and processed. For common pixelated CdZnTe detector layouts this corresponds to roughly 120 channels. Readout complexity has been largely mitigated with the introduction of ASICs [38]. As such, the entirety of work in this thesis was conducted using pixelated CdZnTe detectors.

2.2.3 3-D Position-Sensitive CdZnTe

A common CdZnTe crystal form factor of 2 x 2 x 1.5 cm^3 was used in this work. Each detector was instrumented using an array of 11 x 11, pixelated anodes and a large, planar cathode. Detector anodes are pixelated to leverage the 'small-pixel effect', where the amplitude of electron-drift-induced charge on anode channels is proportional to deposited energy and independent of interaction depth [37]. Contrastingly, the amplitude of induced charge on the large, planar cathode is proportional to the product of deposited energy and interaction depth. Taking the ratio of the these two signals enables estimation of interaction depth [39]. Combined with lateral position-sensing from pixelated anodes, a 3-D gain correction can be applied to recorded, voxel-by-voxel gamma-ray spectra to align the detector-wide spectrum and correct for material non-uniformity. Notably this correction only aligns voxelized, photopeak centroids and is intrinsically limited by the variance within each individual voxel. Crystals are commonly arrayed together in coincidence to increase system sensitivity. A typical 3 x 3 array, the common layout of most systems used in this work, is shown in Fig. 2.3.

Signals induced on electrodes are read out using digital ASICs [30]. Induced anode and cathode waveforms for photopeak, ^{137}Cs gamma rays are shown in Fig. 2.4 where the shape of anode and cathode weighting potentials are clearly visible. Single-pixel resolutions of less than 0.4% FWHM at 662 keV are achievable by directly attaching high-quality, Redlen CdZnTe crystals to recent, VAD_UMv2.2 digital ASICs as shown in Fig. 2.5. CdZnTe crystals are directly mounted to readout ASICs to improve energy resolution by reducing capacitance between the detector and preamplifier [40]. Lateral interaction position can be estimated to better than 300 μm at 662 keV, smaller than the anode pixel pitch, using transient signals on neighboring anode pixels [30]. With the 3-D position and deposited energy of gamma-ray interactions in CdZnTe, the incident direction of radiation can be estimated using a variety of imaging modalities.

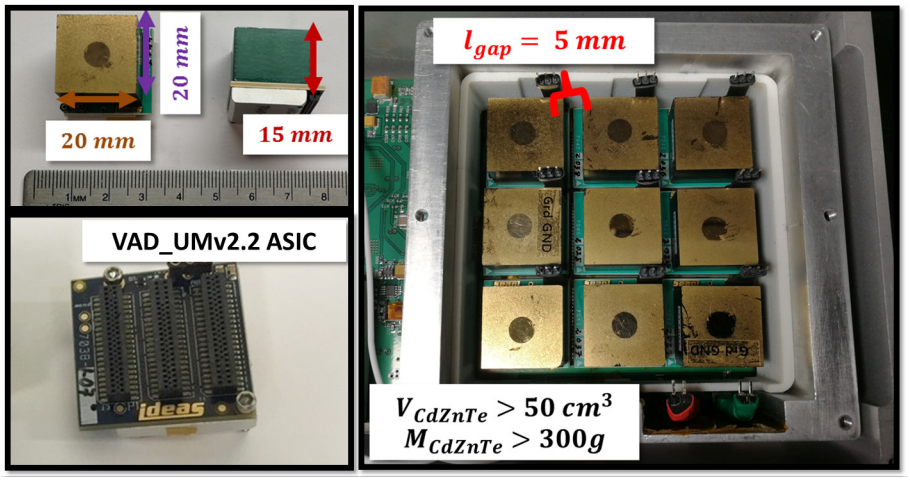

Figure 2.3: (Top left) Typical CdZnTe crystals are 2 x 2 x 1.5 cm^3. (Bottom left) Each crystal is readout via an ASIC. The current, state-of-the-art VAD_UMv2.2 ASIC directly mounts to CdZnTe crystals, without an interposer board, to help reduce electronic noise. (Right) A 3 x 3 array of CdZnTe crystals in Orion Beta. The gap between detectors varies from 2 to 5 mm between systems. Cumulative CdZnTe volume and mass are greater than 50 cm^3 and 300 g respectively.

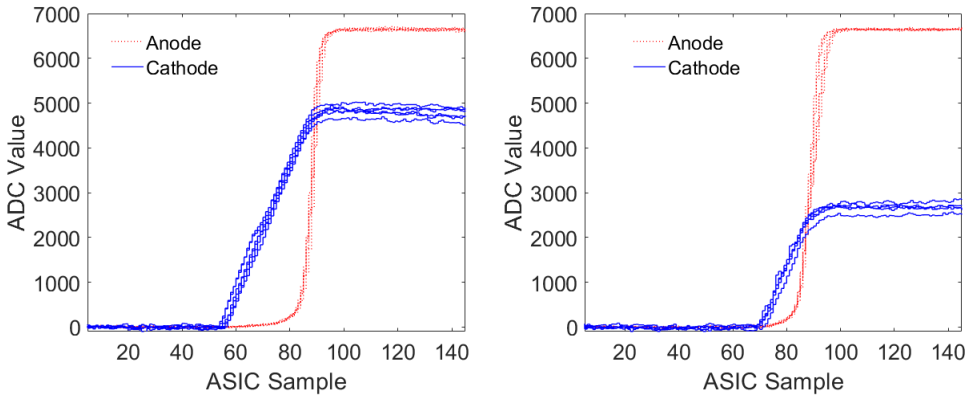

Figure 2.4: Anode (red) and cathode (blue) waveforms for ^{137}Cs photopeak events near the cathode (left) and anode (right) where electron clouds drift through 75% and 40% the detector respectively. Note that cathode amplitude changes with depth while anode amplitude is relatively depth-independent. The ASIC sampling rate is 80 MHz.

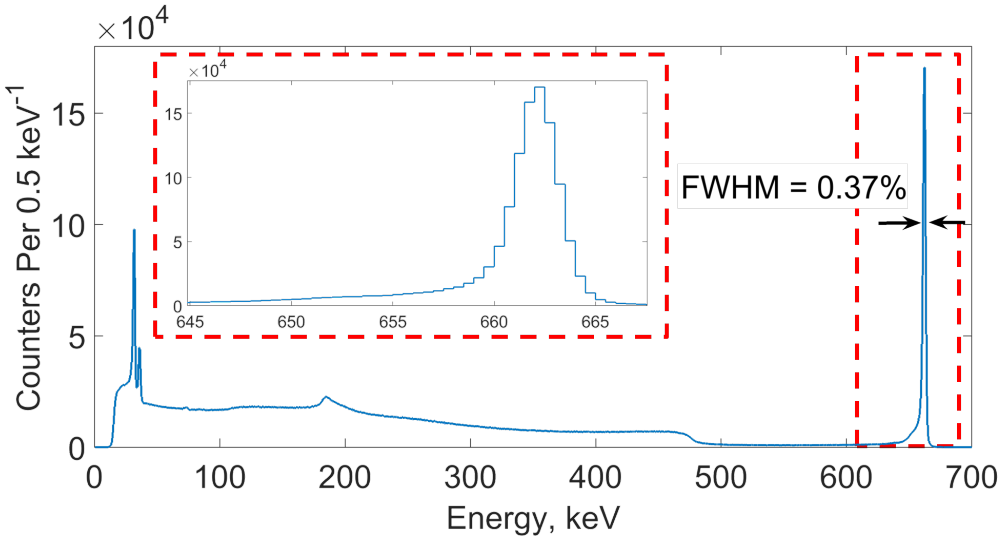

Figure 2.5: Voxelwise, gain-corrected, single-pixel ^{137}Cs spectra from a direct-attached, 2 x 2 x 1.5 cm^3 CdZnTe crystal with 0.37 % FWHM. The inset region in red emphasizes photopeak shape with moderate, low-energy tail stemming from the pixelated readout.

2.3 Radiation Imaging

2.3.1 Imaging Model

Radiation imaging centers around estimating the spatial distribution of some unknown, radioactive source. Imaging problems can be described in matrix-form by

$$\bar{\boldsymbol{g}} = \boldsymbol{T}\boldsymbol{f} \tag{2.4}$$

where $\boldsymbol{f}$ is a length J vector representing the source distribution discretized into image elements, pixels in 2-D or voxels 3-D, $\bar{\boldsymbol{g}}$ is some expected length I observation vector and $\boldsymbol{T}$ is the I by J system matrix that maps between the source and observation space. The system matrix can be considered more intuitively when considering a single row corresponding to event i. The j^{th} column of the i^{th} row, t_{ij}, represents the conditional probability that given a photon was emitted from image element j, what is the probability it is detected as event type i. Given some measurement $\boldsymbol{g}$, which is a sample of expected observation vector $\bar{\boldsymbol{g}}$, there are many ways to estimate of $\boldsymbol{f}$.

2.3.1.1 Simple-Backprojection

If the system matrix $\boldsymbol{T}$ is easily invertible, and there is negligible statistical noise, the estimation problem becomes trivial. However for radiation detectors the system matrix $\boldsymbol{T}$ is not always easily invertible. Furthermore, there are often far fewer observations in $\boldsymbol{g}$ than the J unknowns in the imaging space. Without sufficient information this inversion process can become ill-posed.

Simple-backprojection (SBP) is one naïve imaging approach that uses the system matrix $\boldsymbol{T}$ in estimating $\hat{\boldsymbol{f}}_{\boldsymbol{SBP}}$. Heuristically the simple-backprojection estimate can be thought of as the summation of system matrix rows weighted by the number of observations for each row. Mathematically, this process can be thought of as using the system matrix transpose $\boldsymbol{T}^\top$

$$\hat{\boldsymbol{f}}_{\boldsymbol{SBP}} = \boldsymbol{T}^\top \boldsymbol{g} = \boldsymbol{T}^\top \boldsymbol{T} \boldsymbol{f}. \tag{2.5}$$

Fig. 2.6 show the process of backprojection and summation of Compton cones to the image plane for a single point source using a CdZnTe system. However, this simple-backprojection estimate, $\hat{\boldsymbol{f}}_{\boldsymbol{SBP}}$, does not produce an unbiased estimate of the point source $\boldsymbol{f}$ as

$$\boldsymbol{T}^\top \boldsymbol{T} \neq \boldsymbol{I} \tag{2.6}$$

where $\boldsymbol{I}$ is the identity matrix. For example, the overlap of many Compton cones reconstructed for the same point source produces an image with non-zero, spatial spread. The shape of this imaging spread, known as the point spread function (PSF), is system-dependent and typically blurs reconstructed images. Contrastingly, Fig. 2.6 also shows a simple-backprojection reconstruction using the coded aperture imaging modality. The attenuative mask elements were placed following a modified, uniformly redundant array (MURA) mask pattern such that $\boldsymbol{T}^\top \boldsymbol{T}$ approaches an identity matrix [41]. As such, the point source is reconstructed on a uniform background with little

additional blur beyond the size of projected elements used in the mask.

For some simple, sparse problems discussed in this thesis, the blur from SBP reconstruction is acceptable. However, the effect of this blur is particularly severe for some non-sparse scenes, where there are spatially extended, or multiple point sources, encountered in this thesis. Given sufficient measurement statistics, or prior information on the shape of $\boldsymbol{f}$, intrinsic system blur can be deconvolved out using a variety of techniques such maximum-likelihood, filtering or Bayesian approaches [42–44]. In this thesis system blur in Compton images is deconvolved using a well-known, maximum-likelihood-based approach.

2.3.1.2 Maximum-Likelihood

Maximum-likelihood-based approaches, in general, attempt to solve for the 'most-likely' source distribution given some observations and underlying Poisson detection physics. Derivation of maximum-likelihood-based approaches can be succinctly described following a detailed outlined provided by *Chu* [55]. More detailed derivations can be found elsewhere [45]. Assume the number of experimental observations of event type i is drawn from the Poisson distribution with mean $\bar{g}_i$. Given I possible event types then the logarithmic likelihood, that is maximized when considering possible source distributions $\boldsymbol{f}$, is

$$\mathcal{L}(\boldsymbol{g}|\boldsymbol{f}) = ln(\prod_{i}^{I} P(g_i|\boldsymbol{f})) = \sum_{i}^{I} ln(P(g_i|\boldsymbol{f})). \tag{2.7}$$

For practical measurements using 3-D, position-sensitive CdZnTe system the measurement vector $\boldsymbol{g}$ is too large for tractable, analytic solutions to Equation 2.7 [46]. For example, a nine detector CdZnTe array with 40 depth bins, 121 anode pixels and sub-pixel resolution factor of seven yields $(9 \cdot 40 \cdot 121 \cdot 7^2)^2 \simeq 4.5 \cdot 10^{12}$ possible, two-pixel event Compton rings for a given photon energy. As such, instead of storing

some incredibly large, sparse vector $\boldsymbol{g}$ individual events are stored in list-mode format [47,48]. The incredibly large, sparse system matrix $\boldsymbol{T}$ is now replaced by $\tilde{\boldsymbol{T}}$ which is built on an event-by-event basis. Each row corresponds to the pixel-wise likelihood an event emitted from each image element was recorded as event type i. The size of $\tilde{\boldsymbol{T}}$ is now I by J where I is the total number of imagable events in a measurement over J image elements. List-mode maximum-likelihood expectation-maximization (MLEM) problems can be solved iteratively using the technique pioneered by Richardson and Lucy [49, 50]

$$f_j^{n+1} = \frac{f_j^n}{s_j} \sum_{i=1}^{I} \frac{t_{ij}}{\sum_{k=1}^{J} t_{ik} f_k^n} \tag{2.8}$$

where f_j^n is the intensity estimate of image pixel j during iteration n, t_{ij} is the probability of recording event i given the photon was emitted from image element j, s_j is the system sensitivity to events emitted from image element j given J image elements and I total events. Although the relative likelihood of the maximum-likelihood solution $\hat{\boldsymbol{f}}_{\boldsymbol{MLEM}}$ increases with every MLEM iteration, a general stopping criterion is difficult to choose [51, 52].

In general, the MLEM deconvolution process amplifies high-frequency noise in source reconstruction. Careful consideration must be given between balancing deconvolution of system blur, which improves with iteration number, and unwanted amplification of high frequency noise with increasing iteration. For example, this high-frequency noise typically manifests itself in CdZnTe-based Compton images as salt-and-pepper noise which complicates the localization of point sources and margins of extended objects. In practice, somewhere between 10 and 25 MLEM iterations has been heuristically chosen as a reasonable trade-off between deconvolution of system blur and amplification of high-frequency noise using 3-D, CdZnTe systems [42, 53].

Many techniques exist to mitigate the amplification of high-frequency noise through the deconvolution process. Regularized maximum-likelihood-based reconstructions

have been developed to penalize non-sparse or non-smooth solutions using L_0, L_1 and L_2 penalties [54]. Similar sparseness and smoothness promoting priors have been developed for Bayesian based reconstructions. Measurement statistics-based filters have been implemented for direct inversion based techniques such as filter-backprojection [55]. These filters more aggressively deconvolve system blur, increasing system resolution, with increasing measurement statistics as the problem becomes better-posed.

2.3.2 Imaging Modalities

Photons are imaged using different modalities depending on their incident energies.

2.3.2.1 Compton Imaging

Photons that Compton scatter and are subsequently absorbed in a detector can be localized through electronic collimation first proposed by *Todd et. al* [155]. This process, known as Compton imaging, reduces possible incident photon directions to the surface of a cone with opening angle determined via Compton kinematics as shown in Fig. 2.6. Due to rotational symmetry, significant ambiguity exists in incident source direction for a single photon. This rotational ambiguity in incident, photon direction can be reduced to some angular subset of a cone by tracking the recoil electron [56, 57]. However, electron tracking is not yet feasible in the CdZnTe systems used in this work. Reconstructing many Compton cones generated by photons from the same spatial location produces a hot spot at the source location. Compton imaging is a mature, commercially-available imaging technique in CdZnTe detectors that can be readily leveraged to extract information from unknown spaces [46, 58].

2.3.2.2 Coded Aperture

Low-energy photons do not Compton scatter in high-Z radiation detectors and therefore, cannot be localized using Compton imaging. However, low-energy photons are readily attenuated by high-Z materials. Low resolution estimates of incident photon direction can be made by recording the attenuation of photons across multiple, or within a single, position-sensitive detector [59–61]. Incident fast neutron direction can be similarly estimated by the attenuation of neutron interactions across a detector [62].

Source localization precision is typically limited using only detector attenuation. Detailed source location can be estimated by selectively placing attenuating media between the radioactive source and detector. By removing one region of the attenuator, similar to a pinhole camera, source distributions can be directly estimated by projecting recorded counts from the detector plane through the opening. Multiple holes can be added to the attenuator to increase imaging efficiency at the expense of reconstruction complexity stemming from the ambiguity over which hole a recorded photon passed through [63]. By carefully arranging mask openings, such as using a modified, uniformly redundant array (MURA) pattern, perfect reconstruction quality is still theoretically achievable using multiple mask holes [41]. Coded aperture reconstructions are conducted in a manner similar to that of a pinhole, where recorded detector counts are projected through all open mask elements. Several MURA-based coded aperture systems have been developed and deployed for 3-D, position-sensitive CdZnTe systems [64, 65]. Several mature, commercial coded aperture gamma-ray imaging systems are also available [66, 67]. An example coded aperture reconstruction of a point source is shown in Fig. 2.6.

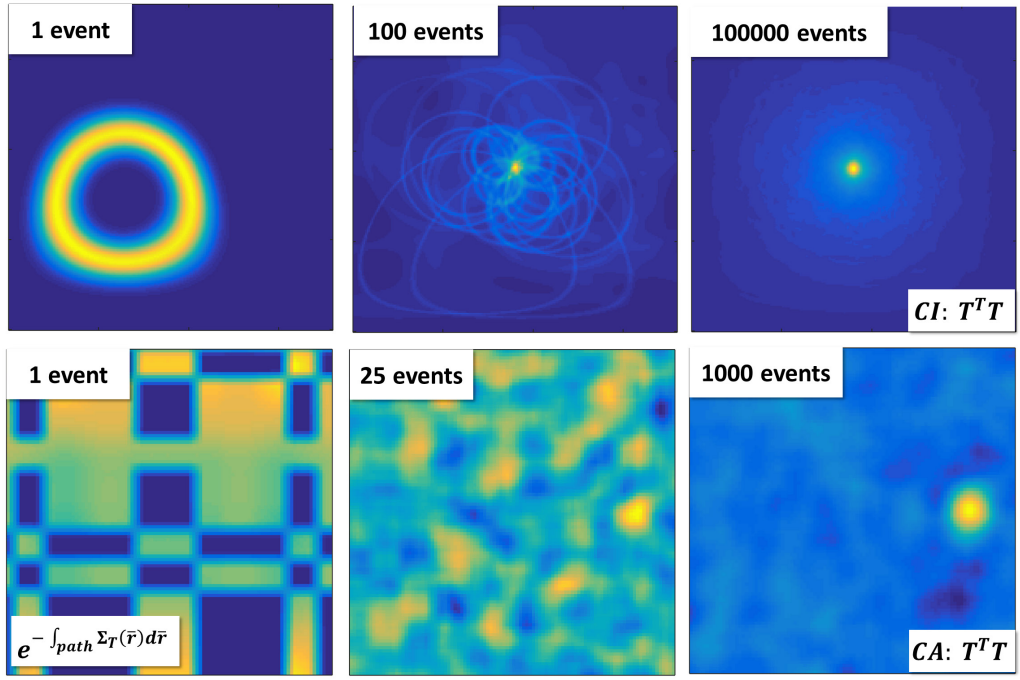

Figure 2.6: (Top) Simple-backprojection of high-energy photons using Compton imaging. When a photon of known energy interacts twice in a detector, its incident direction can be localized to the surface of a cone. Non-zero cone width results from limited detector position and energy resolution on an event-by-event basis [68]. Cones reconstructed from photons emitted at the same point in space will overlap, forming a blurred hot spot. (Bottom) Low-energy photons emissions can be localized through coded aperture imaging where the shadow of some attenuative mask is recorded on a detector. A sample reconstruction for a rank 19 MURA mask, similar to that used in Polaris II, is shown. Detected photons are more likely to have streamed through open mask elements. Event responses are reconstructed by back-projecting ray-traced attenuation probabilities back to imaging space. Given many recorded events the orthogonal nature of the MURA pattern becomes apparent. Slight deviations from perfect image reconstruction stem from detector pixelation and gaps. With sufficient statistics the simple-backprojection reconstructed images, independent of imaging modality, have the shape $\boldsymbol{T}^\top \boldsymbol{T} \boldsymbol{f}$. The non-identity matrix shape of $\boldsymbol{T}^\top \boldsymbol{T}$, as $\boldsymbol{f}$ is a point source, is clearly evident in Compton imaging.

CHAPTER III

Angular Shielding Detection

3.1 Gamma-Ray Based Shielding Characterization

Unshielded, radioactive material is rarely found in practical, in-field measurements. Realistic, poorly-defined, source-shielding geometries modulate the energy and intensity of emitted source photons and neutrons. Accounting for this shielding-dependent modulation is critical for accurate, quantitative measurement of SNMs [4, 5]. Many techniques, such as GADRAS and others, exist to characterize unknown shielding from measured, gamma-ray spectra [69, 70]. *Streicher et. al* proposed and implemented a simple, alternative technique to cheaply characterize unknown shielding using the energy dependent modulation of photopeak ratios and foward-angle, Compton scatter [14]. Effective shielding atomic number, Z, and areal-thickness, ρx, can be estimated by comparing the observed, energy-dependent modulation of photopeak ratios and forward-angle Compton scatter against a library of plausible shielding combinations. A brief outline of the technique developed by *Streicher et al.* is provided below.

Gamma rays are exponentially attenuated by shielding material. Given the emission of gamma rays with energy E_1 and E_2, the attenuated fluxes through shielding

of thickness x are calculated as

$$I_1 = I_1^0 e^{-(\frac{\mu}{\rho})_1 \cdot \rho x}, \qquad I_2 = I_2^0 e^{-(\frac{\mu}{\rho})_2 \cdot \rho x} \tag{3.1}$$

where I_1^0 and I_2^0 are the initial fluxes, μ_1 and μ_2 are the shielding linear attenuation coefficients at each energy, x is the thickness of intervening material and ρ is the shielding density [18]. Given tabulated cross sections for each element, mass attenuation coefficients $(\frac{\mu}{\rho})_{2,Z}$ and $(\frac{\mu}{\rho})_{1,Z}$ can be calculated. Residuals between measured and predicted photopeak ratios can be calculated via

$$r^2_{\rho x,Z} = \left[\ln(\frac{I_1}{I_2}) - \ln(\frac{I_1^0}{I_2^0}) - \left[(\frac{\mu}{\rho})_{2,Z} - (\frac{\mu}{\rho})_{1,Z} \right] \rho x \right]^2 \tag{3.2}$$

as a function of hypothetical mass thickness ρx and element Z. N peak ratio residuals can then be combined into a single metric to enhance estimator quality via

$$R^2_{\rho x,Z} = \sum_{k=1}^{N} \frac{{r_{\rho x,Z,k}}^2}{\sigma_k^2} \tag{3.3}$$

where $r_{\rho x,Z,k}$ is the k^{th} photopeak ratio residual with propagated variance σ_k^2.

3.1.1 Small-Angle Compton Scatter

Gamma rays undergo small-angle Compton scatter in shielding with probability dictated by the Klein-Nishina formula [21]. The probability that a gamma ray small-angle-scatters in shielding of thickness D and is subsequently detected can be broken down into individual components. First, the small-angle-scatter must occur. Second, the outgoing scatter angle $d\Omega$ about Ω must fall in directions subtended by the detector. Third, the outgoing gamma ray must exit the object without subsequent interaction. Assuming the material cross section is roughly the same before and after

scatter, these three terms are combined and simplified as

$$P_C = e^{-\mu_t D} \int_0^D \mu_t dx \int_{\mathbf{\Omega_D}} \frac{1}{\sigma_t} \frac{d\sigma_c}{d\Omega} d\Omega \tag{3.4}$$

where μ_t is the shield linear attenuation coefficient, σ_t is the total interaction cross section, $\mathbf{\Omega_D}$ is the subset of detectable scatter angles and $\frac{d\sigma_c}{d\Omega}$ is the Klein-Nishina cross section [14]. Comparing this to the probability of a photon being unattenuated, P_U, yields

$$\frac{P_C}{P_U} = \mu_t D \frac{1}{\sigma_t} \int_{\mathbf{\Omega_D}} \frac{d\sigma_c}{d\Omega} d\Omega \propto \rho D \frac{Z}{uA} \tag{3.5}$$

where A is the relative shielding atomic number and u is the atomic mass unit. Note the final simplification is possible as the Klein-Nishina cross section is approximately proportional to the effective atomic number of the shield [14]. The probability of small-angle-scatter relative to unattenuated, photopeak flux is measured in spectra via

$$\frac{P_C}{P_U} = \frac{(A_C - B) - \beta(A_{PP} - B)}{A_{PP} - B} \tag{3.6}$$

where A_C is the gross, small-angle-scatter counts, A_{PP} is gross, photopeak counts, B is background counts and β is a system-dependent, self-small-angle-scatter correction that is subtracted off. In practice, β stems from both scatter in the non-detector volume of the CdZnTe system and low energy tailing from true, non-scattered, photopeak gamma rays due to the pixelated readout.

Compton scatter residuals can be similarly calculated by computing the squared difference between the measured ratio of small-angle-scatter and unattenuated gamma-rays to the expected ratio as a function of hypothetical shielding mass thickness and atomic number using tabulated data. Compton scatter residuals are then combined with photopeak ratio residuals to estimate Z and ρx of the intervening, shielding material in a measurement. Regions of low, residual fits across both photopeak and

scatter ratios implies plausible shielding configurations. This is demonstrated in Fig. 3.1 for a 1.3 cm tin-shielded, ^{133}Ba source. The lowest, combined residual fit from photopeak attenuation and Compton scattering is chosen as the best estimate of shielding thickness and atomic number.

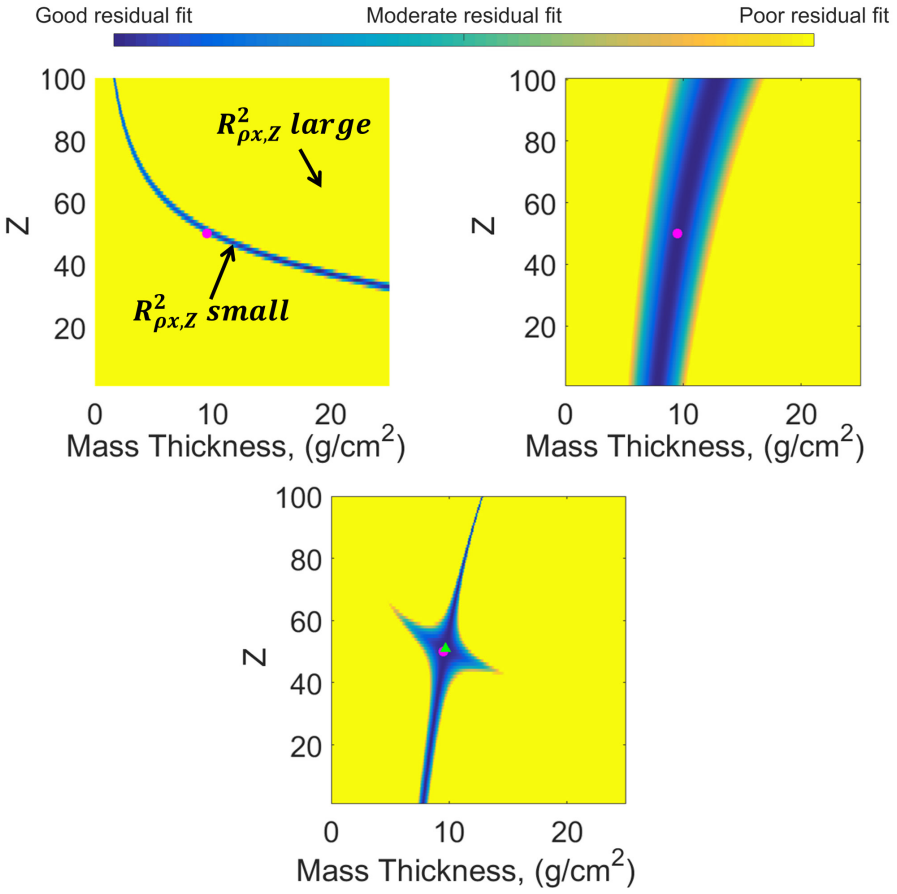

Figure 3.1: Photopeak ratio (left), small-angle Compton scatter (right) and combined (bottom) residual fits calculated using the spectrum of a ^{133}Ba source shielded by 1.3 cm of tin. Note the complimentary information contained in photopeak and Compton scatter residuals. Colormaps are independently scaled between images to maintain contrast. True shielding parameters are marked with a magenta dot while the best estimate from combined photopeak and Compton scatter residuals is labeled with a green triangle.

The simple technique discussed in [14] works in sparse measurement scenarios, where there is only one gamma-ray source, but fails for scenarios where multiple sources are shielded by distinct materials. In realistic cases containing multiple

sources distinct, gamma-ray spectra leak out from each shielded source. A linear combination of the distinct spectra, scaled by source strengths and absolute efficiencies, is measured by the detector. The resulting, 'angularly-integrated' spectra is not indicative of any of individual shielding parameters, severely hindering any characterization. Unwanted angular integration, however, can be mitigated through the use of gamma-ray imaging.

3.2 Angularly Resolved Gamma-Ray Spectra

Naïve photon detectors angularly integrate all spectra from multiple, shielded sources into one, cumulative gamma-ray spectrum. Gamma-ray imaging spectrometers undo this unwanted angular integration, returning directional spectra, enabling directional shielding characterization. As discussed in Chapter II, different imaging modalities are used for different energy photons. Recent effort has been made to use GADRAS to estimate directional spectra using CdZnTe imaging spectrometers [71]. However, these directional spectra have not been explicitly used to characterize directional shielding. Directional shielding characterization, using both Compton and coded aperture imaging, is presented below.

3.2.1 Shielding Characterization of Multiple ^{133}Ba Sources via Compton Imaging

^{239}Pu emits gamma rays across a wide energy range from roughly 40-800 keV [24]. Low-energy plutonium photons, from roughly 40-120 keV, are completely attenuated by even moderate shielding. High-energy plutonium gamma rays, from 600-800 keV, are emitted with relatively low intensity. In contrast, medium-energy plutonium gamma rays, from 330-420 keV, are relatively bright, penetrative emissions that can be used to characterize shielding. Medium-energy, plutonium gamma rays are also readily Compton-imagable. ^{133}Ba is a common surrogate used to mock moderate-

energy, plutonium gamma rays [72, 73]. As such, shielded ^{133}Ba sources were used to mock scenarios containing heterogeneously shielded plutonium. The following summarizes the work presented in *Goodman et. al* [74].

3.2.1.1 Measurement Geometry

A 90 μCi ^{133}Ba source was placed 38 cm above the cathode side of the CdZnTe detectors at two locations corresponding to $(\theta, \phi) = (90°, 90°)$ and $(\theta, \phi) = (139°, 108°)$ in polar coordinates. In this coordinate system, $(\theta, \phi) = (90°, 90°)$ corresponds to the direction perpendicular to the cathode. Plates of various thickness and elemental composition were then placed between the source and detector in addition to the bare cases as shown in Fig. 6.5. Plate shields were placed directly under the sources such that roughly all scatter angles less than 180° were possible while source-to-detector distance was kept roughly constant. Bare sources were measured for 8 hours while shielded sources were measured for 16 hours. Measurements were linearly combined to mimic the simultaneous measurement of multiple sources; individual count rates were low enough such that differences in dead time and system performance were small when combining measurements. Individual measurement spectra illustrating modulation of peak ratios and small-angle Compton scatter are shown in Fig. 3.3.

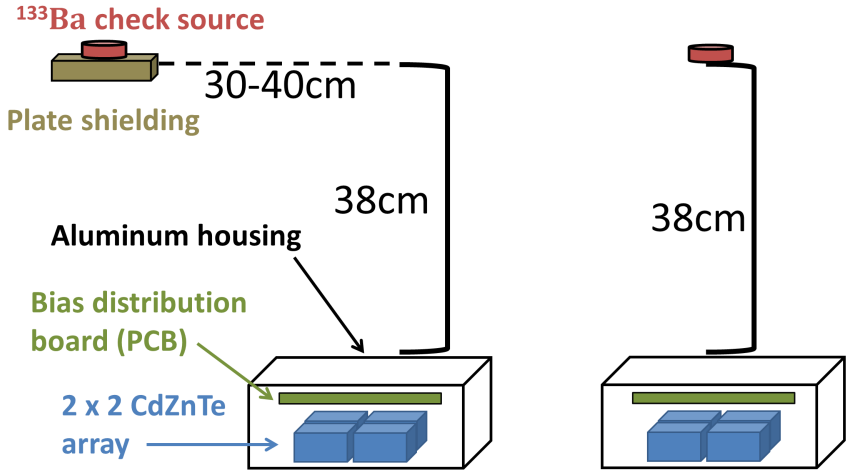

Figure 3.2: (Left) Measurement schematic for shielded sources. Plate shielding was placed directly under the source to insure the detector was fully shielded. Note the non-negligible amount of scattering material in the detector housing and bias distribution boards contributing to system, self-small-angle-scatter β. (Right) Measurement schematic for bare sources.

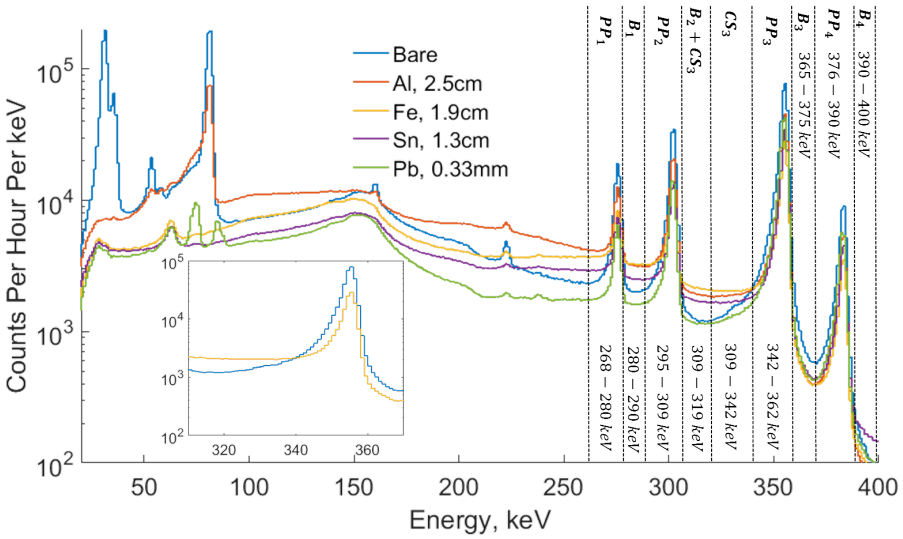

Figure 3.3: Measured ^{133}Ba spectra for several shielding configurations. The boxed inset emphasizes the relative ratio between small-angle scatter and photopeak counts for the bare and iron measurements. Note the iron continuum is larger, from small-angle scatter within the shield, even though the bare photopeak has more counts. Photopeak, small-angle Compton scatter and background energy bins were labeled PP, CS and B respectively for each subscripted photopeak number.

A MLEM algorithm, as described in Chapter II, was used to reconstruct direc-

tional spectra. MLEM was chosen over simple-backprojection to mitigate spectral crosstalk between neighboring sources. An illustration comparing reconstructed images for a sample ^{133}Ba measurement is shown in Fig. 3.4. Simple-backprojection hot spots have non-zero, off-source direction tails. A second, reconstructed source hot spot is superimposed on top of these tails, systematically biasing estimates of directional spectra. This spectral crosstalk is less severe in the MLEM reconstruction.

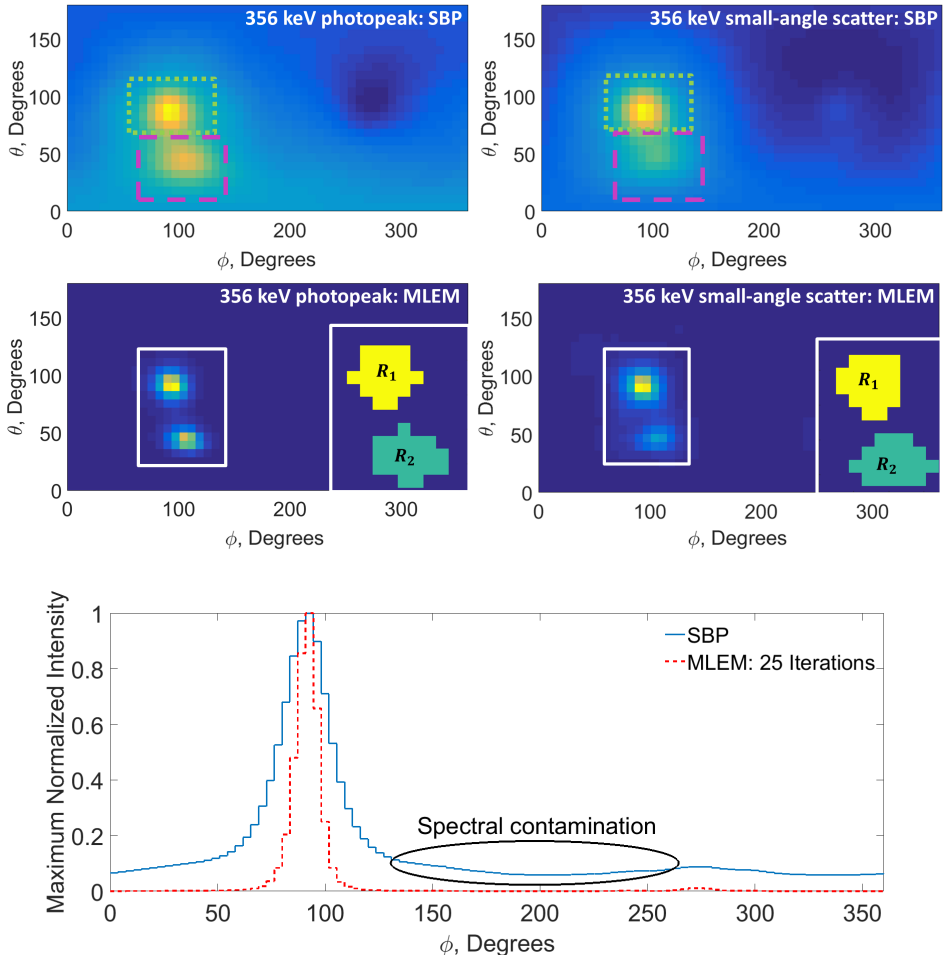

Figure 3.4: (Top) Simple-backprojection reconstructions of photopeak and small-angle scatter energy bins of interest for a combined lead-shielded and bare ^{133}Ba measurement. The human-defined lead and bare source regions are outlined with dashed and dotted lines respectively. Clear spectral contamination is seen in both directions as source PSFs overlap. (Middle) MLEM reconstructions of the same data. Note the improved angular separation between sources. Gross counts within source regions for each energy window are computed by summing the intensity of the 20 most intense pixels shown in the inset regions of interest. Images were scaled by individual maxima to maintain visual contrast. (Bottom) Azimuthal slices through SBP and MLEM reconstructions of the same bare source. Note the wider FWHM and non-zero baseline of the SBP reconstruction which contributes to spectral contamination.

Twenty five MLEM iterations were run on each energy bin of interest and directional intensities, assuming two source regions, C_1 and C_2 were extracted via summing

reconstructed pixel intensities

$$C_1 = \sum_{j \in \boldsymbol{R_1}} f_j^{25}, \quad C_2 = \sum_{j \in \boldsymbol{R_2}} f_j^{25} \tag{3.7}$$

where $\boldsymbol{R_1}$ and $\boldsymbol{R_2}$ were the 20 most intense pixels within human-defined source regions. Note this corresponds to a small, 1.6% of the entire 4π imaging space on a 25 by 50 bin angular image grid. 20 pixels were chosen within the source region of interest as they contained a majority of the reconstructed source intensity while maintaining angular separation between hot spots. Total recorded counts I_{tot} within an energy bin, including non-imagable events, were allocated to either source I_1^{ML} or I_2^{ML} based on the fractional imaged hot spot intensities

$$I_1^{ML} = I_{tot} \frac{C_1}{C_1 + C_2}, \quad I_2^{ML} = I_{tot} \frac{C_2}{C_1 + C_2}. \tag{3.8}$$

The ratio between C_1 and C_2 was found to be relatively insensitive to the number of image pixels summed in each region of interest: at most, a 4% perturbation was seen changing the number of summed pixels between 15 and 25. Net photopeak counts were calculated by subtracting off similarly allocated background at energies immediately higher than the photopeak. The photopeak, small-angle Compton scatter and background energy bins used in MLEM reconstructions for ^{133}Ba were listed in Fig. 3.3. A single, small-angle Compton scatter region was chosen from a prominent, high-energy peak to avoid the complication of subtracting off Compton continua from higher energy peaks. I_1^{ML} and I_2^{ML} for each photopeak and Compton scatter energy bin were then passed into the general shielding characterization process as discussed before.

3.2.1.2 Results

Bare and shielded ^{133}Ba measurements were reconstructed using MLEM on a discretized, 25 by 50, angular grid to estimate directional spectra and angular shielding. Combined photopeak ratio and Compton scatter residual plots for each measurement are shown in Fig. 3.5 to Fig. 3.8 with shielding estimates tabulated in Table 3.1. Combined, bare with lead, bare with tin and bare with iron measurements were reasonably reconstructed, sufficiently informing users of rough shielding atomic number and mass thickness in both the bare and shielded direction. Slight, systematic bias was seen in the iron-shielded case and may stem from naïve background subtraction. Contrastingly, the reconstructed atomic number in the aluminum direction of the combined, bare and aluminum measurement was drastically underestimated. However, the dotted bands of plausible residual fits contain many possible shielding combinations. This degenerate shielding behavior stems from gamma-ray attenuation changing slowly at high energies as a function of Z for low atomic number materials. Furthermore, naïve background subtraction assuming a flat continuum degrades the small expected change in photopeak ratios shown in Fig. 3.9. Combined, this results in an ambiguously reconstructed Z as many element's expected photopeak ratios are plausible within measurement uncertainty. This illustrates that for the technique to work, the magnitude of the spectral modulation must be large compared to combined statistical and systematic errors in computing directional spectra. Limiting cases occur for low Z shields, where photopeak ratios are not heavily modulated, or for thick shields where few photons are recorded. Including low energy peak ratios using the 81 keV ^{133}Ba emission would resolve this ambiguity as total attenuation changes more rapidly with atomic number at lower energies. This however requires combined, Compton and coded aperture imaging as 81 keV gamma rays do not produce many Compton imagable events in CdZnTe detectors. Despite this ambiguity, the Compton scatter residual accurately predicts the aluminum shielding thickness while the bare

source is accurately reconstructed.

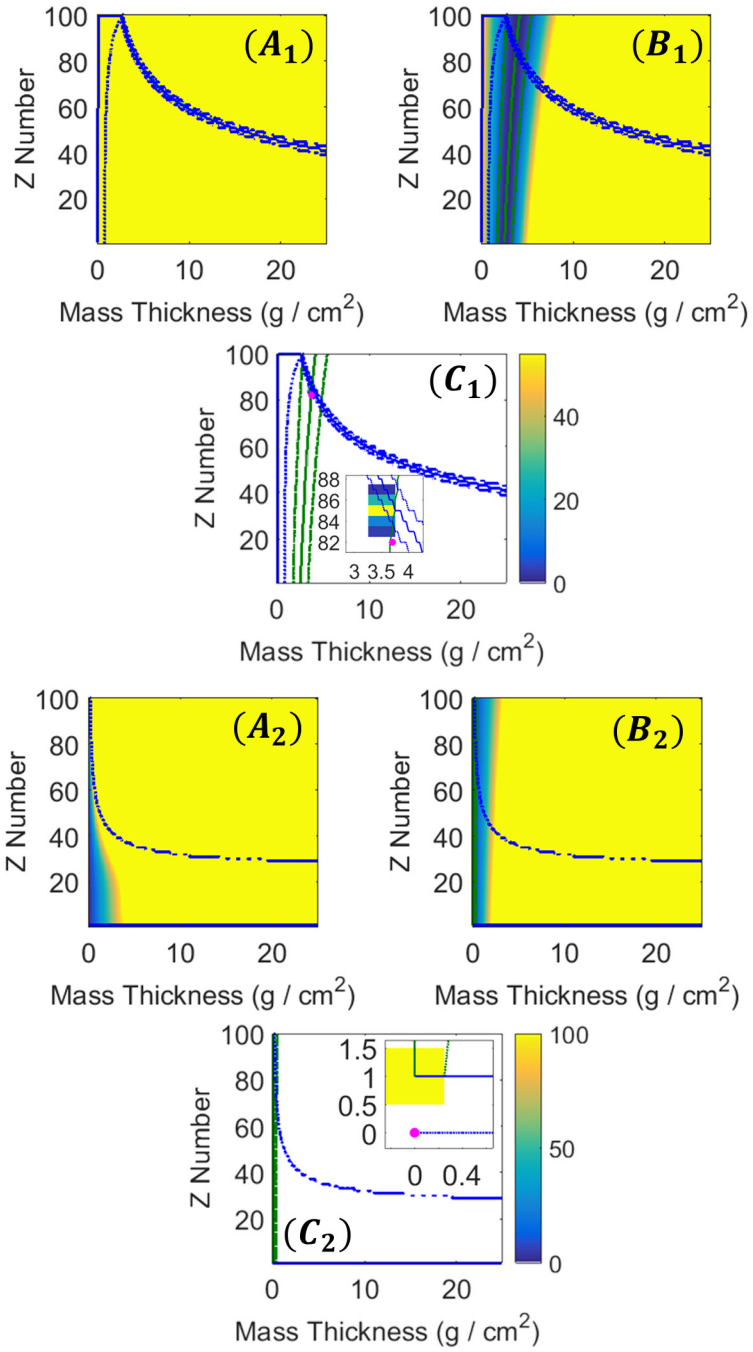

Figure 3.5: Peak ratio residual (A), small-angle Compton scattering residual (B) and combined residuals (C) for counts reconstructed in lead-shielded direction one (top) and bare direction two (bottom). Regions of good residual fit, corresponding to twice the minimum residual, are contained inside dashed lines. The inset figure shows uncertainties estimated via bootstrapping. True shielding characteristics are labeled with a magenta dot.

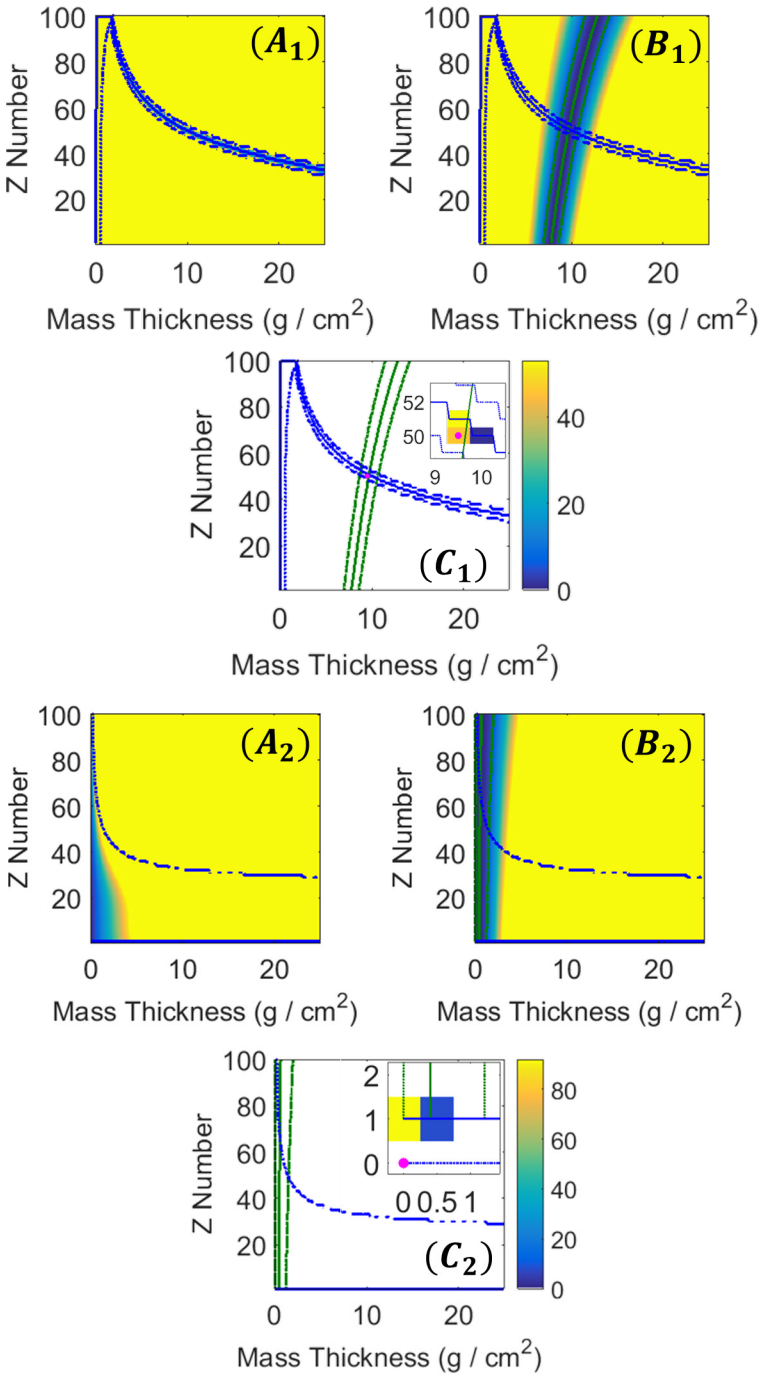

Figure 3.6: Peak ratio residual (A), small-angle Compton scattering residual (B) and combined residuals (C) for counts reconstructed in tin-shielded direction one (top) and bare direction two (bottom). Regions of good residual fit are contained inside dashed lines. The inset figure shows uncertainties estimated via bootstrapping. True shielding characteristics are labeled with a magenta dot.

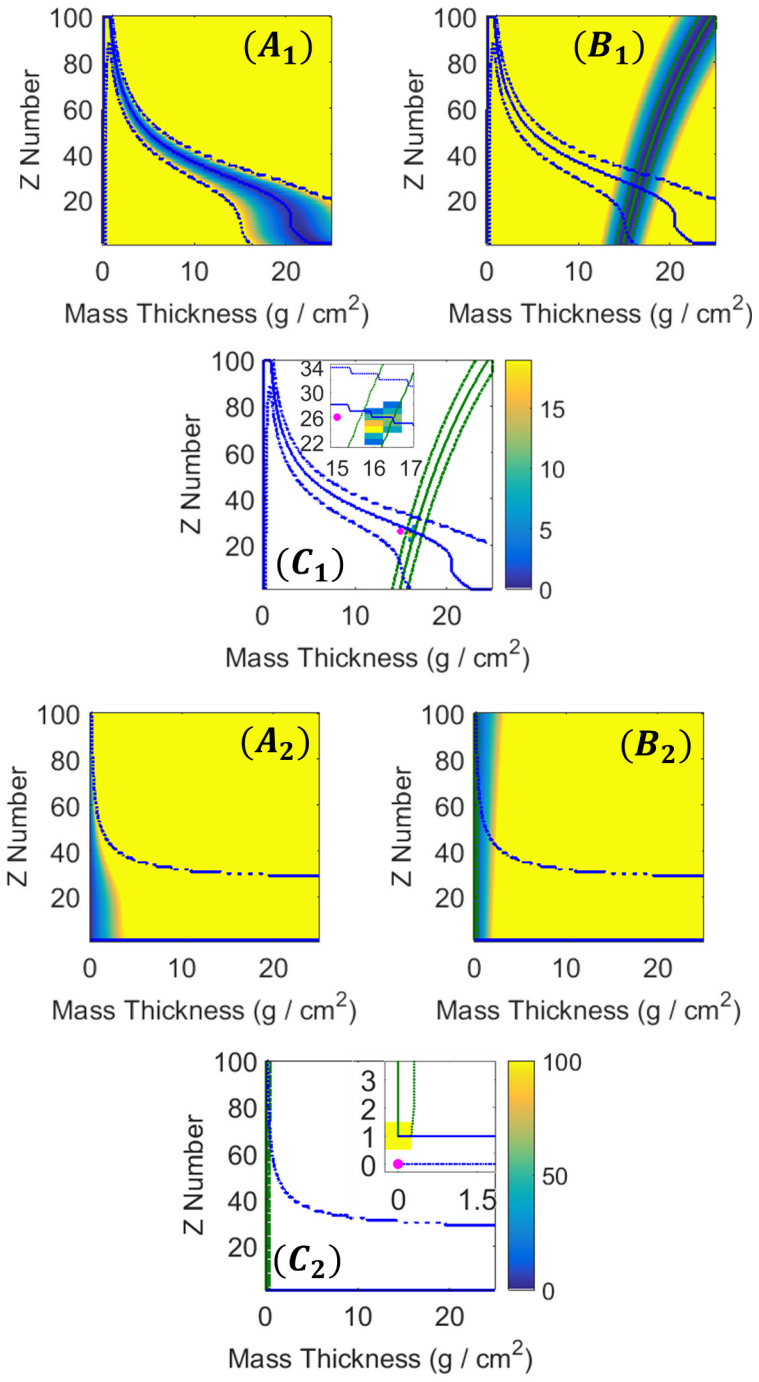

Figure 3.7: Peak ratio residual (A), small-angle Compton scattering residual (B) and combined residuals (C) for counts reconstructed in iron-shielded direction one (top) and bare direction two (bottom). Regions of good residual fit are contained inside dashed lines. The inset figure shows uncertainties estimated via bootstrapping. True shielding characteristics are labeled with a magenta dot.

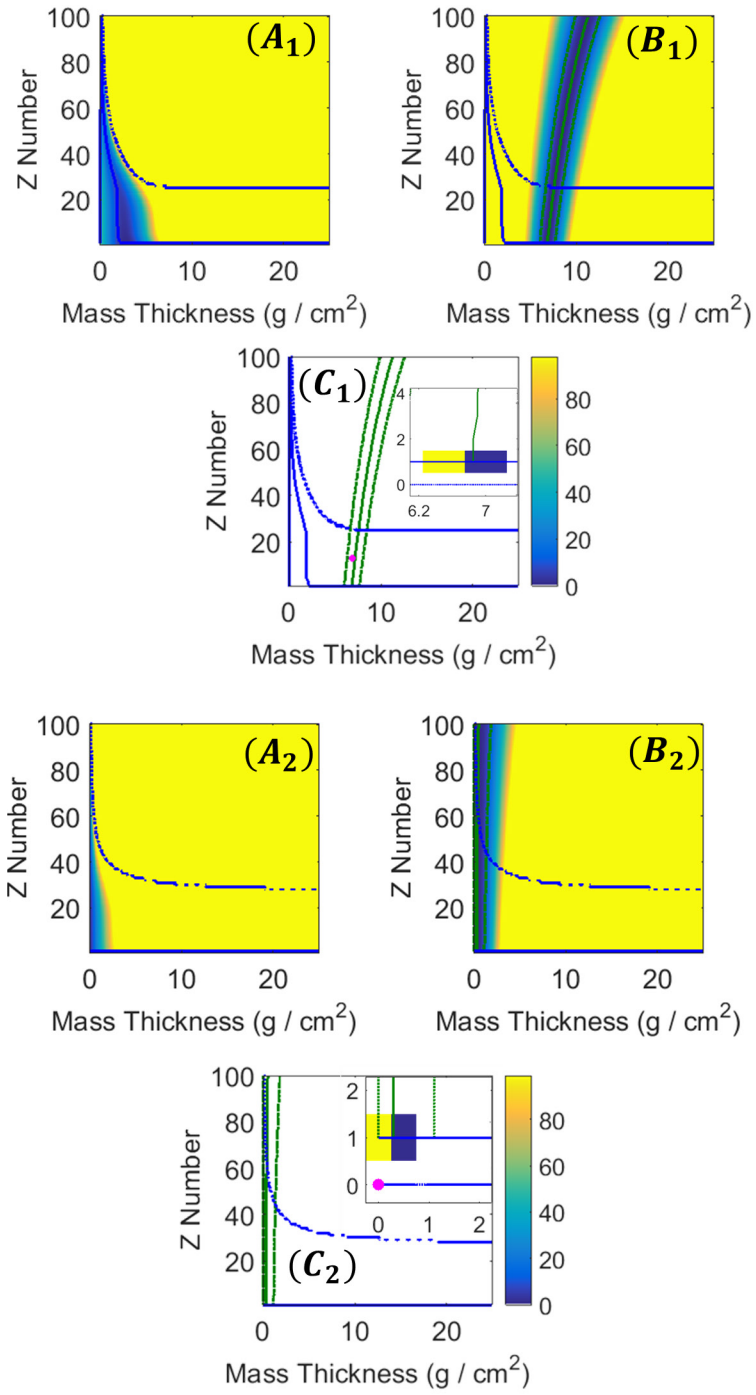

Figure 3.8: Peak ratio residual (A), small-angle Compton scattering residual (B) and combined residuals (C) for counts reconstructed in aluminum-shielded direction one (top) and bare direction two (bottom). Regions of good residual fit are contained inside dashed lines. The inset figure shows uncertainties estimated via bootstrapping. Note the general ambiguity is seen in aluminum Z number although Compton scattering correctly identifies shielding thickness. True shielding characteristics are labeled with a magenta dot.

Reconstructed uncertainties in shielding atomic number and mass thickness were quantified by processing many bootstrapped realizations of the initial measurements [75, 76]. Bootstraps were taken with the same number of samples, taken with replacement, as events in the initial measurements. Bootstrapped results for the lead, tin, iron and aluminum-shielded measurements are shown inset in Fig. 3.5 to Fig. 3.8. Bootstrapped uncertainties fell within regions of plausible residual fit marked by dashed lines. This suggests that the plausible bounds, corresponding to twice the minimum residual fit, provided via the shielding reconstruction algorithm can be used to conservatively estimate uncertainty without the extreme computational expense of bootstrapping.

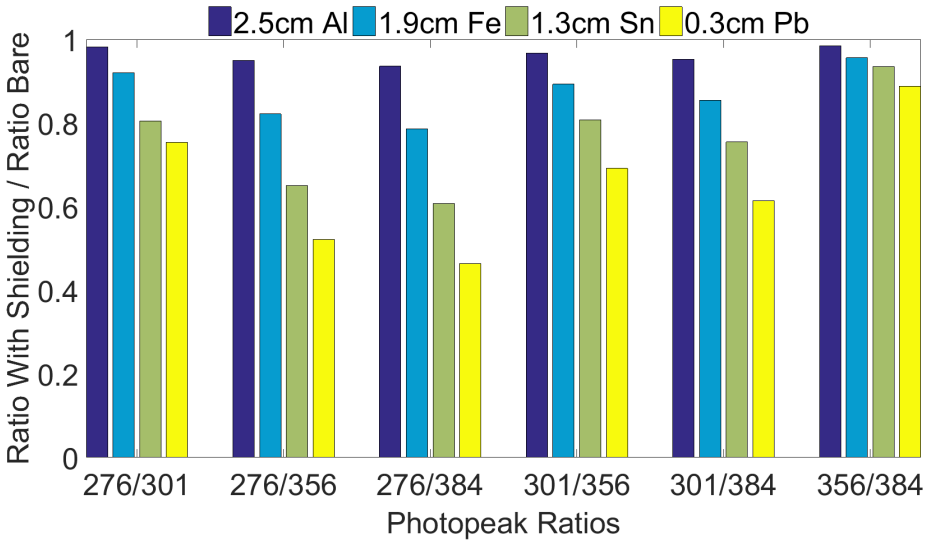

Figure 3.9: Expected deviations from bare ^{133}Ba peak ratios for measured shielding configurations. Note that the aluminum-shielded photopeak ratios do not greatly differ from the bare case. This complicates estimates of low-Z shields.

Table 3.1: True and estimated shielding mass thicknesses and atomic numbers for each direction. Tabulated 1σ uncertainties are statistical in nature and estimated via bootstrapping. Shielding parameters are listed in areal thickness and effect atomic number pairs $(\rho x, Z)$. Areal thicknesses are in units of g/cm^2.

Shielding	Pos. 1 True	Pos. 2 True	Pos. 1 Estimated	Pos. 2 Estimated
Al, Bare	$6.9, 13$	$0.0, 0.0$	$6.9\pm0.1, 1.0\pm0.0$	$0.0\pm0.1, 1.0\pm0.0$
Fe, Bare	$15.0, 26$	$0.0, 0.0$	$16.5\pm0.1, 25.0\pm1.3$	$0.0\pm0.0, 1.0\pm0.0$
Sn, Bare	$9.5, 50$	$0.0, 0.0$	$9.7\pm0.1, 50.5\pm0.5$	$0.3\pm0.1, 1.0\pm0.0$
Pb, Bare	$3.7, 82$	$0.0, 0.0$	$3.7\pm0.1, 85\pm0.7$	$0.0\pm0.0, 1.0\pm0.0$

3.2.2 Shielding Characterization of Multiple ^{235}U Sources Using Coded Aperture Imaging

As discussed in Chapter II, low-energy gamma rays rarely Compton scatter in CdZnTe detectors. Gamma rays that do scatter do not travel very far, generating poor-quality Compton cones. This precludes the use of Compton imaging to extract low-energy, directional gamma-ray spectra. Low-energy, directional spectra can be estimated with high-fidelity using coded aperture imaging. The extraction of directional spectra, and subsequent estimation of directional shielding, for simulated ^{235}U sources, presented in *Goodman et al.*, is outlined below [77].

3.2.2.1 Time-Encoded Imaging System

Typical low-energy, gamma-ray coded aperture imaging is conducted with modulation in the spatial domain using a high atomic number mask. However, modulation can be conducted in the time domain, known as Time Encoded Imaging (TEI), where a mask temporally modulates the incident radiation field. A recent TEI system using 3-D, position-sensitive CdZnTe detectors was built achieving roughly 1.5 mm FWHM image spatial resolution. The detector plane consists of a 3 x 3 array of 2 x 2 x 1.5 cm^3 CdZnTe crystals with pixelated anodes and a planar cathode. A rank 79, 1.4 mm pitch, adjustable thickness, tungsten mask is rastered temporally in front of the

array. List-mode data is output from the spatially-sensitive detector array which is subsequently stitched together into a large, high-resolution mask. The larger mask is then cross-correlated with a decoding matrix to reconstruct a source image. Detailed discussion of system parameters and the reconstruction process is provided in [17,65].

Image reconstruction is repeated on a per-energy-bin basis, from which directional spectra can be estimated. Several research and commercial systems have experimentally demonstrated directional spectra estimation using traditional, spatial coded aperture [66,78]. However, time-encoded reconstructions using pixelated CdZnTe are substantially more uniform, with fewer systematic artifacts, than equivalent reconstructions generated with spatial coding [65]: background non-uniformity and image artifacts fundamentally limit the quality of estimated directional spectra. Background fluctuations, at best, are bounded by Poisson fluctuation. At worst, systematic fluctuations in image background add additional variance to directional spectra. Other image artifacts from detector imperfections, such as gaps producing a 'hashtag'-shaped artifact in previous spatial, CdZnTe coded aperture systems, further systematically perturb reconstructed images [65]. These artifacts can cause substantial, spectral crosstalk between independent sources in a reconstruction. This spectral crosstalk, when superimposed on the image, prevents complete, angular deconvolution. Therefore, time-encoded imaging enables robust extraction of directional spectra, compared to traditional coded aperture, to characterize shielding.

3.2.2.2 Simulation Geometry

Five equal intensity ^{235}U point sources were simulated in Geant4 as shown in Fig. 3.10. Either 0.5 cm of iron, 1.0 cm aluminum, 0.1 cm tungsten or 0.1 cm of lead was placed in front of sources while one was left bare. On average, $4 \cdot 10^4$ gamma-rays were emitted isotropically from each source at each mask step using tabulated ^{235}U emission probabilities. For simplicity, no uranium self attenuation was modeled.

Single-pixel detector energy resolution was chosen as 0.5% FWHM at 662 keV to approximate the performance of new digital CdZnTe arrays [79]. No detector subpixel spatial resolution was used [80].

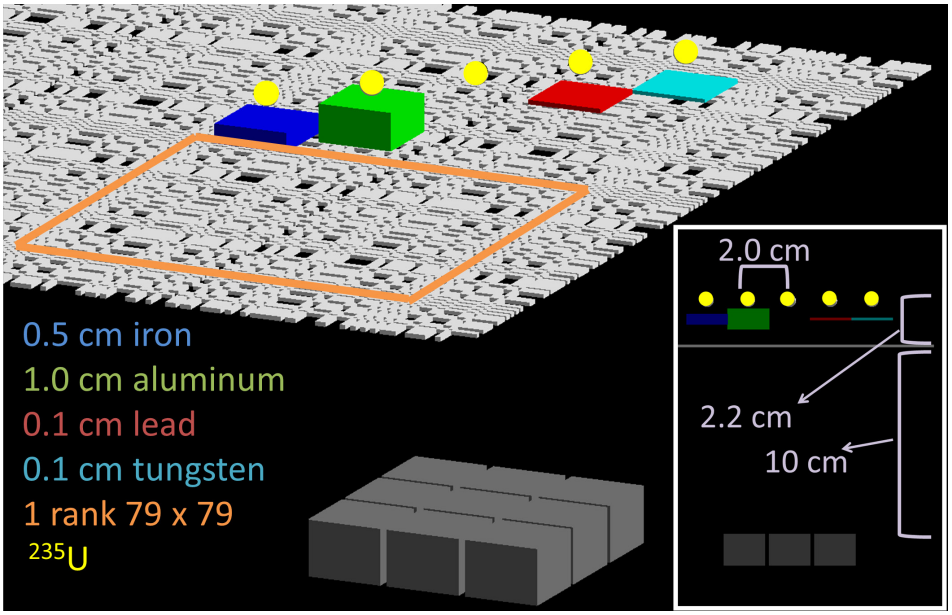

Figure 3.10: Five sources behind various shields simulated using Geant4. A rank 79 MURA, 1 mm thick tungsten mask was then rastered back in forth in front of the 3 x 3 CdZnTe array for TEI reconstructions.

Count rates as a function of energy for each detector pixel were cross-correlated with the attenuation history of each image element and summed linearly on a common image grid $I(x, y, E)$ after shifting based on detector pixel location. An estimate of image background in a given energy bin E, estimated from a human-defined, non-source direction, was then subtracted off the entire image as a pedestal correction. Detailed discussion of the time-encoded image reconstruction process is provided in [17] while a similar pedestal subtraction process is discussed in [66].

3.2.2.3 Results

TEI reconstruction was conducted using cross-correlation. Five hot spot directions were determined by looking at the 186 keV photopeak image. Both angularly-

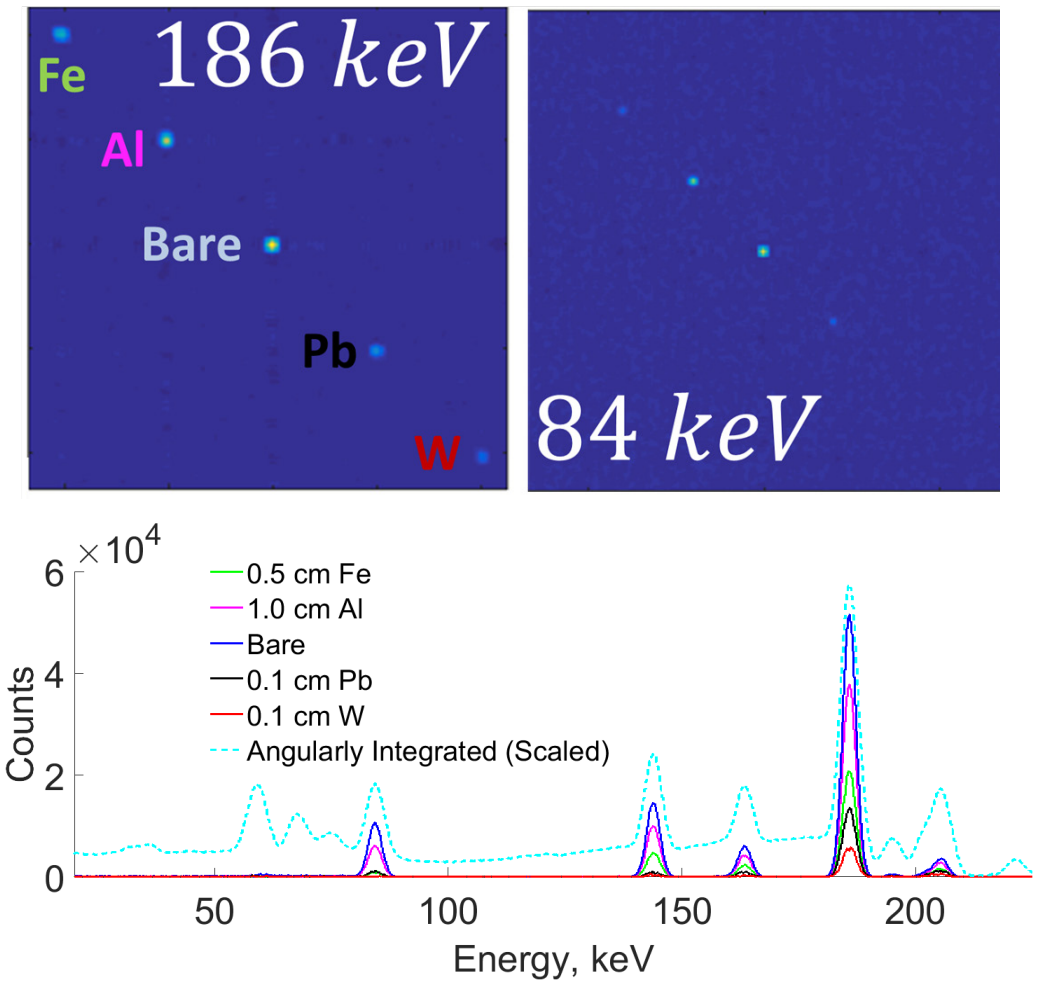

Figure 3.11: (Top) Reconstructed images at 186 and 84 keV emphasizing the energy-dependent modulation of various shields. (Bottom) Spectra $I(x, y, E)$ queried along each colored direction and the angularly-integrated spectra.

integrated and directional spectra with reconstructed images at several ^{235}U emissions are shown in Fig. 3.11. For two source directions clear, small-angle Compton scatter was seen with increased counts around the hot spot at lower energies. Shielding in these directions was estimated with both Compton scatter and photopeak attenuation information as shown in Fig. 3.12: these directions correspond to iron and aluminum shielded sources respectively. The iron and aluminum shields were accurately estimated in both cases. Similar analyses were conducted on the other three directions which correspond to bare, lead and tungsten shields. The bare and lead-shielded sources were reconstructed properly while large bias was seen in the tungsten direc-

tion. This bias is still under investigation but is suspected from a larger-than-expected number of counts in the 84 keV window of the tungsten direction from scatter and energy resolution effects. 1 mm of tungsten attenuates greater than 99.999% of 84 keV source gamma rays meaning no real 84 keV signal was expected. Some 84 keV counts were incorrectly reconstructed in the tungsten direction such that only elements above $Z = 81$, which corresponds to a K-edge of roughly 84 keV, have plausible shielding configurations. This systematically biased the reconstruction towards higher atomic number.

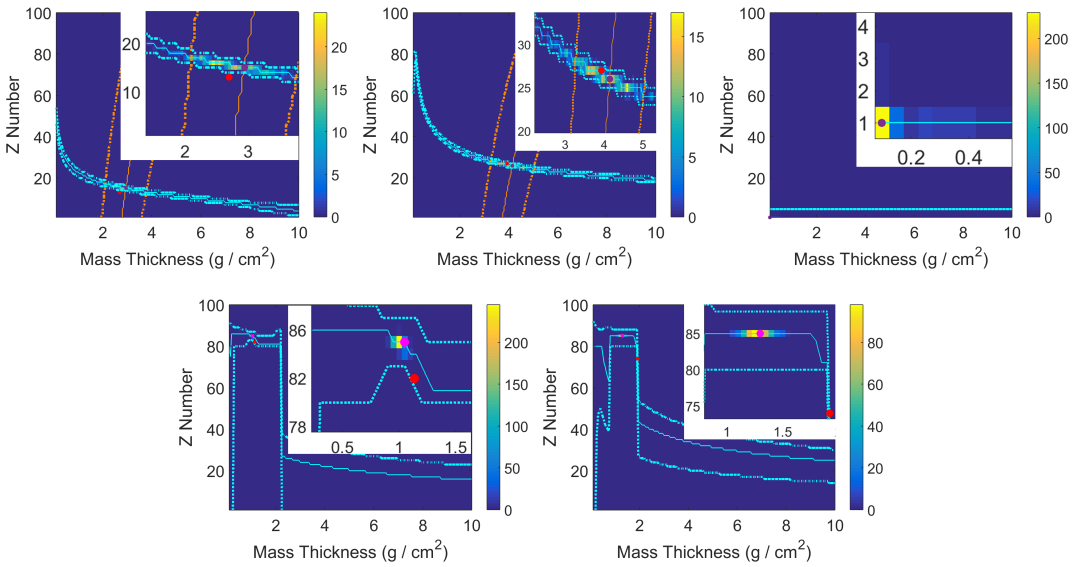

Figure 3.12: From left-to-right and top-to-bottom: Reconstructed shielding in the aluminum, iron, bare, lead and tungsten shielded directions. Dashed blue and orange lines illustrate regions of reasonable photopeak and Compton scatter residual fits respectively. Discontinuous tungsten and lead photopeak fit shapes stem from K-edges in the photoelectric cross section. Best estimates of shielding were shown with a magenta dot while true shielding was shown in red. Inset regions show bootstrapped shielding estimates to quantify uncertainty.

Bootstrapped estimates of source intensities were conducted as shown in Fig. 3.13. Raw intensities of shielded sources were underestimated as expected. Shielding corrections improved estimates such that they better approximated the intensity of the bare source as shown in Table 6.1. Notably, uncertainties in estimated source intensities were dominated by spread in estimated shielding, not raw intensities $I_p(X, Y, E)$.

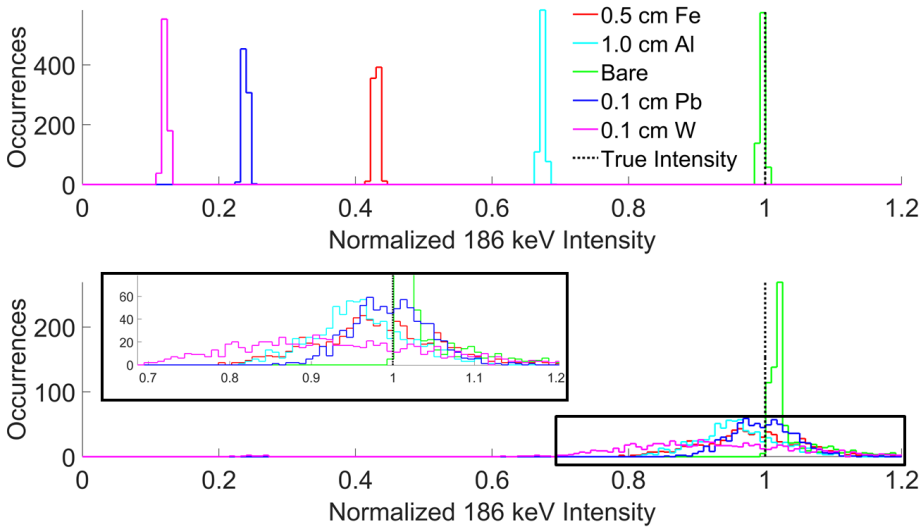

Figure 3.13: Raw (top) and shielding corrected (bottom) histograms of estimated source intensities. In reality all sources have equal emitted intensity. Slight offset in the corrected, bare case stems from not having zero shield as a possible choice.

Simulated directional spectra computed using coded aperture imaging can be used to estimate directional shielding in a manner similar to Compton imaging. However shielding estimates are complicated when including photopeak ratios computed with low-energy gamma rays that fall below K-edge energies. Cross sections at these low energies vary strongly as a function of element. Slight, systematic errors in computed photopeak ratios can strongly bias combined, uncertainty-weighted shielding estimates. This complication was not seen in Compton imaging reconstructions as incident, imagable gamma rays fall above elemental K-edges. As such, directional photopeak ratios computed using low-energy gamma rays must be carefully computed to avoid even small levels of systematic bias.

3.3 Conclusion

The simple shielding characterization technique developed by *Streicher et. al* can be applied on a direction-by-direction basis using gamma-ray imaging. Using imag-

Table 3.2: True and estimated shielding mass thicknesses and atomic numbers with raw and corrected intensity estimates. Tabulated 1σ uncertainties are statistical in nature estimated via bootstrapping. Note uncertainties in raw intensities are small compared to that of corrected estimates. This shows that uncertainty in estimated shielding dominates the problem.

Shielding	True $Z, g/cm^2$	Estimated $Z, g/cm^2$	$\frac{I_{raw}}{I_{true}}$	$\frac{I_{corrected}}{I_{true}}$
Bare	$0, 0.0$	3.7±4.9, 0.2±0.2		1.04±0.04
Al	$13, 2.7$	15.5±1.2, 2.8±0.5	0.678±0.004	0.96±0.06
Fe	$26, 3.9$	26.4±1.6, 4.0±0.7	0.434±0.004	0.99±0.08
W	$74, 1.9$	84.9±0.6, 1.3±0.2	0.126±0.003	0.94±0.15
Pb	$82, 1.1$	84.9±0.4, 1.05±0.04	0.243±0.004	1.00±0.05

ing, the inherent, undesirable angular integration of traditional spectrometers can be avoided. This greatly extends the applicability of shielding characterization algorithms to more realistic measurement scenarios containing multiple sources. Furthermore, the technique is agnostic to detector type, assuming sufficient energy resolution to resolve photopeaks, or imaging modality given source separation is large compared to the imaging, angular resolution. Directional shielding estimation was experimentally demonstrated using Compton imaging, reconstructed using MLEM to reduce spectral crosstalk, for ^{133}Ba sources. Estimation of uranium directional shielding was demonstrated using Geant4 simulation of a recently reconstructed time-encoded imaging system. Shielding estimates were used to correct estimates of source activities to within statistical uncertainties extracted via bootstrapping. Combined, these results illustrate the practical, shielding characterization capabilities of imaging, CdZnTe detectors for black-boxes.

CHAPTER IV

Atmospheric Effects and Ultra-Far-Field Imaging

Measurements of strong, gamma-ray sources, such as those encountered after the detonation of an RDD or IND, are often conducted in the far-field. Air, which can be thought of as a tenuous, omnipresent form of shielding, affects gamma-ray spectra in far-field measurements. The effects of intervening air, as discussed in *Goodman et al.*, can be leveraged to extract source information [81].

4.1 Atmospheric Perturbation of Emitted Gamma-Ray Spectra

Air is a low-density, $\rho = 1.2 \cdot 10^{-3}\ g/cm^3$, low-Z, $Z_{eff} = 7.64$, gas composed of primarily nitrogen [82]. Greater than 90% of photon interactions with air are Compton scatter for incident energies above 60 keV. Furthermore, the mean free path (MFP) of photons is on the order of 100 m. The large MFP and dominance of Compton scatter interactions allows gamma rays to travel long distances before detection.

As photons propagate through the air the uncollided, photopeak flux falls off with standoff r following exponential attenuation and solid angle

$$I(r) = \frac{I_0 e^{-\rho \frac{\mu(E)}{\rho} r}}{4\pi r^2} \tag{4.1}$$

where I_0 is the emitted photopeak intensity at energy E, $\mu(E)$ is the linear attenuation coefficient of air and ρ is air density. Given multiple emitted photon energies, the ratios of uncollided, photopeak fluxes at some distance away from the detector follows

$$R(r) = \frac{I_{0,1} e^{(\frac{-\mu(E_1)}{\rho} + \frac{\mu(E_2)}{\rho})\rho r}}{I_{0,2}} \tag{4.2}$$

where $I_{0,1}$ and $I_{0,2}$ are the initial photopeak intensities at energy E_1 and E_2 respectively. Given knowledge of initial source parameters, $I_{0,1}$ and $I_{0,2}$, and the density of air, ρ, the distance to a source can be estimated via measured photopeak ratios. However, photopeak ratios cannot be used to estimate standoff for sources that emit a single-energy gamma ray. The ratio between scattered to unscattered gamma-ray flux at a point, called the scatter ratio, is sensitive to the mass thickness of the scattering volume traversed. For thin, solid shields the small-angle-scatter ratio is roughly proportional to a shield's areal thickness as discussed in Chapter III [14].

Previous studies on the effects of gamma-ray air-scatter have used empirical buildup terms to estimate the intensity of scattered gamma rays [83]. However, these studies neglected the effects of the dense ground on scattered gamma-ray fluxes. Previous effort focusing on the effects of ground-scattered radiation only measured the behavior out to limited standoffs of tens of meters [84]. Environmental scatter has also been implemented into GADRAS to better account for floor and wall-scattered gamma rays [85]. Simplified analytical transport models have been implemented for complex, 3-D geometries, such as the slab geometry in this specific problem, to quickly estimate recorded gamma-ray spectra [86]. However to understand the complex, far-field behavior of both ground and air-scattered gamma rays a full MCNP6 model was developed [87]. It models how the scatter ratio changes as a function of ^{137}Cs standoff in realistic geometries at novel, large-standoffs exceeding half a kilometer.

The simplistic simulation consisted of a point source floating 3.5 m above typical western dirt with F5 tallies placed 1 m off the ground radially away from the source

to estimate point spectra. Air and ground compositions were taken directly out of the PNNL material compendium [88]. The scatter ratio was found to have two different contributions; scatter from the ground and scatter from the air, as shown in Fig. 4.1. These different components were separated in simulation, showing ground scatter contributes to the scatter ratio at small distances, while air scattering dominates at larger standoffs. The strength of ground contributions was found to vary with source height, particularly for small standoffs of less than roughly 30 m. However standoff estimation is robust even without *a priori* knowledge of source height above the ground as air scatter contributes to more than 80% of total down-scattered flux at standoffs greater than 100 m: 2 m uncertainty in source height at a 100 m standoff only propagates to roughly 25 m standoff uncertainty. This fractional uncertainty becomes smaller at larger standoffs, and is comparable to contributions from statistical uncertainty for realistic dwell times. Regardless, a roughly linear trend in the scatter ratio with source standoff is seen, similar to that measured for thin solid shields, in this realistic geometry. This scatter ratio trend can be used to estimate standoff for gamma-ray sources that emit only a single energy photon. However, this scatter-based approach is generally more complicated and offers worse, systematic uncertainties than photopeak-based techniques.

4.2 Far-Field Measurement of Bare Sources

Measurements were conducted at Idaho National Laboratory on August 31, 2017. Strong 0.8 Ci ^{137}Cs and 88 Ci ^{192}Ir sources were placed bare, 3.5 m off the ground on an aluminum ladder while a pickup truck was used as a mobile measurement platform. The CdZnTe detector system was placed inside the cab of the pickup while the HPGe detector was placed outside on the truck roof. The truck window in front of the CdZnTe system was opened to offer an unimpeded line-of-sight to the source. Both detectors and readout computers were powered via an external generator. The ^{137}Cs

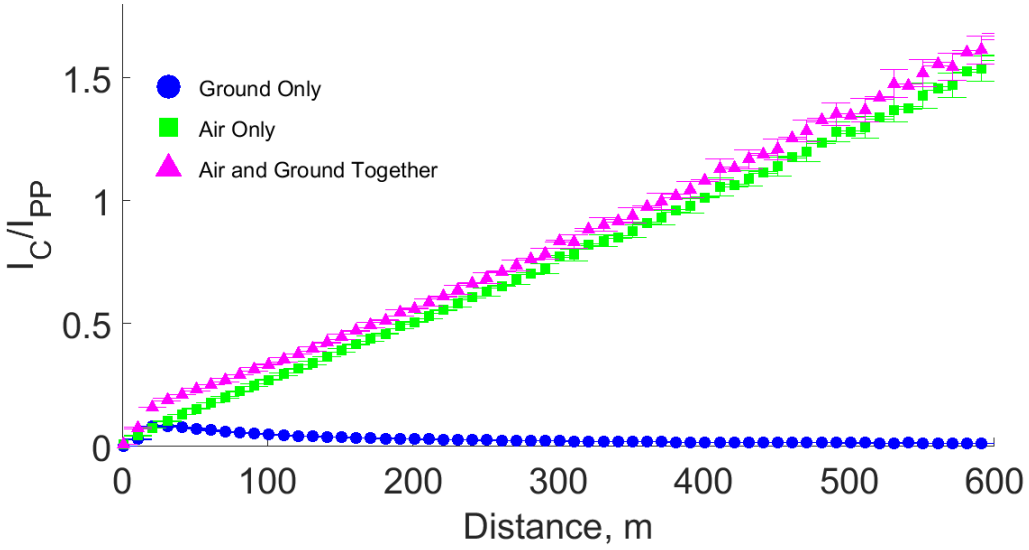

Figure 4.1: The scatter ratio as a function of ^{137}Cs source standoff. The optically thick ground causes an initial transient for small distances. At large standoffs the ratio is dominated by air effects. Plotted 1σ error bars are statistical in nature. The small-angle-scatter energy bin was [463,661] keV. No detector resolution was implemented such that only 661.7 keV events were used in the photopeak.

source was measured at standoffs of 50, 100, 150, and 200 m while the ^{192}Ir source was measured at standoffs of 200, 400, and 600 m. A small, 10 μCi ^{137}Cs check source was also measured in the near-field. Air density was recorded using measurements from the Idaho Falls regional airport weather station (Fanning Field, ID USAF 725785), a distance of approximately 64 km from the experiment location.

When comparing HPGe spectra taken at each standoff, the attenuation effects of atmospheric air are obvious as shown in Fig. 4.3. For ^{192}Ir the energy-dependent attenuation of differing photopeaks was seen when pivoting around the normalized 468 keV peak: the roughly 300 keV photopeak triplet was attenuated relatively more than the roughly 600 keV photopeak triplet. Furthermore, clear evidence of Compton-downscatter is seen in the buildup of low-energy counts in both the ^{137}Cs and ^{192}Ir measurements with increasing standoffs. These spectral features were used to estimate standoff.

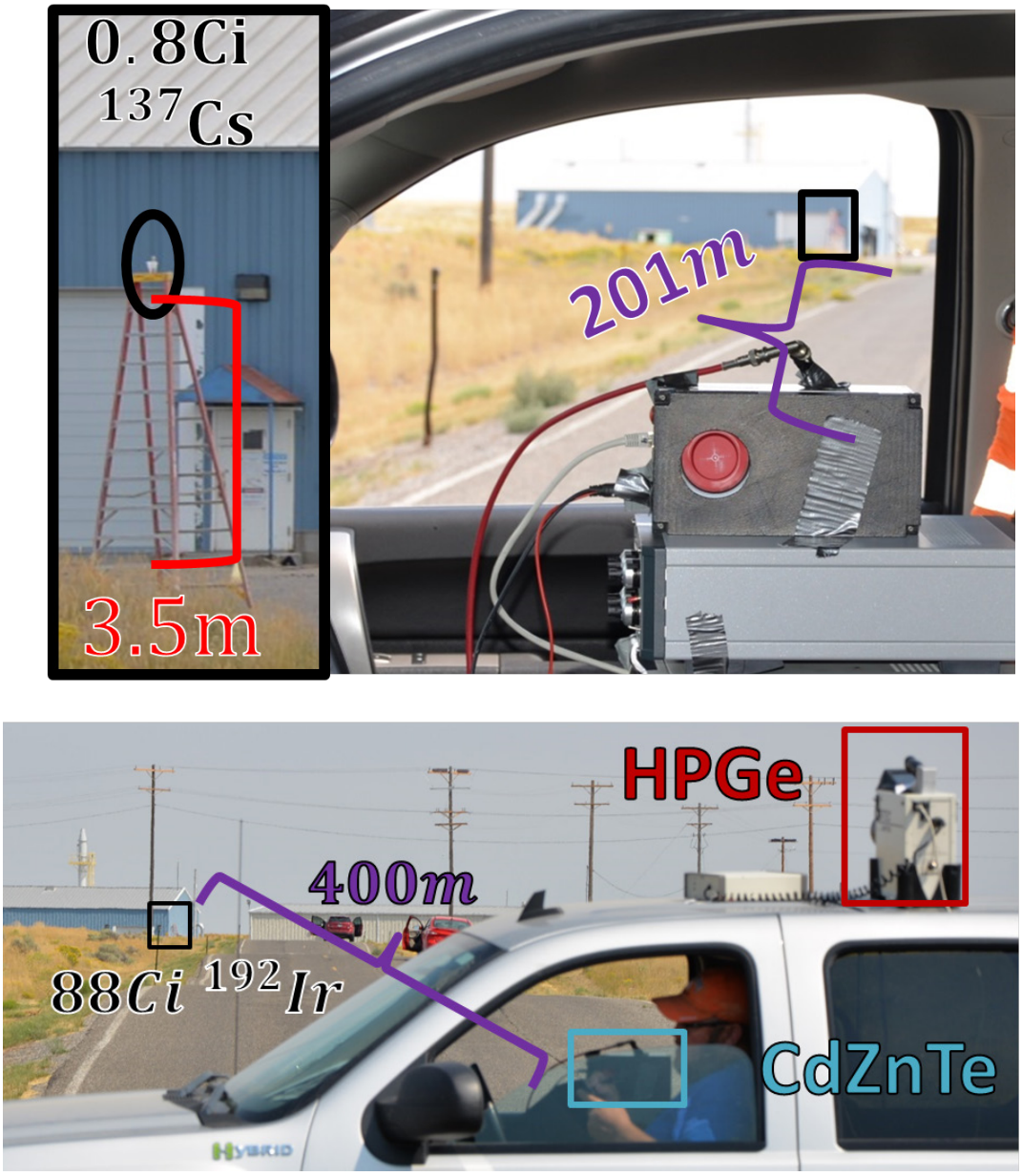

Figure 4.2: (Top) Measurements were conducted at Idaho National Laboratory with a pickup. The CdZnTe system was placed inside the truck cab. Sources were on top of a 3.5 m ladder well away from buildings to mitigate scatter. The truck cab window facing the source was opened giving the CdZnTe system an unimpeded view of the source. Source location is highlighted with a black box with the inset figure showing additional detail. (Bottom) Far-field measurement at 400 m showing relative HPGe placement on the truck roof.

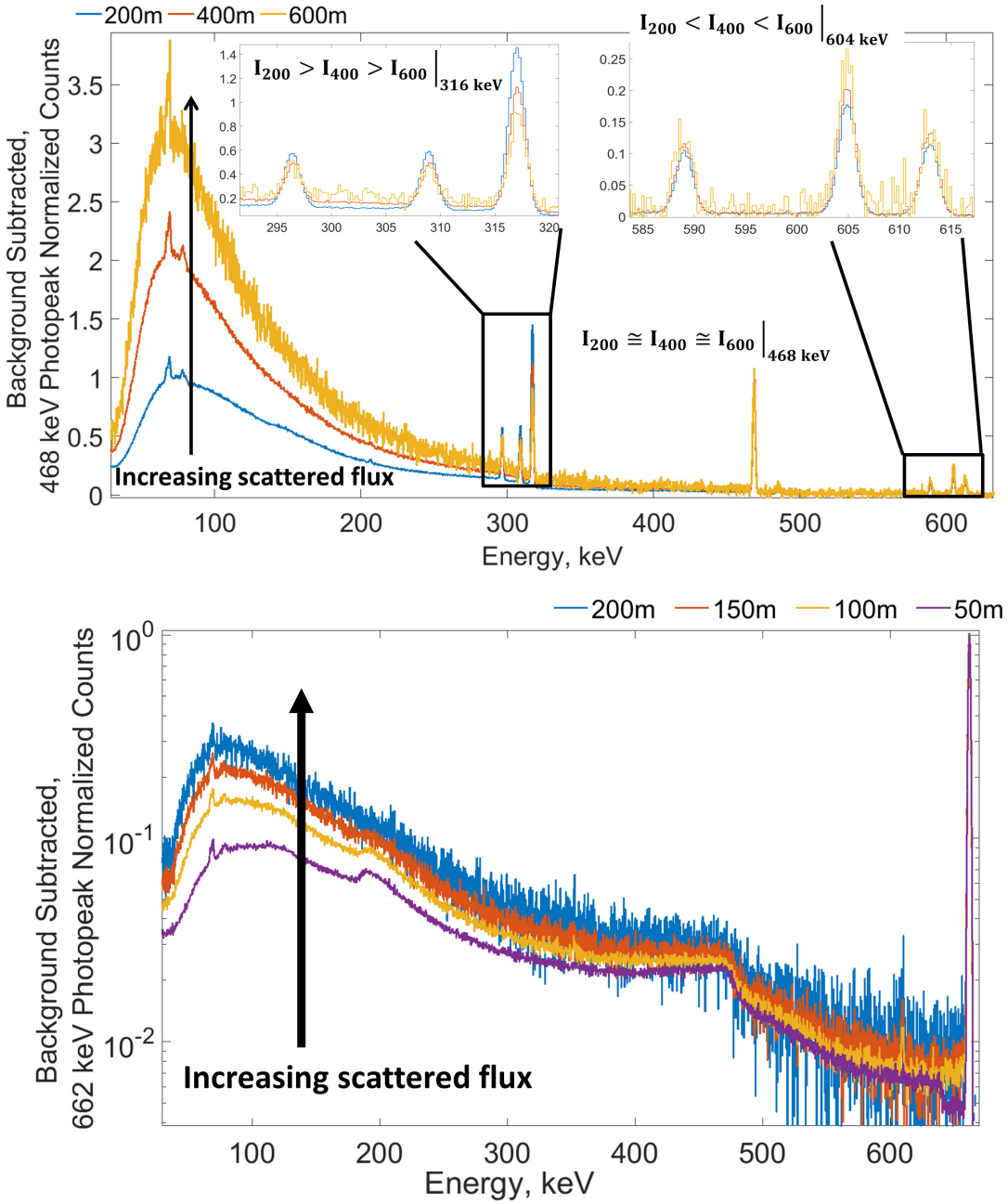

Figure 4.3: HPGe spectra of ^{192}Ir (top) and ^{137}Cs (bottom) sources as a function of standoff. Spectra were background subtracted and normalized by respective photopeaks. Low-energy ^{192}Ir photopeaks are relatively less intense at larger source standoffs due to larger attenuation. Contrastingly, high energy ^{192}Ir photopeaks are relatively more intense than the 468 keV peak at large standoffs due to smaller attenuation. Note the increase in counts below the photopeaks as a function of standoff for both sources due to down-scattered gamma rays.

4.2.1 3-D Source Reconstruction

Previous, model-based characterization techniques estimate shielding atomic number and areal thickness, ρx, by comparing measured photopeak and scatter ratios against expectations over a tabulated list of elements and thicknesses [14]. Source standoff estimation through air, a form of shielding characterization, is greatly simplified as the Z number of air is known *a priori*. Furthermore, measuring air density ρ is trivial using a simple weather station, allowing for direct estimation of standoff x. Source-to-detector standoff can be simply estimated via a calibration curve generated using measured photopeak and scatter ratios as a function of standoff. Calibration-curve-based techniques are easily implemented, not requiring detailed knowledge of detector efficiencies, and can illustrate the feasibility of spectral-based standoff estimation. For the ^{192}Ir and ^{137}Cs measurements presented here, photopeak and scatter ratios were recorded as a function of standoff. Environmental background, from naturally occurring radioactive materials, was first mitigated by subtracting off a background measurement. Contributions from the incomplete-energy-deposition of higher-energy gamma rays in both photopeak and downscatter regions were subtracted off using baseline estimates from the high-energy side of photopeaks. To estimate source-to-detector standoff at an unknown distance using photopeak ratios, an exponential fit from all points, excluding data from the queried point of interest, was generated. The calibration curve was then inverted to convert the photopeak ratio at the queried point to estimated standoff. A similar process was used to estimate standoffs using scatter ratios with a linear calibration curve. Energy windows used for computing scatter and photopeak ratios are shown in Fig. 4.4.

Source standoff was computed for ^{192}Ir measurements using HPGe photopeak ratios. Recorded photopeak ratios between the 316, 468, and 604 keV lines were compared against expected values computed using Eq. 4.2 and NIST cross sections [89]. Measured data points agreed with the predicted trend, shown in Fig. 4.5, with

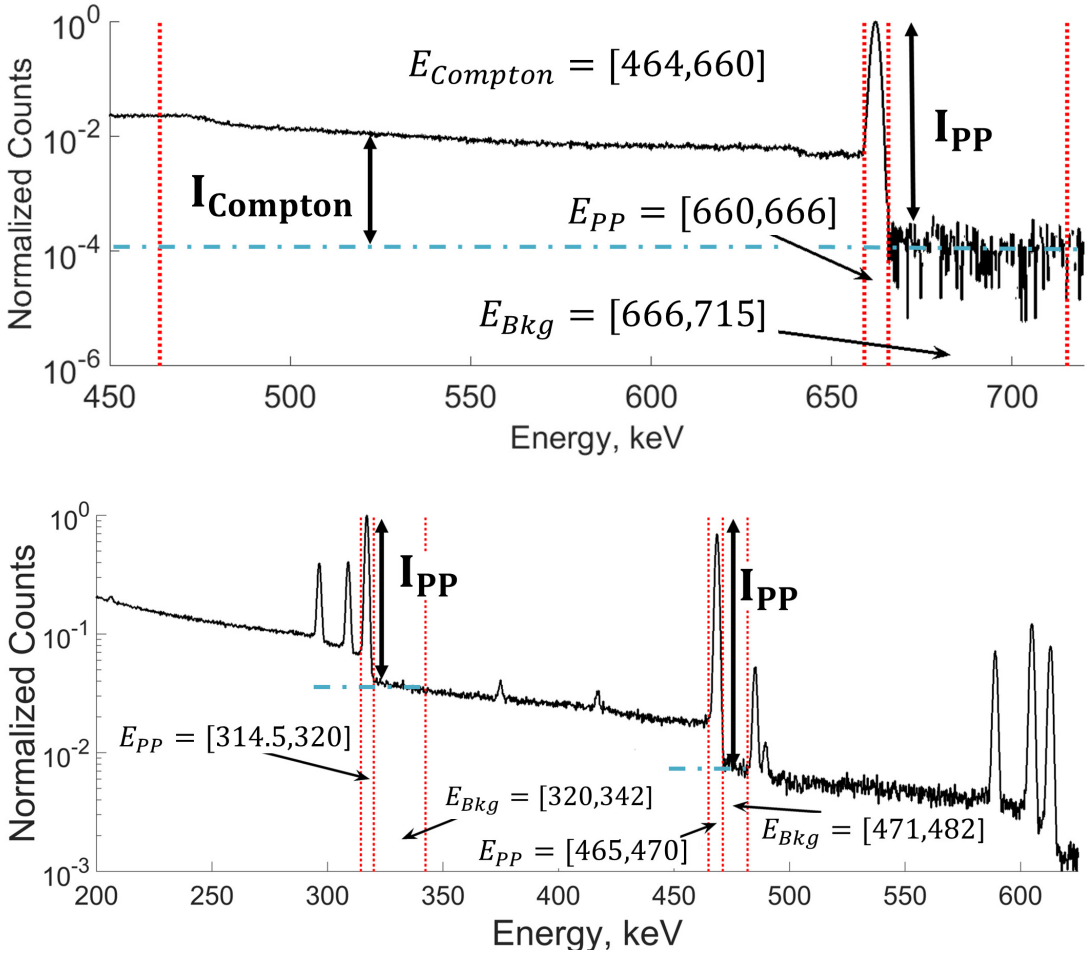

Figure 4.4: Photopeak, background and Compton scatter energy windows used in background-subtracted ^{137}Cs (top) and ^{192}Ir (bottom) spectra to estimate standoff. Contributions from incomplete-energy-deposition events, shown with cyan dash-dot lines, were subtracted off from both the photopeak and scatter window. The low-energy, Compton downscatter cut was placed near the ^{137}Cs Compton edge to help mitigate the influence of incomplete-energy-deposition events. Both spectra are from the Ortec trans-SPEC HPGe detector.

at most 2σ of statistical, measurement uncertainty. An exponential fit of 316 to 468 keV photopeak ratios was used to estimate source standoff for the 600 m measurement and is shown in Fig. 4.6. Uncertainty estimates, computed from bootstrapping the HPGe spectra, contained the true distance within statistical uncertainty [75, 76].

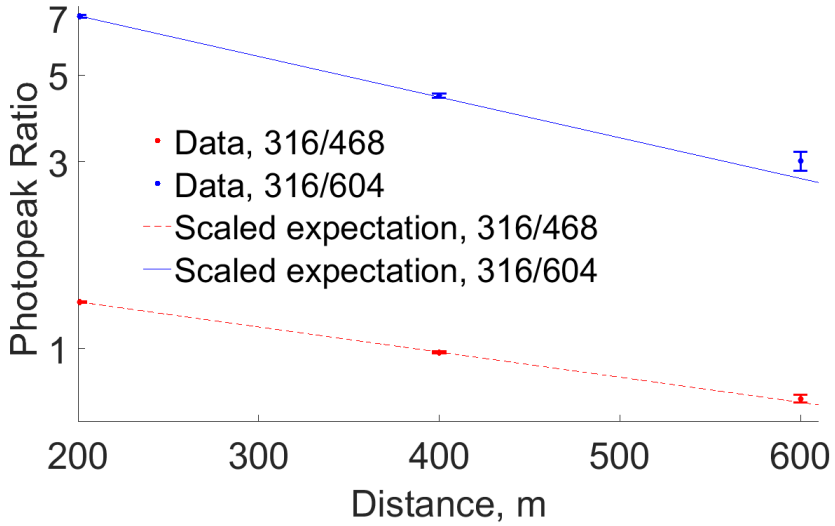

Figure 4.5: Photopeak ratios as a function of source standoff. Reasonable agreement is seen with expected photopeak ratios, computed using tabulated cross sections from NIST, with all data points agreeing within 2σ statistical measurement uncertainty. NIST expectations were scaled to 200 m values to account for detector efficiency.

For ^{137}Cs the measured scatter ratio from HPGe spectra increased linearly with distance, shown in Fig. 4.7, in agreement with expected trends modeled in MCNP6. A similar analysis was conducted for HPGe ^{137}Cs spectra to estimate standoffs at 50, 100 and 150 m using a linear fit to scatter ratios and is shown in Fig. 4.7. All bootstrapped standoff distributions in Fig. 4.8 contained the true standoff within statistical fluctuations, showing that source standoff can be estimated with even a single photopeak.

3-D source localization is conducted by combining estimates of source standoff from the atmospheric perturbation of gamma-ray spectra with directionality estimated via traditional Compton imaging. The combination of standoff and directional

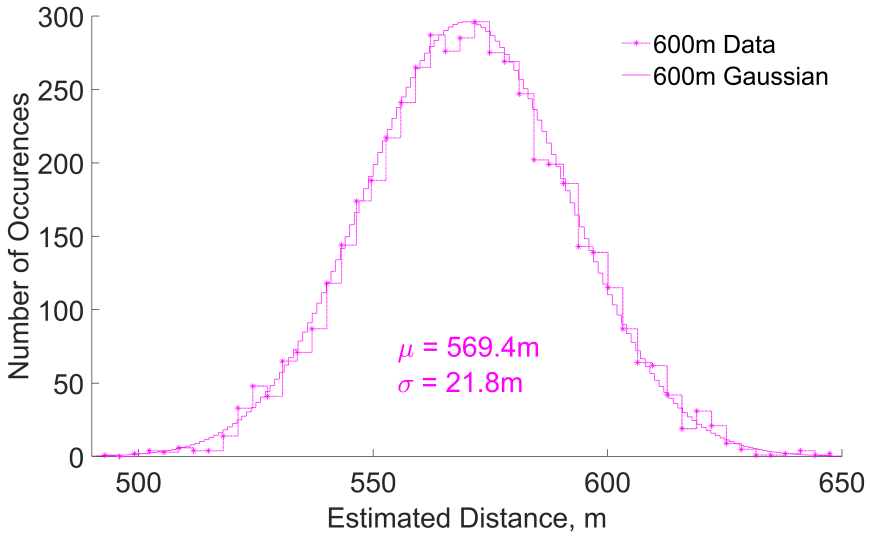

Figure 4.6: 5000 bootstrapped estimates of ^{192}Ir source standoff at 600 m using an extrapolated fit of photopeak ratios generated with data at r=200 and 400 m. Bootstraps contain the same number of counts as the initial measurements. The distribution appears approximately Gaussian with standard deviation, σ and mean, μ, inset into the figure.

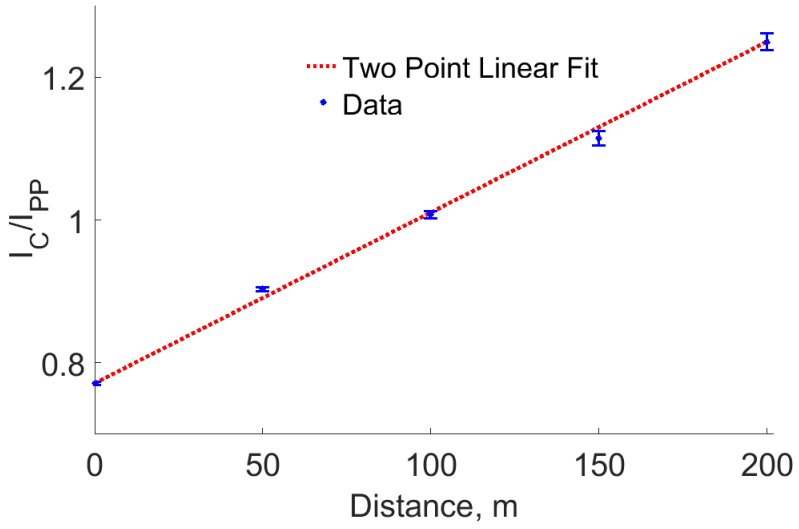

Figure 4.7: Measured ^{137}Cs scatter ratio as a function of source standoff. A linear fit between $r = [0, 200]$ m was made to estimate intermediate distances via interpolation. Plotted 1σ error bars get larger with increasing standoff due to limited counting statistics.

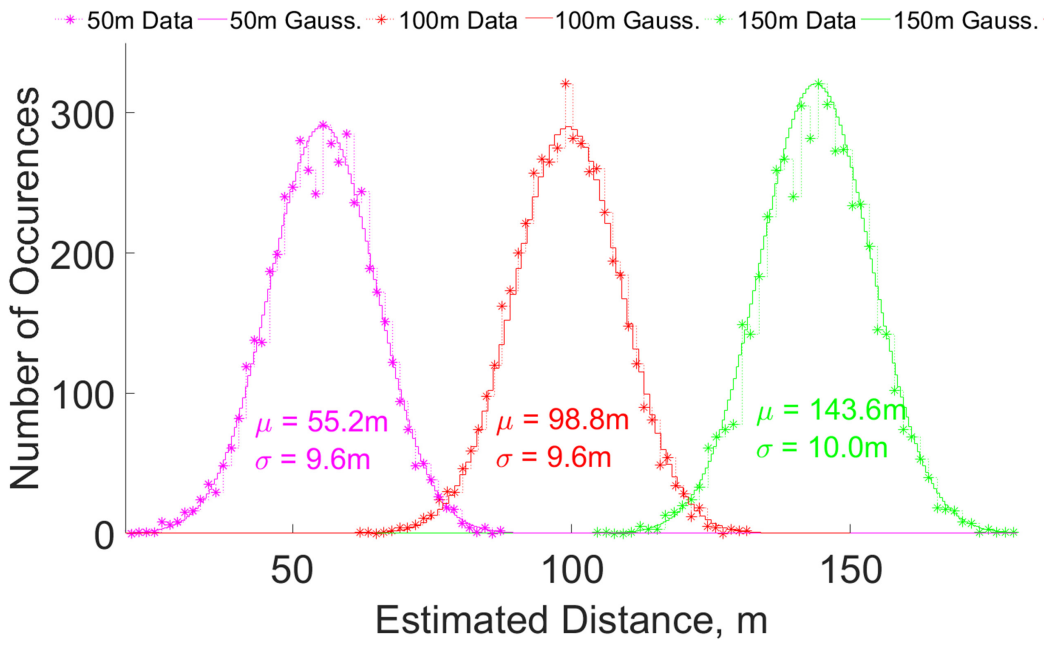

Figure 4.8: 5000 bootstrapped estimates of ^{137}Cs source standoff at r=50,100, and 150 m using a linear fit between r=0 and 200 m. Bootstraps contain the same number of counts as the initial measurements. Estimate distributions appear approximately Gaussian with standard deviations, σ and means, μ, inset into the figure.

information for absolute, 3-D localization is heuristically shown in Fig. 4.9. Compton imaging can be used to estimate incident source direction $(\hat{\theta}, \hat{\phi})$. Coded aperture or any other imaging modality can be used interchangeably in this step. Spectral perturbation is then used to estimate source-to-detector standoff $\hat{r}$. Given an estimated source standoff, $\hat{r}$, and source direction in spherical space, $(\hat{\theta}, \hat{\phi})$, 3-D source location relative to the detector is estimated via

$$\begin{aligned} \hat{x} &= \hat{r}cos(\hat{\theta})cos(\hat{\phi}) \\ \hat{y} &= \hat{r}cos(\hat{\theta})sin(\hat{\phi}) \\ \hat{z} &= \hat{r}sin(\theta). \end{aligned} \tag{4.3}$$

3-D analyses were conducted using CdZnTe detectors. Standoffs were estimated using 316/468 keV photopeak ratios for ^{192}Ir measurements at 200, 400 and 600 m. Dwell times were 606, 909 and 2211 seconds respectively for each distance. In

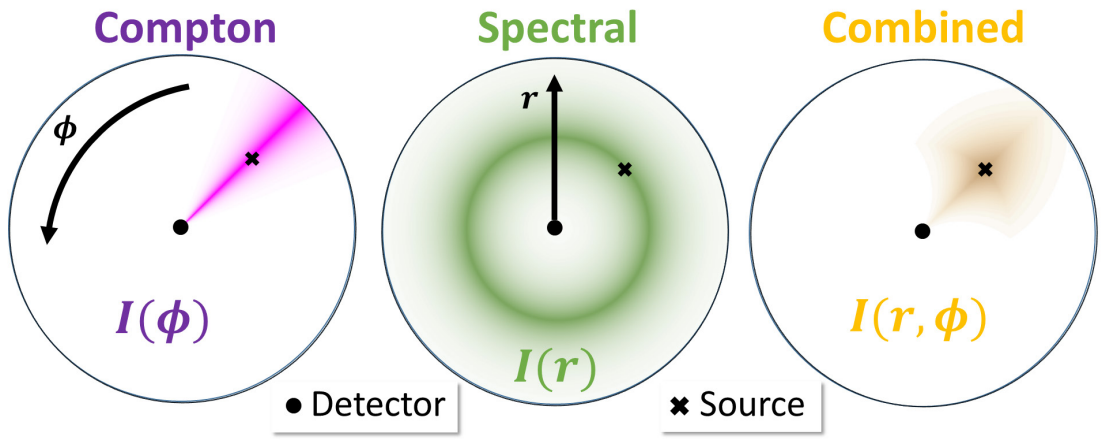

Figure 4.9: 3-D source localization process shown in 2-D for a source on the horizon such that $\theta = 90°$. (Left) Source directionality is estimated from Compton imaging by backprojecting reconstructed events away from the detector. The volume of the region subtended by the source Compton imaging PSF increases with increasing standoff r. (Middle) Source standoff estimated by atmospheric, spectral perturbations. A ring of positions are all consistent with observed spectral features. (Right) The combination of Compton imaging and spectral information for 3-D source localization.

all measurements the source appeared near the horizon, $\theta = \pi/2$, such that the estimated, 3-D distributions can be easily represented in polar form (r, ϕ). Estimated source location distributions with uncertainties from bootstrapping are shown in Fig. 4.10. Notably there was an estimated $\pm 5°$ uncertainty in detector rotational pose in all imaging measurements from limitations in positioning the pickup truck across a narrow road. Bounds of the bootstrapped distributions contained the true source location for all three measurements, showing that absolute, 3-D source location can be estimated from a single measurement view. Uncertainties in estimated ^{192}Ir standoffs from the CdZnTe system are larger than equivalent HPGe estimates in Fig. 4.6 due to the worse relative efficiency and energy resolution of the CdZnTe system.

4.2.2 Activity Estimation

With air density measured through conventional means, areal thickness can be converted to source-to-detector standoff through the air. Given an estimated standoff

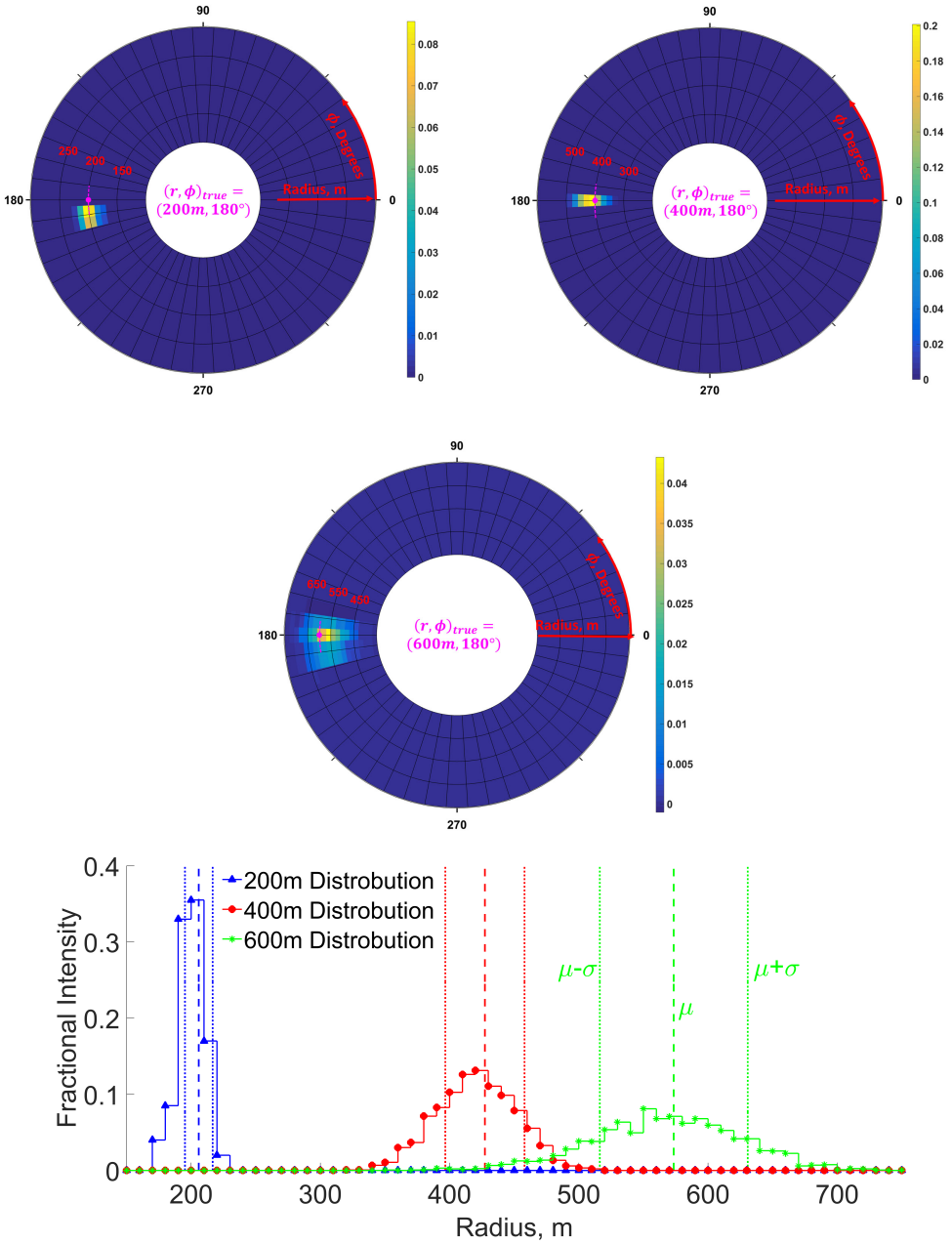

Figure 4.10: (Top) Distribution of relative, 3-D source locations computed using source standoff estimated via photopeak ratios and source directionality via Compton imaging at 200, 400 and 600 m. Dwell times were 606, 909 and 2211 seconds respectively. There was an estimated ±5° angular uncertainty in detector, rotational pose in each measurement. The best estimate of source locations are listed in the center of each plot while the dotted magenta line represents the bounds of uncertainty in angular pose. Histograms represent bootstrapped estimates of source location. Colormaps are independently scaled to maintain contrast. (Bottom) Plots collapsed to the radial dimension showing clear separation in estimated standoff. Mean estimated distance and standard deviation are marked with dashed and dotted lines respectively. Note uncertainty in depth increases at larger standoffs due to counting statistics.

$\hat{r}$ and count rate C of photopeak gamma rays at energy E in counts per second, source strength can be estimated via

$$\hat{I}(\hat{r}) = \frac{Ce^{\rho\frac{\mu(E)}{\rho}\hat{r}}}{f_{emit}\epsilon}\frac{4\pi\hat{r}^2}{A_{det}} \tag{4.4}$$

given a measured density of air ρ, photon yield of f_{emit} per decay, intrinsic detector efficiency ϵ at energy E, and detector surface area facing the source A_{det}. Note moderate uncertainty in estimated standoff $\hat{r}$ propagates to large uncertainty in estimated source strength.

A distribution of estimated source activity, made using standoffs estimated from bootstrapped CdZnTe spectra at 400 m, is shown in Fig. 4.11. The true source activity was within two, sample standard deviations of statistical uncertainty calculated via bootstrapping. The factor-of-two agreement between the mean, estimated source strength and reality is impressive considering that the solid angle, $\frac{4\pi\hat{r}^2}{A_{det}}$, and air attenuation, $e^{\rho\frac{\mu(E)}{\rho}\hat{r}}$, correction terms are on the order of 10^7 and 10^2 respectively. This illustrates that source activity, and therefore associated local dose rates, can be approximated from a single, far-field measurement.

Long-range estimates of 3-D source location and intensity can be overlaid on maps to provide contextual information for emergency response. Results from the 400 m ^{192}Ir measurement are overlaid on a terrain map in Fig. 4.12. Conservative estimates of spatial dose rates, neglecting attenuation from buildings, are overlaid on the map. Although estimates of 3-D source location, activity and dose are imperfect, they are sufficiently detailed to guide emergency response. For example, it is clear that there is a large source somewhere near the center of the compound. Furthermore, this information was gathered in a almost 'dose-free' manner; the relative dose rate and cumulative dose were well below 1 mR/h and 0.125 mR respectively.

This long-range approach fundamentally differs from traditional techniques taught

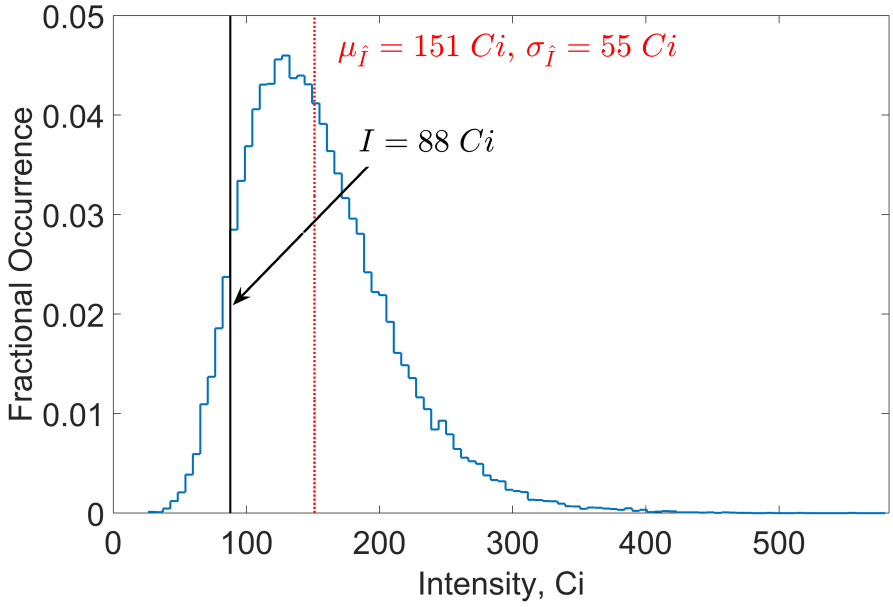

Figure 4.11: Estimated activity distribution for an 88 Ci ^{192}Ir source using the 316 keV photopeak count rate and standoffs estimates at 400 m generating using a CdZnTe detector. Uncertainty in photopeak counts was less than 2%, showing standoff uncertainty dominates uncertainty in activity estimation.

to first responders. First responders are taught to record relative dose rates at specific spatial coordinates using simple detectors. After an individual measurement the responder turns 360°, keeping the detector close to their chest, to act as a simple rotational collimator. They then walk some distance towards the direction, that when shielded by their body, produced the biggest reduction in recorded dose rate [90]. This technique is repeated several times, while dose rates and coordinates are constantly shared with a central command, until the source is localized. This traditional search using non-imaging detectors has many first responders walk towards a source of unknown strength and location. This exposes many responders, in contrast to only one using an imaging detector, to an unknown, and potentially dangerous, dose. Furthermore standoff detection limits first responder exposure to non-radiation hazards, such as fire, smoke or debris, that will come with the detonation of a RDD. Therefore standoff detection using an imaging detector enables 'low-risk' information gathering,

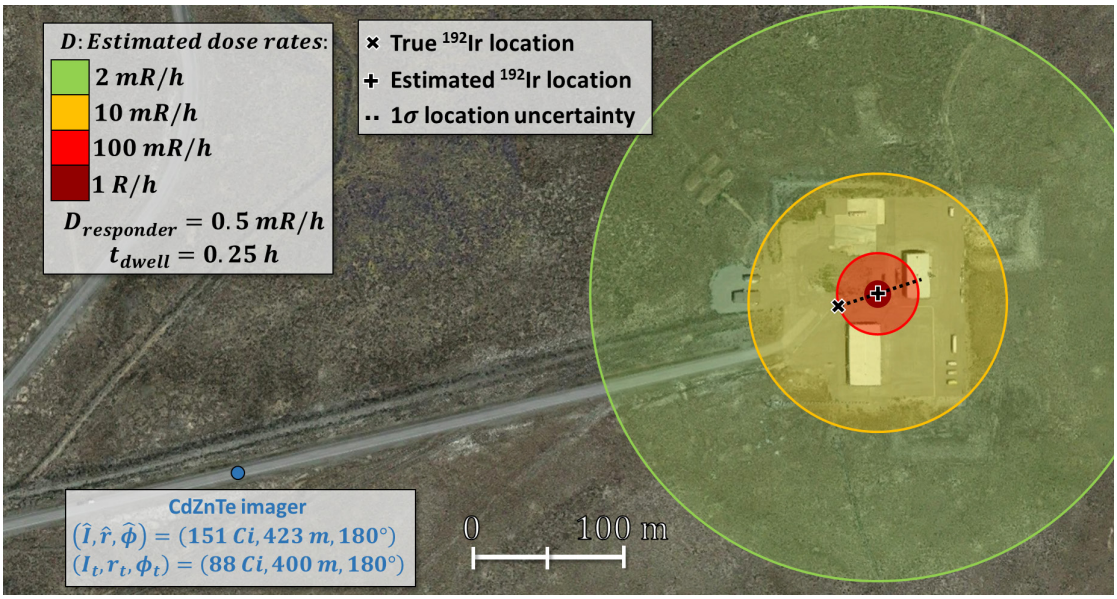

Figure 4.12: Estimated 3-D source position relative to the CdZnTe array. Conservative estimates of spatial dose rates can be inferred from estimates of activity given the standard ^{192}Ir dose rate of 0.55 R h^{-1} Ci^{-1} at 1 m and $1/r^2$. Note the dose rate for a first responder using the CdZnTe imager is only 0.5 mR/h, well outside the 'cold zone', or 'low-radiation-zone boundary' discussed in [13] and [91].

minimizing the first responder risk in unknown, potentially dangerous, situations.

4.2.3 Source Localization with Scattered Gamma Rays

Spectral evidence of air scatter is complimented by Compton imaging reconstructions as shown in Fig. 4.13. Compton imaging incomplete-energy-deposition gamma rays, without the presence environmentally-down-scattered flux, produces an annular ring around the true source location which broadens with decreasing gamma-ray energy [55]. This behavior is seen for near-field sources in the top panel of Fig. 4.13. In the case of air down-scatter, gamma rays predominantly originate from the source direction. Complete-energy-deposition, air-scattered gamma rays produce a broadened hot spot in the rough, source direction. These air-downscattered gamma rays deposit similar energies to uncollided gamma rays that outscatter, without depositing their entire energy, from the detector. When summed together, these two gamma-ray

populations produce a source hot spot from air scatter superimposed on annular ring from incomplete deposition events. This behavior is seen for far-field sources in the middle-panel of Fig. 4.13. Therefore off-photopeak, Compton images also encode information on source-to-detector distances.

The influence of incomplete-energy-deposition events can be subtracted from reconstructed Compton imaging PSFs to focus on atmospherically scattered events. This was attempted for a far-field source in the bottom-panel of Fig. 4.13. A previously measured PSF with no air scatter, $I_{psf}(\theta, \phi, E)$, can be subtracted off from an arbitrary measurement with air scatter, $I_{mes}(\theta, \phi, E)$, to isolate air scatter alone, I_{as}, via

$$I_{as}(\theta, \phi, E) = I_{mes}(\theta, \phi, E) - C \cdot I_{psf}(\theta, \phi, E) \tag{4.5}$$

where C, the incomplete-energy-deposition scaling factor, can be approximated by the ratio of imaged intensity across photopeak energy bins E_{PP} at the source direction (θ_s, ϕ_s)

$$C \simeq \frac{I_{mes}(\theta_s, \phi_s, E_{PP})}{I_{psf}(\theta_s, \phi_s, E_{PP})}. \tag{4.6}$$

Note this approximation assumes there is only a single source. This enables the more robust localization of sources via air-scatter gamma rays.

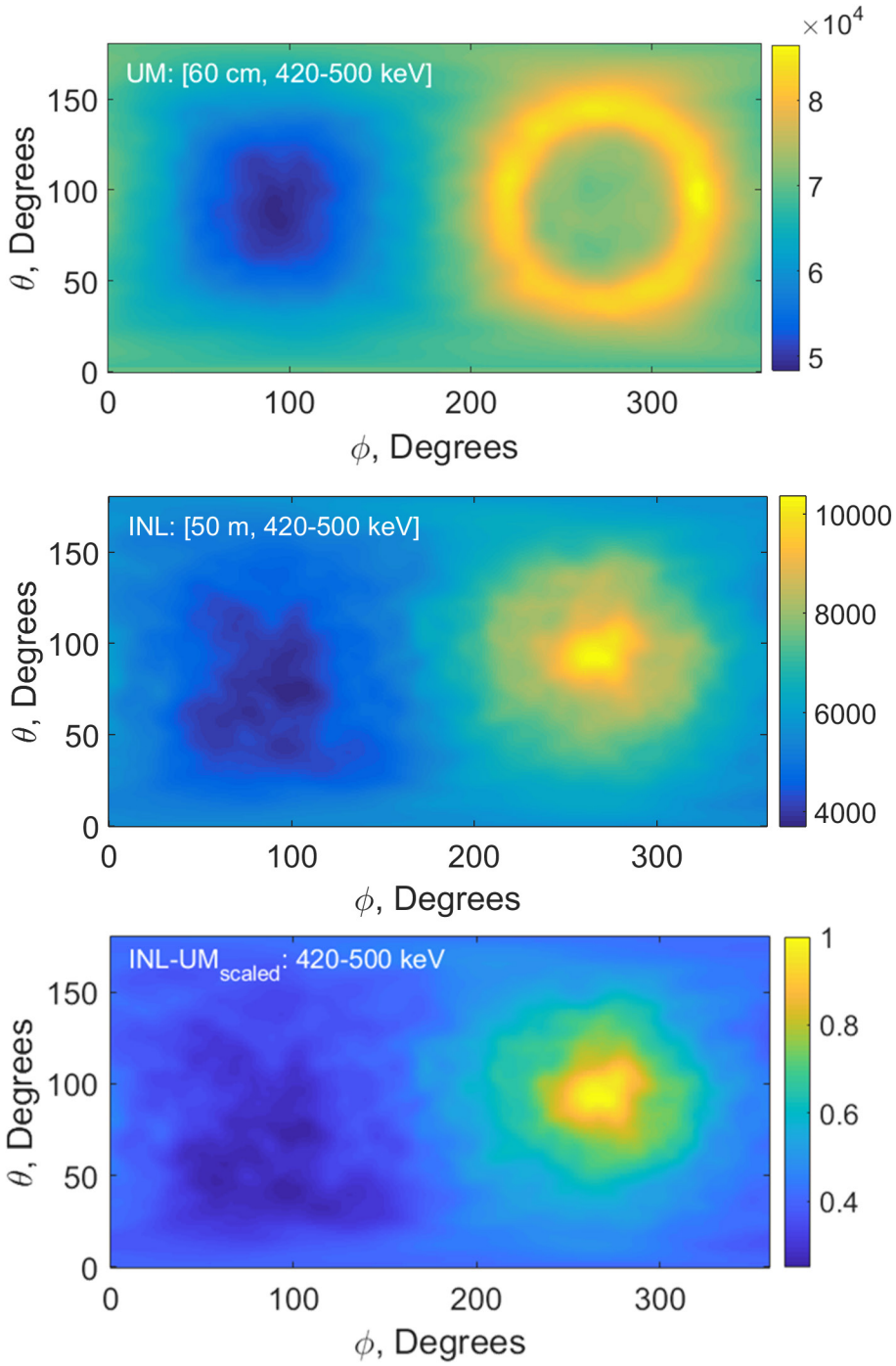

Figure 4.13: (Top) Near-field Compton imaging PSF for incomplete-energy-deposition events between 420-500 keV for a ^{137}Cs source. The calculated Compton scatter angle, which assumes complete energy deposition, is incorrect and forms an annular hot spot around the true source location at $(\theta, \phi) = (90, 270)°$. This incomplete-energy-deposition behavior has been studied extensively by *Chu* [55]. (Middle) Far-field Compton imaging PSF that includes the summation of incomplete-energy-deposition and air-scattered gamma rays. (Bottom) Far-field Compton imaging PSF after subtracting off estimated, incomplete-energy-deposition events.

These Compton-down-scattered gamma rays can be leveraged to more rapidly localize an unknown source. This is possible as down-scattered flux originates from predominately the source direction. This is particularly important in large-standoff, source localization scenarios where the buildup factor, the ratio of total-to-unscattered flux, can be larger than five or more [92]. CdZnTe Compton images were reconstructed with different spectral windows that contained a) only photopeak and b) photopeak plus down-scattered gamma rays for ^{192}Ir measurements. When using scattered data, all multi-pixel events from $E = [200 - 615]$ keV were imaged. The 200 keV low-energy cut was chosen to include down-scattered gamma-ray emissions from ^{192}Ir at 295, 308 and 316 keV. Furthermore, gamma rays below 200 keV do not produce quality Compton images in this specific CdZnTe system as the outgoing, scattered gamma rays do not travel very far, compared to size of detector pixelization, before subsequent absorption. Measurements were bootstrapped and Compton images were repeatedly reconstructed for various dwell times at each source distance using the two different spectral windows. The standard deviation of the bootstrapped source direction estimates for each dwell time and standoff were computed to compare relative, angular localization uncertainties. For short, equivalent detector dwell times, uncertainty in the reconstructed source direction was generally decreased by including scattered gamma-rays for ^{192}Ir measurements, which is illustrated in Fig. 4.14. Intuitively these down-scattered, non-photopeak gamma rays still contain rough, directional information to aid in point source localization when reconstructions are count starved. However, this trend was reversed for long integration times in high-count measurements, such as during the 200 m ^{192}Ir measurement, where slightly degraded source uncertainty was seen. This behavior may be explained by the degraded imaging response of scattered and partial energy deposition gamma rays where the reconstructed PSF of scattered gamma rays had a degraded angular FWHM. In practice this degradation, less than a few degrees, will be unimportant as less than

5° angular uncertainty is sufficient to localize a source.

4.3 MCNP Simulation of Shielded Sources

All previous analyses assumed there was only air between the gamma-ray source and radiation detector. However, sources are commonly surrounded by solid shielding in practical measurement scenarios. This 'local-shielding' modulates photopeak and Compton down-scatter ratios before atmospheric transport, complicating estimation of source standoff.

Simultaneous estimation of local-source shielding and air standoff was attempted for an ^{192}Ir source using MCNP6 simulation. Spherical, local shields of various materials and thicknesses were placed around the source. Local shielding materials were limited to lead, iron and aluminum for simplicity. Simulated lead thicknesses included 0.5, 1, 2 and 3 cm. Aluminum shields spanned 1-10 cm with 1 cm steps. Iron shields spanned 1-10 cm with 1 cm steps. All sources were simulated 3.5 m above the ground. An outline of the employed algorithm is provided in Fig. 4.15. Given a set of photopeak and scatter ratios measured for an unknown geometry, several independent estimates of standoff x_{air} are made assuming a bare source. This is shown in Fig. 4.16. If the standoff estimates are consistent, a bare source is assumed. If not, a secondary check to see which combination of local shields and standoffs agrees most with observations is made. Agreement between observations and lists of hypothesized shields can be quantified considering N_{PP} photopeak and N_C Compton ratios. $\boldsymbol{O}$, the observation vector that lists all measured photopeak and Compton ratios, and $\boldsymbol{S}_i$, the vector of expected photopeak and Compton ratios for standoff-shielding combination i, was defined by the Euclidean distance D

$$D(\boldsymbol{O}, \boldsymbol{S}_i) = \sqrt{\sum_{j=1}^{N_{dim}} (O(j) - S_i(j))^2} \tag{4.7}$$

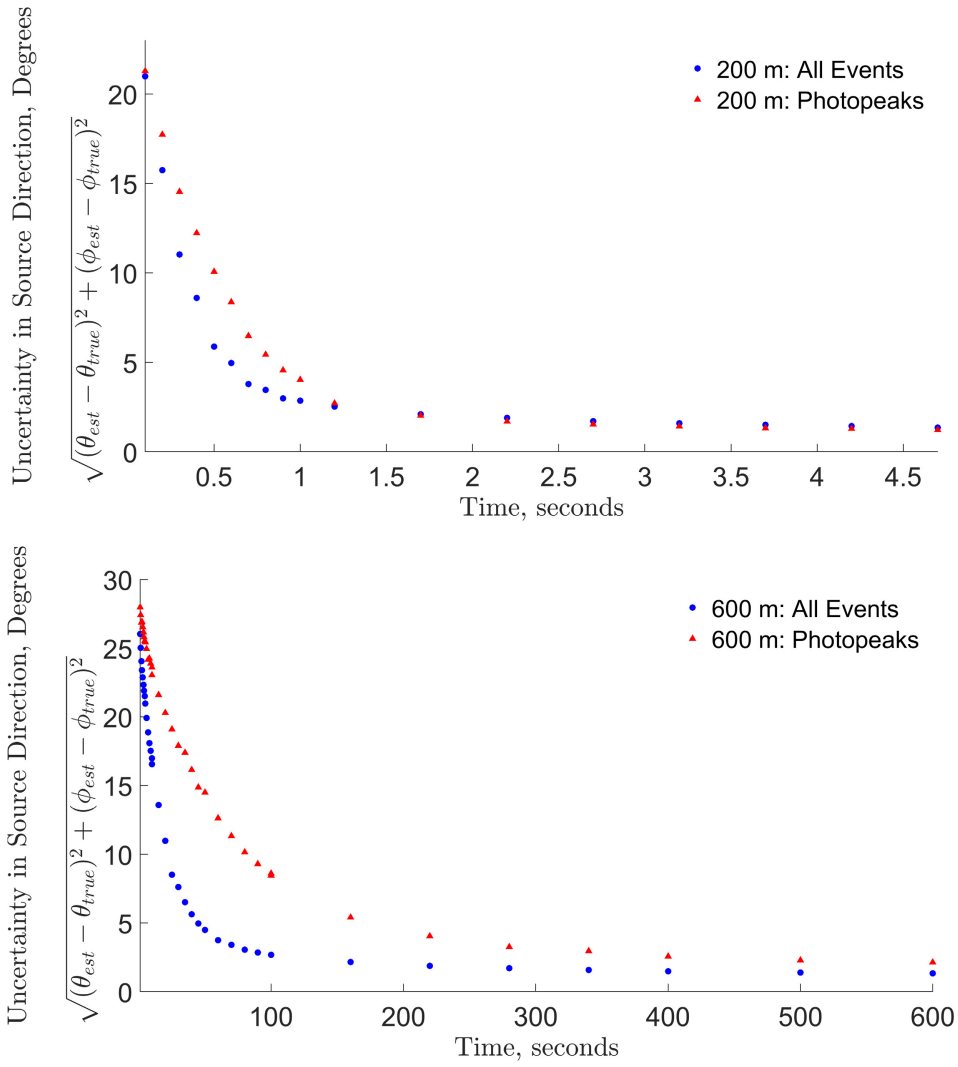

Figure 4.14: Uncertainty in 2-D Compton reconstructed source location as a function of dwell time using only photopeak and photopeak plus scattered gamma rays at 200 (top) and 600 (bottom) m for ^{192}Ir measurements using the CdZnTe imager. Error bars are smaller than plotted points. Note that uncertainty decreases more slowly at larger standoffs due to fewer source counts. The photopeak energy windows were $E = [287-299, 302-320, 456-470, 479-486, 580-590, 596-615]$ keV while the photopeak plus scatter window spanned $E = [200, 615]$ keV.

where N_{dim} corresponds to the cumulative number of photopeak and Compton ratios considered. Small distance $D(\boldsymbol{O}, \boldsymbol{S}_i)$ can be heuristically interpreted as strong agreement between observations and expectations given hypothesized local-shielding and standoff parameters i.

Euclidean distances from MCNP simulation of shielded ^{192}Ir sources are shown in Fig. 4.17. Measured photopeak and Compton ratios appear similar for many disparate local shielding and air standoff combinations. For example, photopeak and Compton ratios through 1 cm of aluminum at an air standoff of 100 m appear similar to bare source cases at an air standoff of 130 m. Similar ambiguity is seen for 2 cm of aluminum shielding at an air standoff of 70 m. This ambiguity suggests that it is difficult to separate the presence of aluminum shielding from air standoff. Similar ambiguity was seen for iron shielding where either air or aluminum can be interchanged to produce similar spectra. Contrastingly, in lead-shielded scenarios, combined-source standoff and local shielding can be simultaneously estimated with little ambiguity. This is unsurprising given the substantially different, energy-dependent attenuation of lead compared to the other materials. This suggests that simultaneous estimation of air standoff and local shielding is only feasible in limited cases, such as for high-Z shields.

Combined local shielding and source standoff estimation can be approached using directional gamma-ray spectra. Gamma rays emitted inside some local shield may Compton scatter. These Compton scattered photons, including those which undergo large-angle scatter, will eventually leak out the surface of the shielding. These shielding-scattered photons then propagate through the air to the detector. For bare sources, the majority of photons incident on the detector surface from the source direction are either uncollided or small-angle scattered. Photons that Compton scatter in local shielding originate from the same source direction at lower than emitted energies. Therefore directional spectra from source directions may be much softer

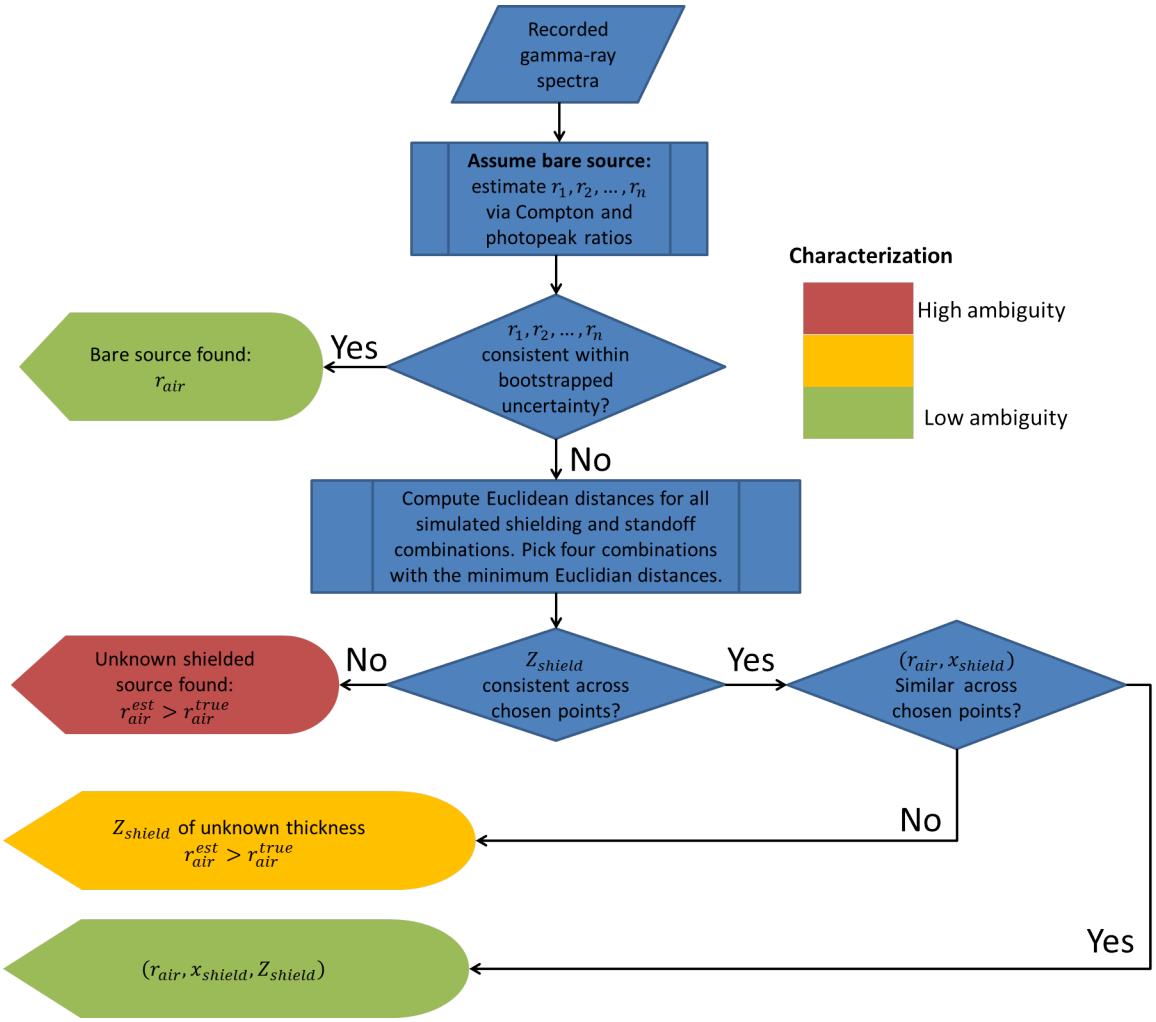

Figure 4.15: Algorithmic logic for combined local-shielding, (x_{shield}, Z_{shield}), and air standoff, r_{air}, estimation. Results have differing levels of ambiguity ranging from detailed problem characterization (green) to simply acknowledging the presence of some type of shielding (red).

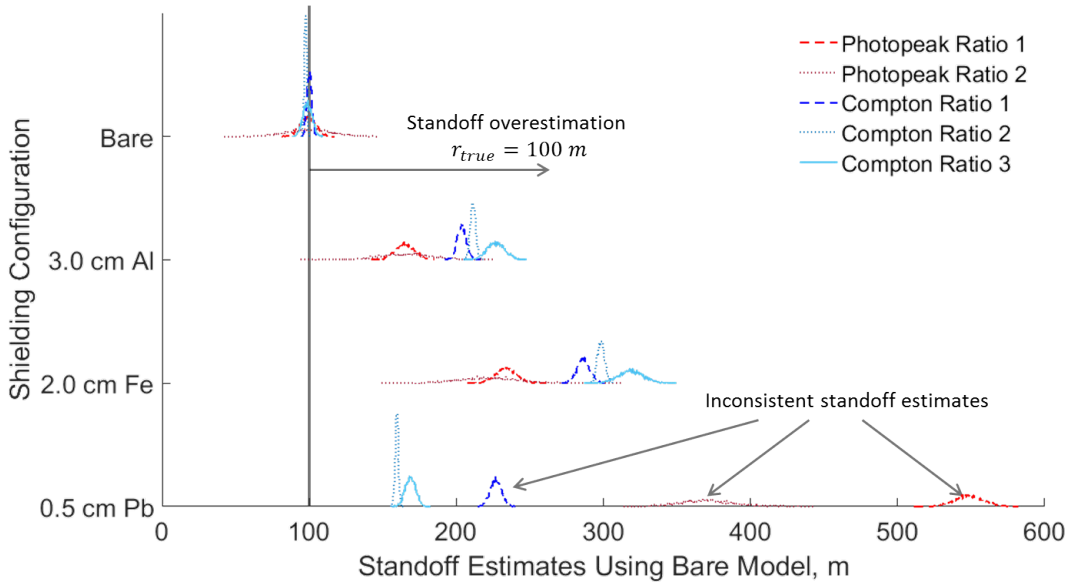

Figure 4.16: Bootstrapped standoff estimates of bare and shielded sources through 100 m of air using several photopeak and Compton ratios. Bootstrapped spectra contain $3{\cdot}10^5$ recorded photons and standoff is estimated using a model that assumes no local shielding. Standoffs using different photopeak and Compton ratios are inconsistent for shielded sources due to model mismatch, suggesting the presence of local-shielding. Extra attenuation from local-shielding causes systematic, overestimation of standoff. The scale of mismatch that can be detected decreases with increasing counting statistics as distributions tighten.

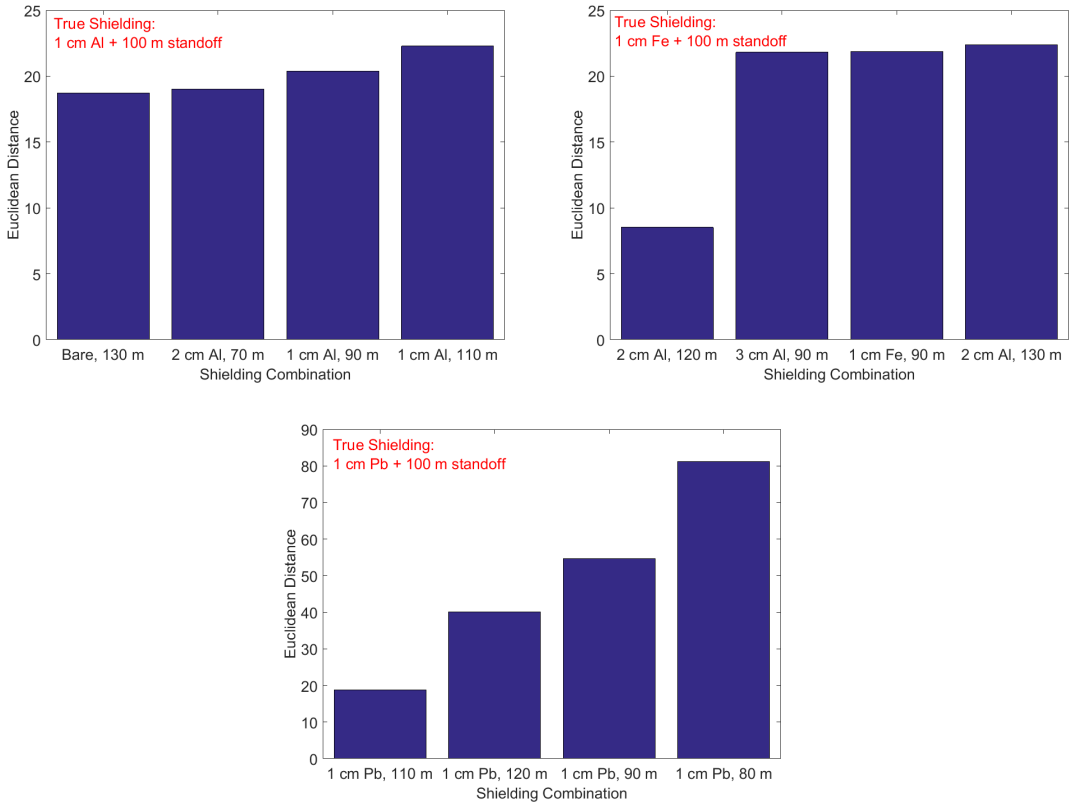

Figure 4.17: Local shielding and air standoff combinations with the smallest Euclidean distance to the true configuration listed in red. (Top left) Air standoff and aluminum thickness appear relatively degenerate. (Top right) Aluminum and iron shielding cases also appear degenerate by varying air standoff. (Bottom) Lead and air standoff can be unambiguously estimated.

in energy for shielded than bare sources. This technique may be used to resolve degenerate cases of low-Z shielding and additional air standoff.

4.4 Measurement of Gamma-Ray Skyshine

Optically-opaque objects, such as buildings or hills, may attenuate all photons along the direct line-of-sight between the source and detector. In these heavily shielded scenarios, with no direct photon path between the source and detector, no photopeaks are expected. However, gamma rays that travel around the optically-opaque shielding can still be recorded. Air serves as one such scattering medium. The atmospheric scattering of gamma rays, known as skyshine, has been studied extensively for radiation portal monitors, nuclear power plant dose and prospecting for uranium ore [93–95]. For source search scenarios, skyshine can be leveraged to localize heavily shielded sources without a direct line-of-sight.

Skyshine measurements were conducted on August 18$^{\text{th}}$, 2018 at Idaho National Laboratory. A strong, 83 Ci ^{192}Ir source was placed into a 6-inch-thick, lead collimator. The collimator had a 4" opening and was 18" long, corresponding to a 6.3° half-opening angle, in a silo-geometry. The collimator thickness was chosen such that air-scattered flux was many times stronger than flux leaking through the shielding at energies of interest. A commercial, H3D H420 detector measured the collimated setup at source-to-detector standoffs of 25, 50, 75, 100 and 150 m [96]. The collimator and recorded spectra are shown in Fig. 4.18. Note the spectra contain little-to-no photopeaks. Low-energy, coded aperture images of air-scattered ^{192}Ir gamma rays show a clear beam of scattered flux above the collimator opening. Using these air scattered gamma rays the unknown source direction can be clearly measured.

Assuming only single scatters, each point along the beam path should have a unique energy spectrum from the downscatter of many ^{192}Ir emissions. Gamma rays that scatter at the base of the beam, near the collimator opening, undergo a smaller-

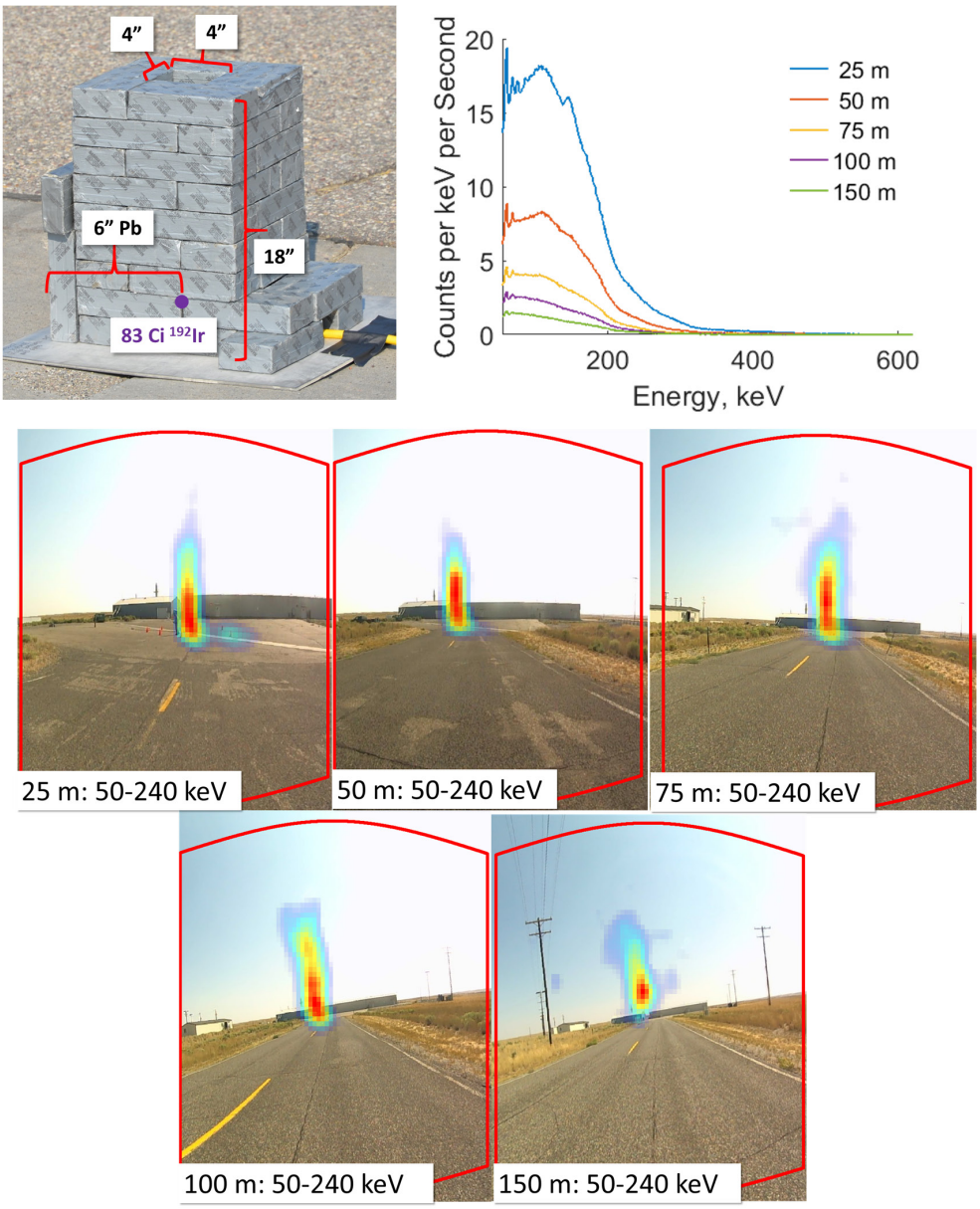

Figure 4.18: A roughly 83 Ci ^{192}Ir source was placed into a 6” lead collimator. Coded aperture images, using a H420 system, were generated as a function of standoff using all 50-240 keV gamma-rays. Clear beams of air-scattered gamma rays are seen above the collimator. Radiation images pixels with intensity less than 50% of the maximum were omitted. No appreciable photopeaks are detected through the collimator.

angle-scatter than those towards the top of the beam. As such, detected gamma-ray spectra from the top of the beam is 'softer' than the bottom. This inverse correlation between Compton scatter angle and outgoing photon energy is seen in Fig. 4.19 at a source-to-detector standoff of 25 m. The true angle-energy correlation from Compton scattering is obfuscated by the polyenergetic nature of ^{192}Ir. Simplified analysis was conducted by approximating the polyenergetic spectra with a single emission. The strongest emission in the triplet from 295-316 keV, which comprises roughly 70% of total emissions, at 316 keV was chosen to approximate the spectra. Air-scattered gamma rays at the base of the collimator Compton scatter through 90°. This corresponds to an expected, outgoing energy of roughly 195 keV. This calculated value agrees with observation in Fig. 4.19. Some underestimation in outgoing, scattered photon energy can be explained by other, higher-energy ^{192}Ir emissions that were omitted in the simplified spectra.

4.5 Conclusions

Air is ubiquitous in measurement of radioactive sources. The low-Z and low-density of air allows the atmospheric transport of gamma rays over hundreds of meters. The predictable modulation of photopeak ratios and Compton downscatter of photopeak flux can be used to estimate gamma-ray source standoff using a single measurement. Standoff from spectra and directionality from imaging can be combined to estimate relative, 3-D source location. Estimated standoff can be used to correct for atmospheric attenuation and solid angle to estimate source strength. Furthermore, air-scattered gamma rays appear to offer coarse, directional information that can be leveraged when localizing a gamma-ray source through several MFPs of air. Local shielding around a source complicates estimation of standoff. MCNP simulations of shielded ^{192}Ir sources suggest that simultaneous estimation of air standoff and local-shielding parameters is only feasible for high-Z shields. In cases of heavily

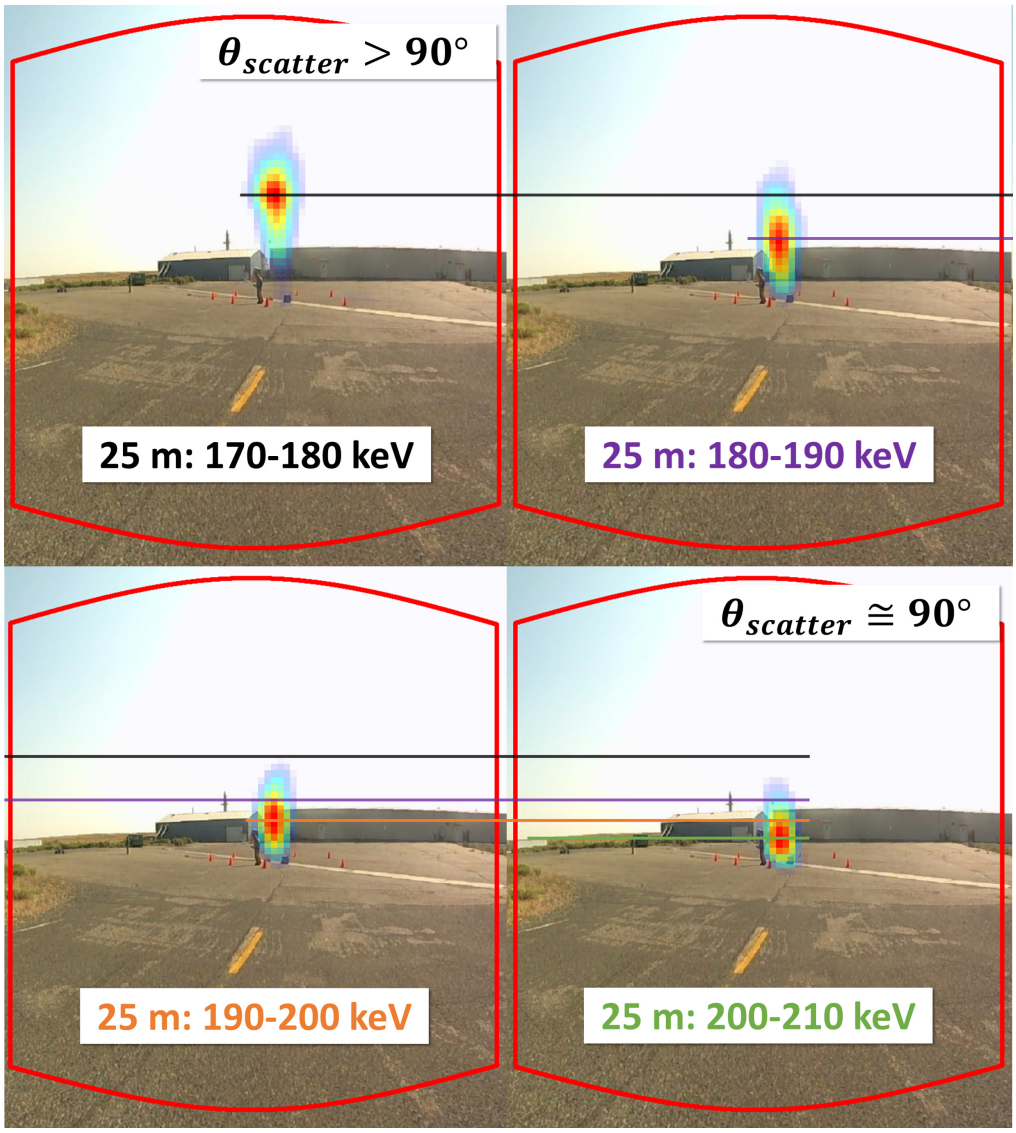

Figure 4.19: Energy-dependent coded aperture reconstructions of air-scattered gamma rays above a lead collimator at a source-to-detector standoff of 25 m. Air scattered spectra from the base of the beam are harder due to the negative correlation between Compton scatter angle and outgoing gamma-ray energy. Color coded lines at the center of each reconstruction are added to guide the eyes.

local shielding, where there is no direct line-of-sight, sources can be localized through skyshine. These novel, experimentally-demonstrated techniques can be used to extract information from large, black-boxes encountered in emergency response.

CHAPTER V

Airborne Localization

5.1 Mobile Source Search

3-D source localization from a single, far-field, gamma-ray imaging measurement is complicated by limited detector parallax. Limited parallax manifests as standoff ambiguity along radial directions away from the detector. Single-view, standoff ambiguity was previously addressed by decoding the standoff-dependent, atmospheric perturbations in gamma-ray spectra. In contrast, quick measurements can be taken from many different locations. Using measurements from many different locations can be thought of as using a larger, single detector. The near-field, where different parts of the detector view the source from different angles, of this large detector extends further, enabling 3-D source localization in scenarios with larger standoffs. Therefore, mobile detector systems offer increased parallax which can be used to localize gamma-ray sources in 3-D space.

Detector systems have been mounted across a variety of platforms. A small subset of platforms include hand-held systems, human-piloted airborne systems for consequence management, and autonomous drones [97–100]. Recently, a large-volume, 3-D CdZnTe system attached to a remotely operated robot successfully localized multiple gamma-ray sources inside a room [101]. Mobile, CdZnTe-based systems mounted to Stryker armored personnel carriers are also under development [102]. This work

focuses on processing data collected from a large-scale, > 4 km^2, proof-of-concept airborne measurement gathered using 3-D, pixelated CdZnTe systems.

H3D A400 [103] and H420 [96] CdZnTe detectors were flown in a commercial helicopter around a bare, 83 Ci ^{192}Ir radiography source at Idaho National Laboratory (INL). The bare radiography source was elevated roughly 1 m above the ground using a tripod. The helicopter flight path and elevation were recorded using a high-accuracy GPS at one second increments. Instantaneous helicopter bearings were not directly measured. As such, instantaneous bearings, which correspond to helicopter rotational pose, were estimated by differentiating subsequent position measurements.

The helicopter flight was broken down into two portions. The first portion was flown at roughly 40 knts at an elevation of 400 ft. It consists of passes directly over the radioactive source, a cloverleaf pattern centered over the source and several orbits around the source at various radii. The second portion was flown at an elevation of 1600 ft at 40 knts and consisted of cloverleaf and circular patterns centered at the source, followed by hovering directly over the source. Detector count rates at 1600 ft were an order of magnitude lower than at 400 ft. As such, this work focuses on the 400 ft dataset which has relatively better statistics. The source geometry and helicopter flight path for the 400 ft dataset are shown in Fig. 5.1

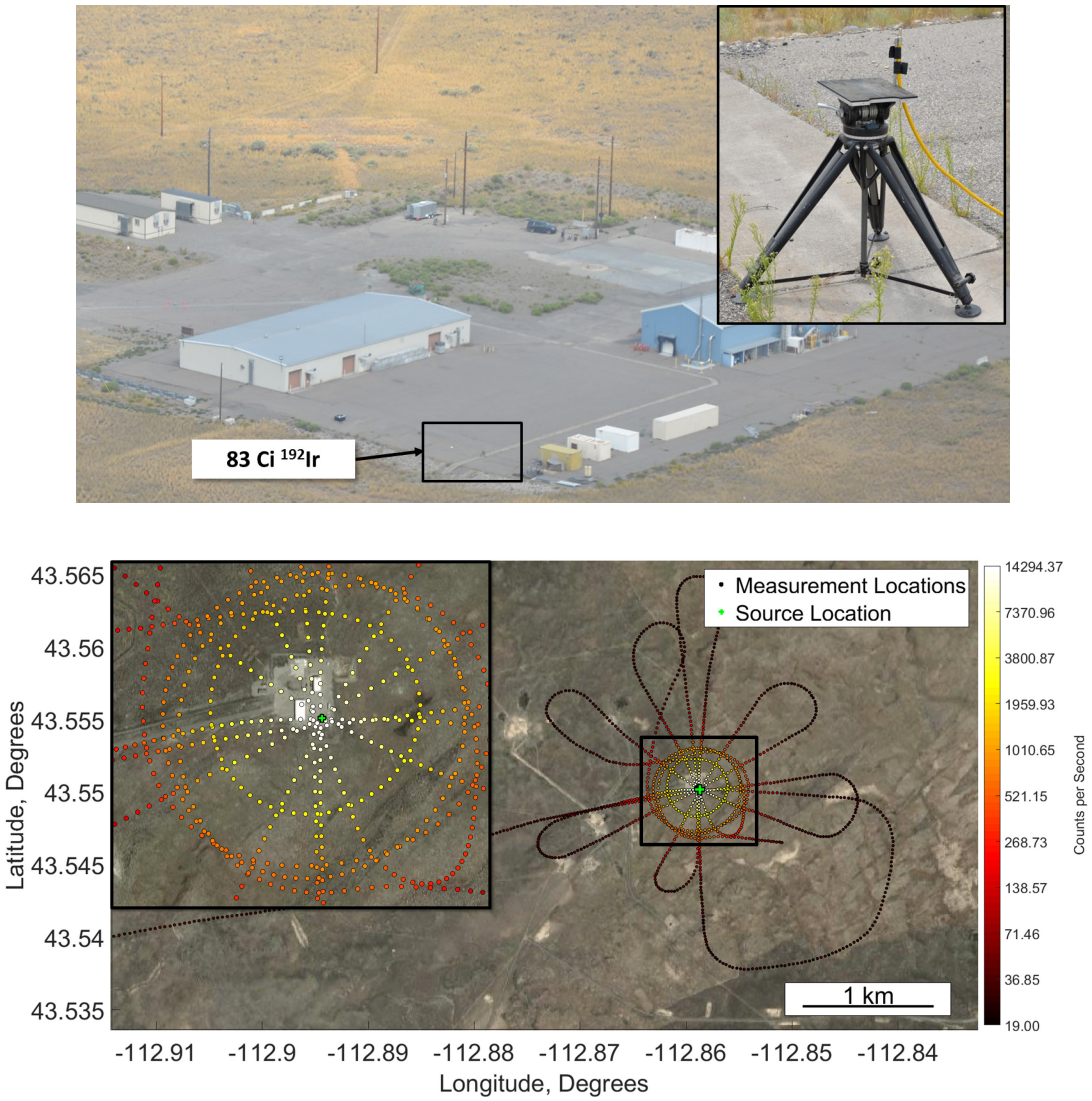

Figure 5.1: (Top) Measurement setup where the bare, 83 Ci ^{192}Ir source was placed on a tripod towards the edge of the compound. (Bottom) H3D A400 count rates taken at 1 second intervals along the flight path at 400 ft. Detector latitude, longitude and elevation were measured via GPS. A clear peak in detector counts for samples around the source is seen.

A400 and H420 H3D detectors were configured differently during the flight. The A400 was placed on the helicopter floor, with cathodes facing towards the ground in a consistent orientation throughout the entire flight, while the H420 was gimbaled around such that its cathodes continually faced towards the source. The H420 saved optical images at roughly 0.25 Hz while Compton images were reconstructed with

data from one second before and after each optical image. The A400, which was kept in consistent orientation with the helicopter throughout the flight, generated gamma-ray spectra at 1 Hz.

5.2 Localization Techniques

Gamma-ray count rates increase for measurements near a source due to increased solid angle and reduced atmospheric shielding. These location dependent count rates encode information on relative source standoffs. Generally, measurements from multiple locations are combined using $1/\mathrm{r}^2$ to localize a source. Imaging offers additional information beyond standoff in the form of source directionality. For example, the spatial distribution of counts within a position-sensitive detector encodes information on source directionally. These two different source localization techniques, which use $1/\mathrm{r}^2$ and imaging information respectively, are discussed below.

5.2.1 $1/\mathrm{r}^2$-Based Localization

Count rates fall off as $1/\mathrm{r}^2$ where r is the source-to-detector distance assuming that the effects of air attenuation are small compared to relative solid angle. As such, the detector sensitivity, ϵ, to gamma-ray emissions from some point on the ground (x, y) across an entire flight path is the simple summation of time-weighted responses

$$\epsilon(x, y) = \sum_{i=1}^{T} \frac{\Delta t(i)}{r(x, y, i)^2} \tag{5.1}$$

where $r(x, y, i)$ is the distance between the ground point and the detector at the i^{th} sample, $\Delta t(i)$ is the time spent at i^{th} sample and there are T total measurements. Given some position-dependent count rate, a sensitivity-weighted, simple-

backprojection can be made via

$$I(x,y) = \frac{1}{\epsilon(x,y)} \sum_{i=1}^{T} \frac{C(i)}{r(x,y,i)^2} \tag{5.2}$$

where $C(i)$ is the count rate recorded by the detector at the i^{th} time step. The maximum of the simple-backprojection image across all possible points (X, Y)

$$(\hat{x}, \hat{y}) = \underset{(X,Y)}{\operatorname{argmax}}\{I(x,y)\} \tag{5.3}$$

is then chosen as the estimated source location $(\hat{x}, \hat{y})$.

5.2.2 Centroid-Based Localization

Imaging information can be used to localize a gamma-ray source. One simple imaging technique, called centroiding, is commercially available on detectors such as the H3D A400 for gamma-ray source localization. The centroid method assumes that the count-weighted centroid in some position-sensitive detector is displaced from the geometric centroid along the direction of incident photons. However, centroid estimates are not directly accessible from H3D software after a measurement. Therefore, a simple centroiding technique was implemented using raw data. Count-weighted displacement from the geometric centroid for each time step t was calculated via

$$\begin{aligned} x_{cen}(t) &= \frac{\sum_{j=1}^{J}\sum_{i=1}^{I}(x(i,j) - x_0)C(i,j,t)}{N_{photons}} \\ y_{cen}(t) &= \frac{\sum_{j=1}^{J}\sum_{i=1}^{I}(y(i,j) - y_0)C(i,j,t)}{N_{photons}} \end{aligned} \tag{5.4}$$

given the geometric detector centroid (x_0, y_0), $N_{photons}$ recorded photons, the spatial distribution of recorded counts $C(i,j,t)$ and pixel coordinates $y(i,j)$ and $x(i,j)$ [59].

For the A400 J and I both correspond to 22; the system consists of a 2 x 2 array of 11 x 11 pixelated detectors. Calculation of the vertical centroid, z_{cen}, was omitted. For succinctness, the vector $(x_{cen}(t), y_{cen}(t))$ was reduced to the vector $\boldsymbol{v_{cen}}(t)$ that points azimuthally around the detector. Centroids were computed using all recorded counts, independent of energy, as a majority of source gamma rays had interacted in the roughly 400 ft of air or helicopter chassis before detection.

The coarse, 2-D estimates of source direction computed for each measurement location were then combined on a common grid. First, the direction between the helicopter and all points on the ground (x, y) were calculated

$$\boldsymbol{r}(x, y, t) = [x - x_{heli}(t), y - y_{heli}(t)] \tag{5.5}$$

where $x_{heli}(t)$ and $y_{heli}(t)$ represent the helicopter location as a function of time t. The cumulative, angular distance between all centroid pointers $v_{cen}(t)$ and ground directions $\boldsymbol{r}(x, y, t)$ was computed by

$$D(x, y) = \sum_{t=1}^{N_t} \boldsymbol{v}_{cen}(t) \cdot \boldsymbol{r}(x, y, t) \tag{5.6}$$

given N_t measurements. Assuming a single source, the true source position should be consistent with all estimated direction vectors. In other words, the cumulative angular distance $D(x, y)$ should be small for the true source position. As such, the point with the minimum, cumulative pointer distance was chosen as the source location

$$(\hat{x}, \hat{y}) = \underset{(X,Y)}{\operatorname{argmin}}\{D(x, y)\} \tag{5.7}$$

where (X, Y) represents all possible ground points in 2-D space.

Measurements were bootstrapped and repeatedly reconstructed using both techniques to quantify reconstruction uncertainty and bias. For each bootstrap, a 2-D

estimate of the source location $(\hat{x}, \hat{y})$ was generated. Many bootstrapped estimates from each technique were then histogrammed. Standard deviations of the resulting distributions were used to quantify uncertainty while shifts in the mean, relative to the true value, were used to quantify bias.

5.3 Source Localization Performance

Measurements were processed in two ways. First, the entire flight path was used. This flight path contains many samples directly above the source. Second truncated flight paths, without measurements above the source, were processed. The relative results for each case are discussed below.

5.3.1 Complete Flight Path

Measurements coordinates and the corresponding count rates from the flight path at 400 ft are shown in Fig. 5.1. As expected, the recorded count rate increases with decreasing source standoff due to enhanced fractional solid angle and reduced atmospheric attenuation. Simple-backprojection results using the framework discussed in Eq. 5.2 are shown in Fig. 5.2. The sensitivity image, $\epsilon(x, y)$, used to scale simple-backprojection results closely resembles the time-weighted, helicopter flight path. Both non-normalized and sensitivity-scaled simple-backprojections were largest near the true source location, successfully localizing the source in 2-D space. This was unsurprising given how sharply the gamma-ray count rate peaks over the source and that the source was passed from many angles.

Location uncertainty in the $1/r^2$-based reconstruction was probed by bootstrapping the original measurement. All bootstrapped estimates returned the same location, suggesting that statistical uncertainty in reconstructed source position was smaller than the 20 x 20 m^2 pixel used in this analysis. This experimentally demonstrates that a $1/r^2$-based simple-backprojection reconstruction can effectively localize

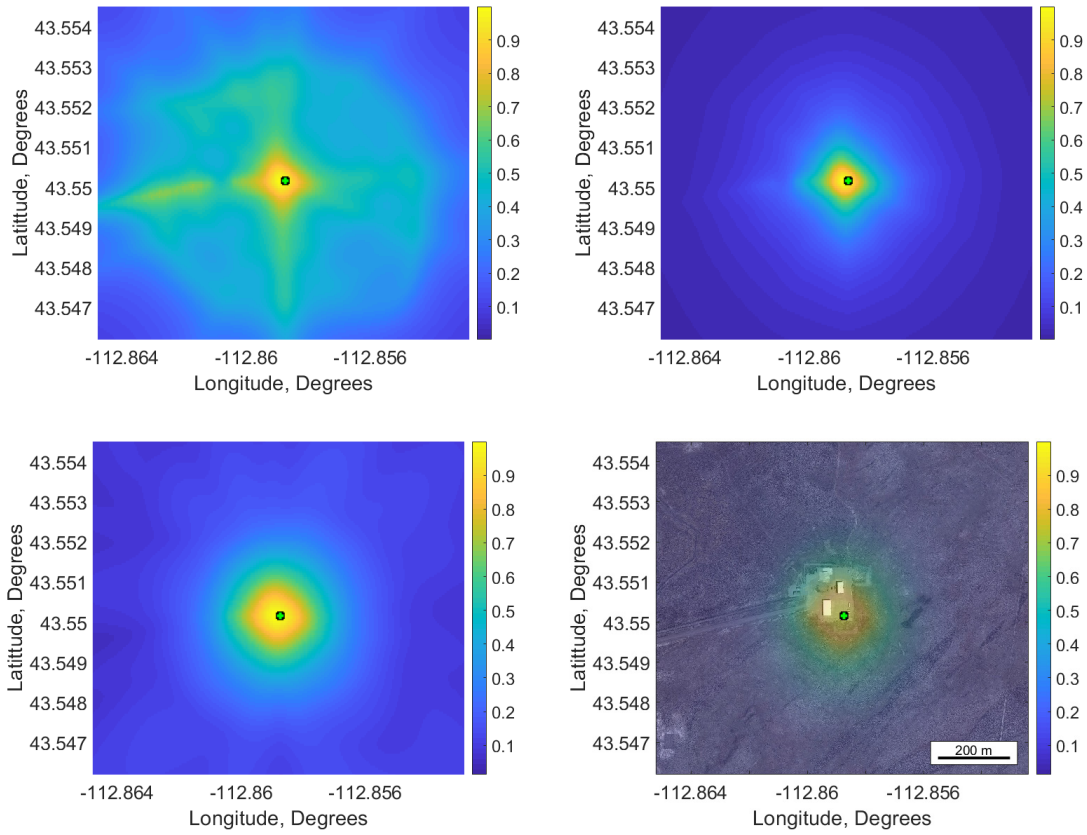

Figure 5.2: (Top left) Detector sensitivity integrated across the entire flight path. Individual helicopter passes from Fig. 5.1 can be clearly seen. (Top right) Non-sensitivity scaled $1/r^2$ reconstruction. (Bottom left) Sensitivity-scaled $1/r^2$ reconstruction. This corresponds to the point-by-point division of the previous two panels. (Bottom right) Sensitivity-scaled $1/r^2$ reconstruction superimposed on Google Maps. The true source location is shown in green across all plots. All plots were normalized by their relative, maximum intensities.

a gamma-ray source for scenarios with many samples directly above and around the source.

Identical analysis was then conducted using imaging information in the form of pointers from centroiding. Estimated source directionality, θ_s, is shown in Fig. 5.3 for portions of the flight. Source directionality was only estimated for measurements with greater than 500 photon counts per second due to limited statistics. During time $\boldsymbol{A}$ the A400 was illuminated preferentially from one side. This measurement corresponds to a clockwise orbit around the gamma-ray source where crystals A_{11}

and A_{21} were preferentially illuminated. During this illumination a clear, horizontal gradient in spatial count rate was observed. The estimated angle to the source, θ_s, was relatively constant at roughly 340° throughout the entire orbit. Contrastingly, measurement ***C*** corresponds to a counter-clockwise orbit around the source where the opposite, horizontal gradient in spatial count rate was observed. Once again, a consistent estimate of source direction, at roughly 190°, was seen during the orbit. In measurement ***B*** the detector passed directly over the gamma-ray source. This measurement corresponds to an equal illumination of all crystal cathodes. As such, no horizontal gradient was observed. However, a rapidly changing vertical gradient was observed where the estimated source angle rotated roughly 180°. This change in directionality corresponds to the detector passing directly over the source.

Centroid-based estimates of the source angle θ_s were plotted on a common spatial grid in Fig. 5.4. Self-consistent source localization is seen for passes directly over the source where pointers flip roughly 180°. Similarly, both orbits around the source show directional estimates pointing towards the true location. Some erroneous pointer behavior was observed for points near the source. This was unsurprising given the detector experienced a substantial change in count gradient over each one second integration; over each integration the detector moved by roughly 20 m. This blurs the reconstructed pointers as the source angle may change over each integration. Furthermore, no option for zero pointer direction was implemented. This complicates regions directly above the source where little gradient was expected. Therefore somewhat random source directions were chosen, due to random fluctuations away from uniformity, at these points directly above the source.

Gamma-ray source localization was attempted using pointers independent of these shortcomings. The summation of pointers on a common grid according to Eq. 5.7 is shown in Fig. 5.5. The estimated source location, the point with minimum, cumulative angular deviation, agrees within 40 meters of the true source location. The

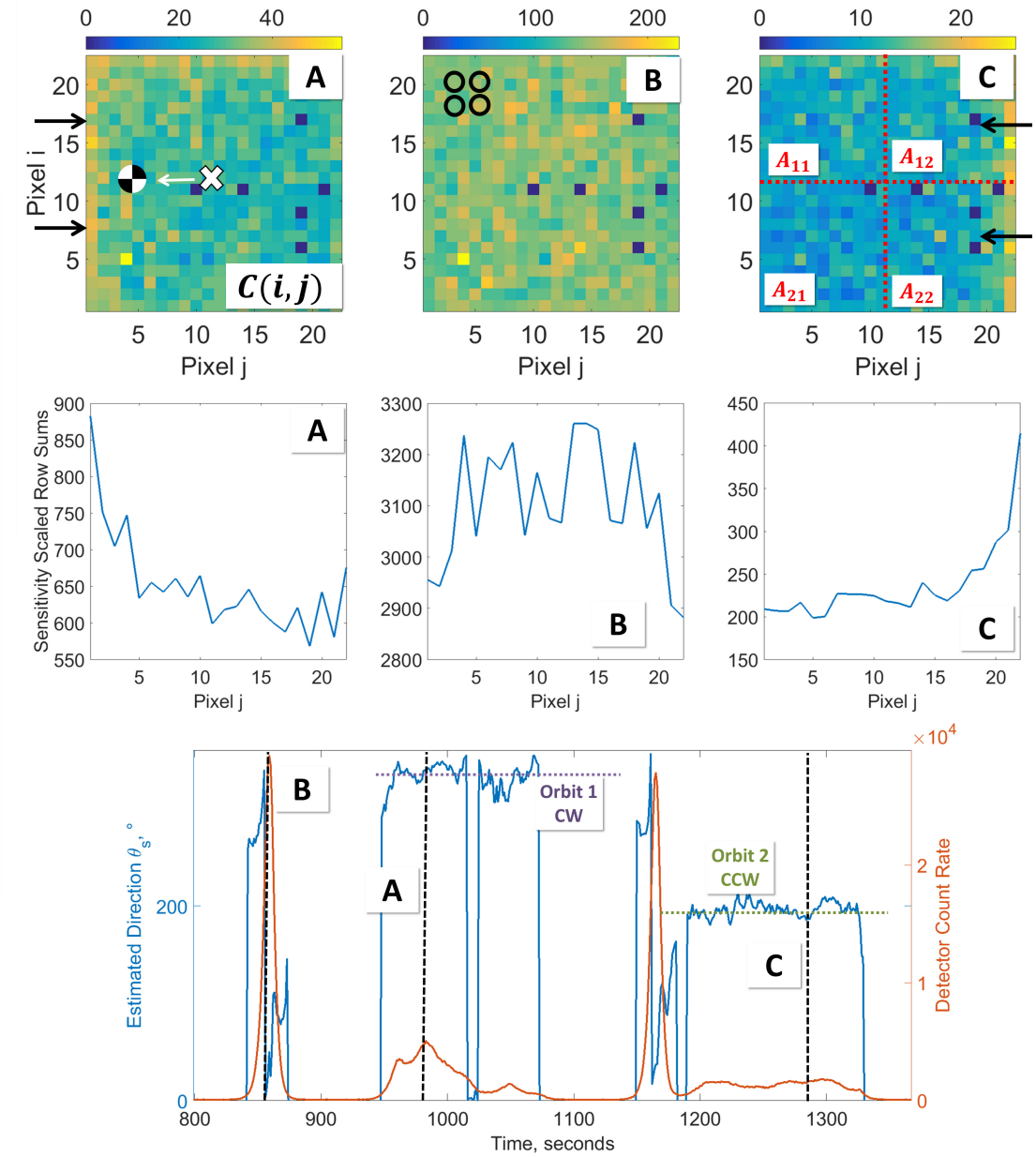

Figure 5.3: (Top left) Sensitivity scaled, pixel-by-pixel A400 gamma-ray count rates for a side illumination. The incident gamma-ray direction is labeled by black arrows. The count-weighted centroid (circle) is displaced from the detector, geometric centroid (white x). Six dead pixels with zero counts are seen. (Top middle) A uniform, cathode-side illumination produces no spatial gradient in pixel-wise count rates. (Top right) An illumination from the opposite direction of ***A***. Individual detector crystals are emphasized by red, dashed lines. (Middle) Column sums to emphasize the horizontal count rate gradients. (Bottom) The displacement of the geometric centroid in the lateral plane was converted to angle θ_s. In ***B*** the helicopter passes directly over the source and the pointer θ_s quickly changes by roughly 180°. In ***A*** and ***C*** the helicopter orbits clockwise and counterclockwise around the source respectively.

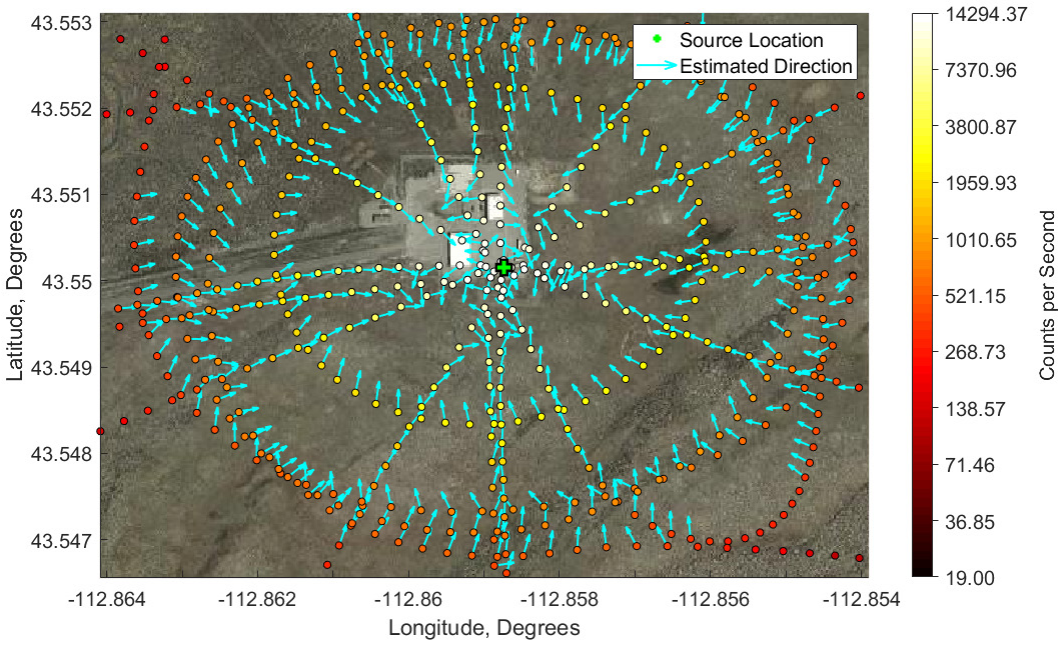

Figure 5.4: Estimated source directions, shown by cyan arrows, computed using the centroid technique for measurements with count rates greater than 500 counts per second.

reconstruction process was then repeated many times using bootstrapped data to quantify statistical uncertainty. The resulting distribution of bootstrapped source locations, shown in Fig. 5.5, illustrates that the measured, 40 m bias is large compared to the statistical spread. The hypothesized root of this disagreement stems from the reconstruction forcing a pointer for all locations, even those directly over the source were the true gradient is small. However, this disagreement is small compared to the size of the measurement space considered. This experimentally demonstrates the successful localization of gamma-ray point source using only imaging information.

Radiation imaging is often combined with optical or spatial information in a process commonly referred to as 'scene data fusion' [104]. H420 optical and Compton images were fused with GPS and A400 spectra. A video showing this scene data fusion for a small subset of the flight can be found here while an individual frame is shown in Fig. 5.6. Compton images were generated using 250-620 keV events. This broad energy window, from the highest energy ^{192}Ir emission to the low-energy

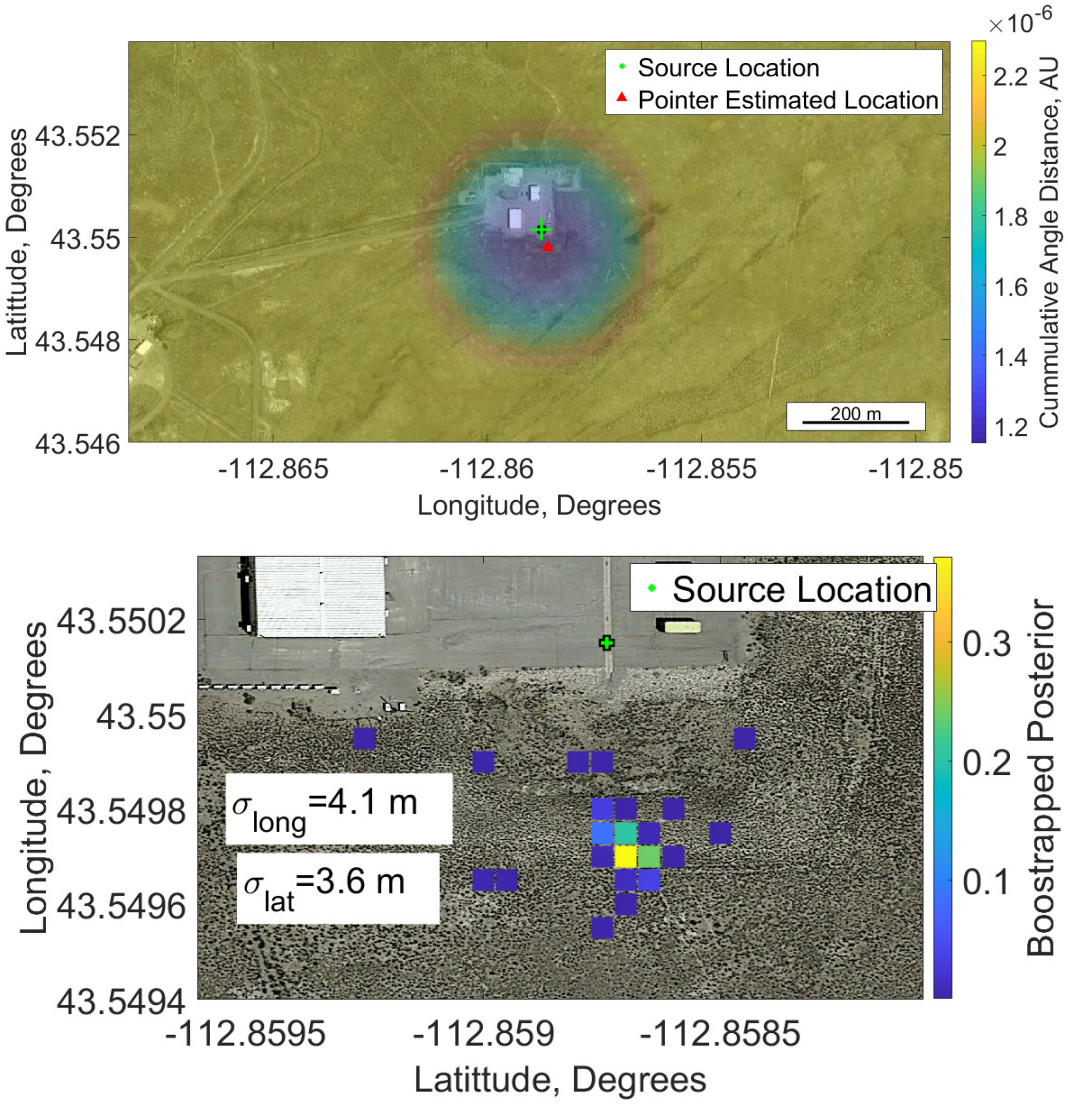

Figure 5.5: (Top) Cumulative pointer distance $D(x, y)$ for all measurement points. The location with the minimum cumulative distance was chosen as the source location. (Bottom) Bootstrapped estimates of source location using the pointer technique. A video demonstrating the image reconstruction process is provided here.

limit of Compton imaging, was chosen as the spectrum contained few photopeak events. Although statistically limited, Compton reconstructions clearly show that the gamma-ray source falls inside the compound of buildings. Coded aperture imaging, although relatively efficient given the preponderance of low-energy flux, could not be utilized as the measurement scene changed more rapidly than the time required for mask-antimask analyses.

One second A400 spectra were summed across the entire flight at 400 ft and shown in Fig. 5.7. ^{192}Ir photopeak triplets around 300 and 600 keV are clearly seen in addition to the strong 468 keV emission. Clear detection of source photopeaks is important in select emergency response applications. For example, photopeak ratios in fallout can encode information on nuclear weapon type [105].

5.3.2 Truncated Flight Path

Previous analyses were conducted using the entire flight path which contained several passes directly over the source. Access to airspace above a source may be limited in practical measurements. Additionally, when first looking for a source, a wide search pattern is flown consisting of parallel lines. The distance between subsequent lines, known as the line spacing, can be quite large. For example, line spacing can be as large as 0.5 miles, or roughly 800 m, at a detector altitude of 500 ft for Aerial Measuring Systems in the Department of Energy [106]. With such large line spacing it is conceivable that no measurements are collected directly over, or nearby, a strong gamma-ray source. This specific measurement scenario, where there are no measurements directly above or near a gamma-ray source, was investigated by truncating the 400 ft flight path.

The complete measurement, with many passes directly over the source, was truncated into smaller datasets to investigate source localization techniques under non-ideal conditions such as limited parallax and lack of sample points near the source

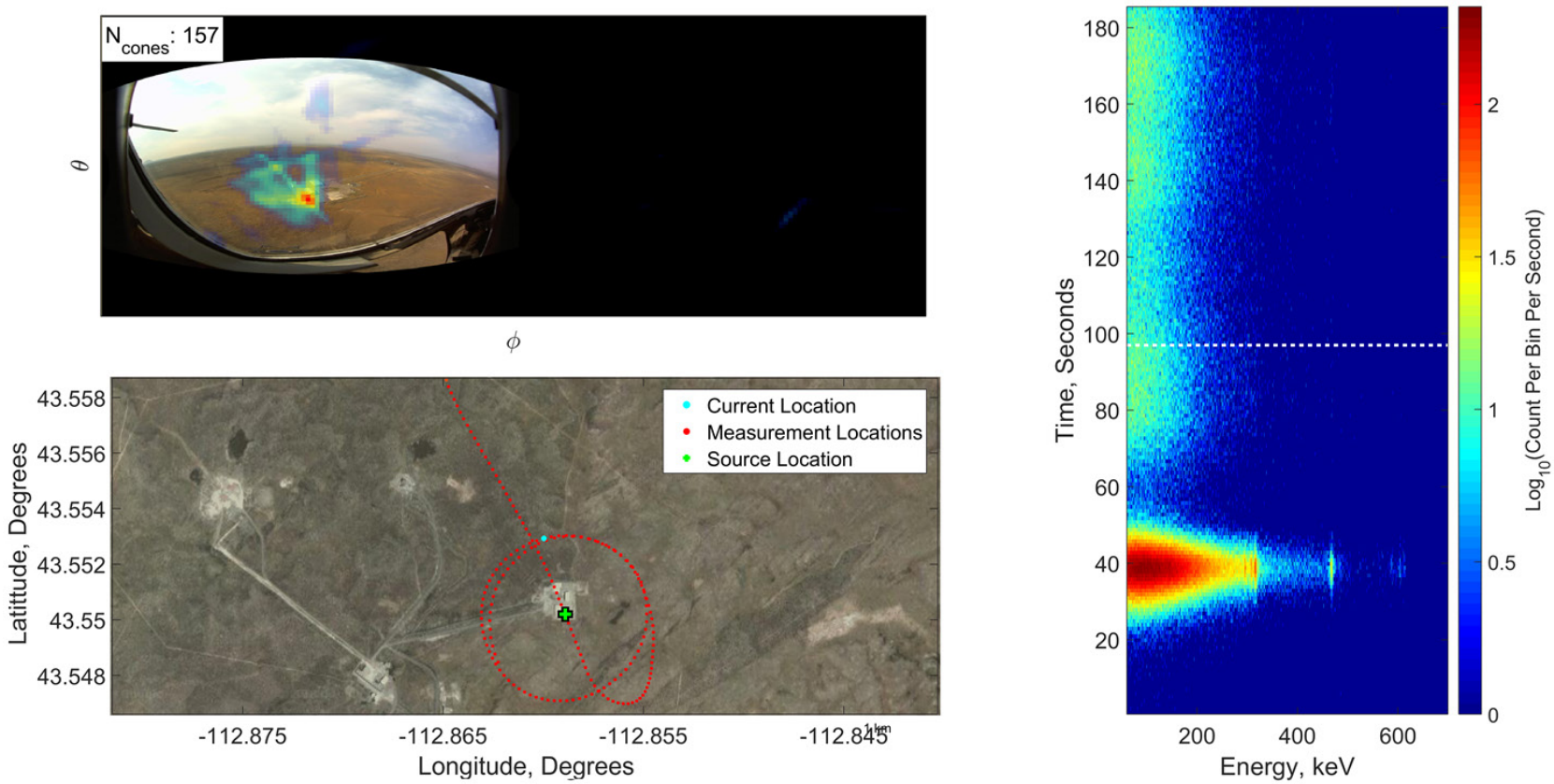

Figure 5.6: (Top) Compton reconstruction backprojected onto a fisheye optical image. Pixels falling below half the maximum intensity in the Compton image were omitted for clarity. Only one fisheye camera was used, limiting the optical FOV to 2π. (Bottom) Helicopter GPS at one second intervals. The current location and true source location are shown by a cyan circle and green cross respectively. (Right) Waterfall plot of A400 counts as a function of time. The white dashed line corresponds to the current, instantaneous spectrum.

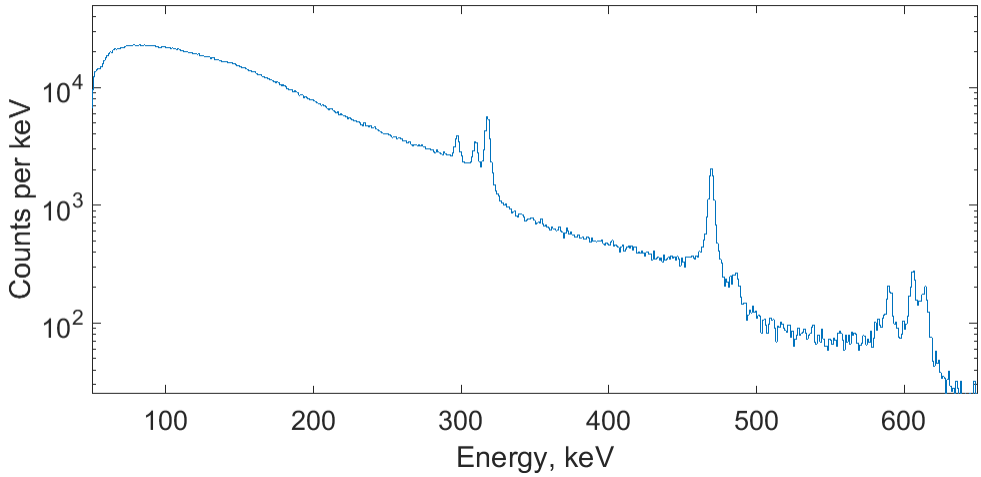

Figure 5.7: A400 gamma-ray spectra integrated across the entire 400 ft flight path. The prominent 468 keV emission alongside triplets at roughly 300 and 600 keV from ^{192}Ir are seen.

location. The impact of these two complications were investigated using both $1/r^2$-based localization and imaging.

Two truncated datasets were considered. The first dataset consisted only of points east of the source, beyond longitude -112.855°. The second dataset added points north of the source, such that points north of 43.551° or east of -112.855° were considered. The two truncated datasets were reconstructed using $1/r^2$ information in a manner identical to Fig. 5.2. Gamma-ray reconstructions using back-projected $1/r^2$ data are shown in Fig. 5.8. For the smallest dataset, reconstructed intensities, $I(x, y)$, were largest for locations east of the source. These points correspond to locations with the highest, measured count rates. Reconstructed intensities for points further east, beyond this high count region, are relatively low. Points west of this high intensity region are more intense than those further east. However, the intensities are relatively small compared to those directly under the flight path. Similar localization behavior was seen in the larger dataset that added points north of the source. Once again, simple-backprojection estimates were largest for spatial points near the high count rate samples along the flight path. As such, the estimated source location was

significantly biased for these measurements without samples above the true source location.

Similar behavior was observed for both simple-backprojection and maximum-likelihood-based reconstructions by *Hellfeld et al.* using a man-portable, mobile detector [107]. $1/r^2$-based reconstructions were seen to converge along the path of the mobile detector, and not the true source positions, in some large, 3-D space without samples near the source. When a sparseness prior was added to the maximum-likelihood problem, allowing for up to a few point sources, [107] achieved both good source localization and strength estimation. This occurs as there are many more, non-sparse source distributions along the path of travel that explain the observed data than the true, sparse solution. As such, it is unsurprising that the reconstruction estimates some non-sparse solution given limited measurement statistics, model mismatch and noise. This suggests that unconstrained, $1/r^2$-based source localization struggles in scenarios where no samples are collected near true source locations.

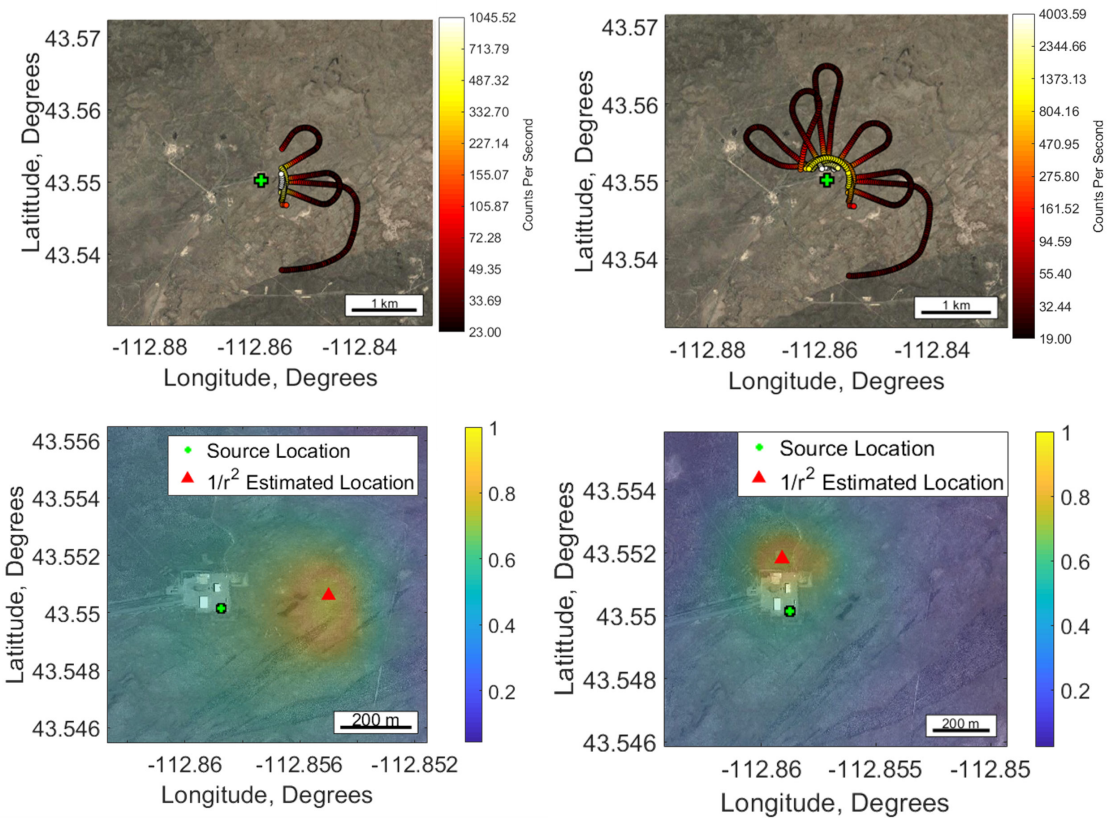

Figure 5.8: (Top left) The complete flight path was truncated, only including points east of longitude -112.855°, to investigate the influence of limited measurement sampling and parallax. (Top right) Points to the north of the source, with latitudes north of 43.551°, were added to the measurement. (Bottom left) Sensitivity normalized, simple back-projection from measurements using points east of -112.855°. The response is largest near points with the highest count rates. (Bottom right) Sensitivity normalized, simple back-projection after adding points north of 43.551°. Once again, the reconstruction is largest for points near the highest count rates. Note neither reconstruction accurately localizes the true source position.

The effects from limited parallax and sampling in truncated measurements using imaging are shown in Fig. 5.9. First, analyses were conducted only using points east of the source. Only samples in a narrow, 50 m wide, longitudinal band nearest the source had count rates exceeding 500 counts per second. Directionality estimates were only generated for these points, as discussed before, and used to localize the source. The truncated measurement was bootstrapped and repeatedly reconstructed to es-

timate statistical uncertainties. The resulting distribution contains the true source location and had relatively large longitudinal uncertainty. This occurs as samples were taken along a small, longitudinal band. As such, all estimated pointers were similar in direction. This lack of system parallax, where the detector sees the source from roughly the same direction at all sample points, could be resolved in several ways. First, measurements could be taken along a larger, latitudinal slice. Second, samples could be taken closer to the source. Both options function similarly, adding samples with substantially different estimates of source direction, to improve longitudinal estimates. Similarly, adding samples north of the source substantially increased parallax along the longitudinal direction. When using these points, uncertainty in longitude was decreased to a level comparable to that of latitude. Overall, the centroid-based, gamma-ray source localization technique successfully localized sources in measurements without samples directly above the source or a sparsity prior. Successful imaging results are in stark contrast to the performance seen using only $1/r^2$ information. This suggests, preliminarily, that imaging information increases source localization robustness in scenarios without samples directly above the source and sparsity priors.

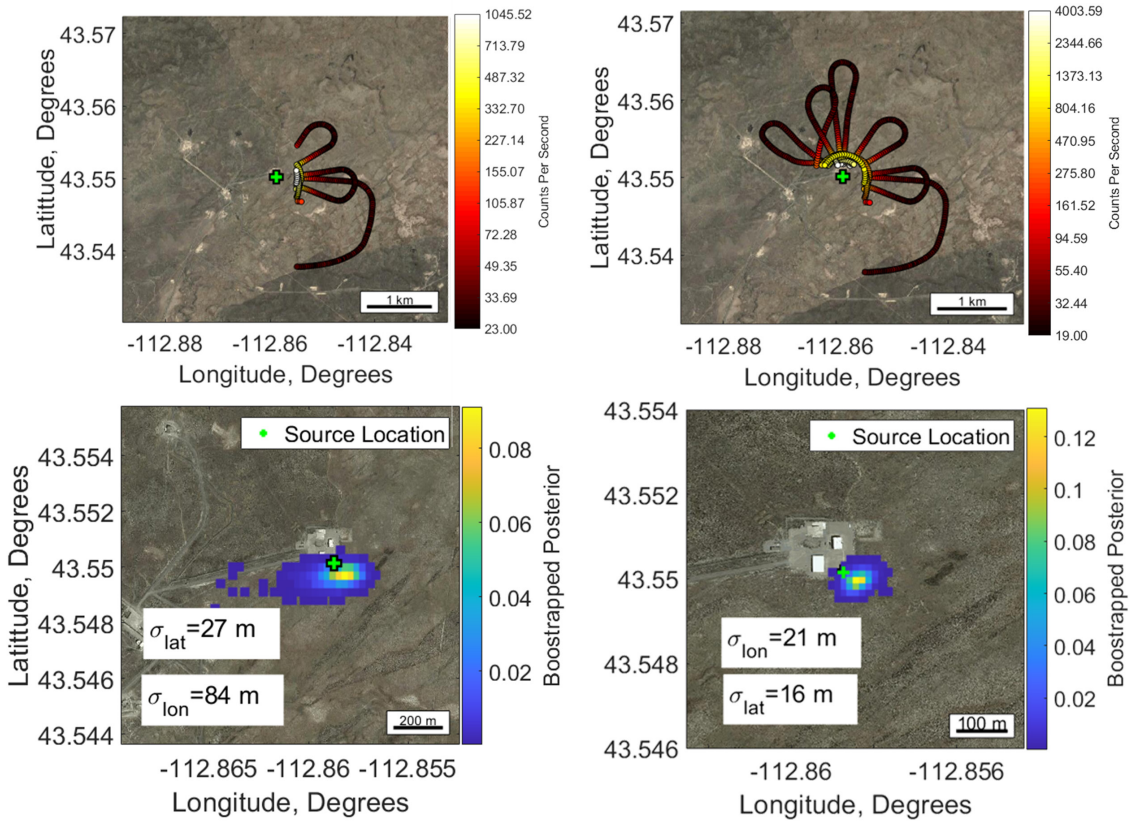

Figure 5.9: (Top left) The complete flight path was truncated, only including points east of longitude -112.855°, to investigate the influence of limited parallax and sampling. (Top right) Points to the north of the source, with latitudes larger than 43.551°, were added to the measurement. (Bottom left) Bootstrapped estimates of source locations, using only points east of the source, showing substantial ambiguity in longitude. A video demonstrating the image reconstruction process is provided here. (Bottom right) Adding parallax from samples north of the source significantly reduced longitudinal uncertainty. Both bootstrapped distributions contain the source location. A video demonstrating the image reconstruction process is provided here.

5.4 Conclusion

Commercial H3D A400 and H420 CdZnTe systems successfully operated on a helicopter under heavy vibrational load. Detector count rates were seen to rise as the systems were flown towards a strong, gamma-ray source. Simple-backprojection of $1/r^2$ count rates was used to accurately localize the source in scenarios with sam-

ples points directly above the source. Poor $1/r^2$ localization performance was seen in truncated datasets without sample points directly above the source. Reconstructed backprojection distributions closely followed the detector path. This observed behavior was similar to that seen in [107]. Naïve, centroid-based point source localization was implemented. The bootstrapped distribution of centroid-based location estimates was slightly biased when using the complete dataset. However, this bias was small when considering both the simple imaging technique and dead-reckoning for helicopter pose. Contrastingly, the centroid-based technique robustly localized the gamma-ray source in truncated measurements without samples near the source. Parallax-limited, directional uncertainty in bootstrapped distributions was clearly seen. Adding measurement points that viewed the source from a different, nearly orthogonal angle, greatly reduced localization uncertainly along the direction previously limited by parallax. In general, imaging-based localization appear robust in measurements without samples directly above the source or a sparsity prior.

The weights of commercial CdZnTe systems, 5.0 and 7.8 lbs for the A400 and H420, are well below payload limits on commercial drones [108]. CdZnTe detector systems have matured sufficiently that commercial, off-the-shelf H3D systems can be easily mounted on drones. Computer-vision-based navigation techniques, such as open source Google Cartographer [109], can be easily implemented to get relative detector pose. Given relative detector location and pose, source distributions can be reconstructed in a common space using algorithms like those described in [55,110] and illustrated in Fig. 5.10. Furthermore, imaging performance can be improved using mechanical gimbals designed to steady high-resolution, optical cameras. Gimbal-based steadying is particularly important for radiation imaging techniques that require substantial dwells such as coded aperture. With increased platform stability improved coded aperture techniques, such as mask anti-mask, become feasible. Source localization measurements using drone-borne detectors would reduce operational costs and

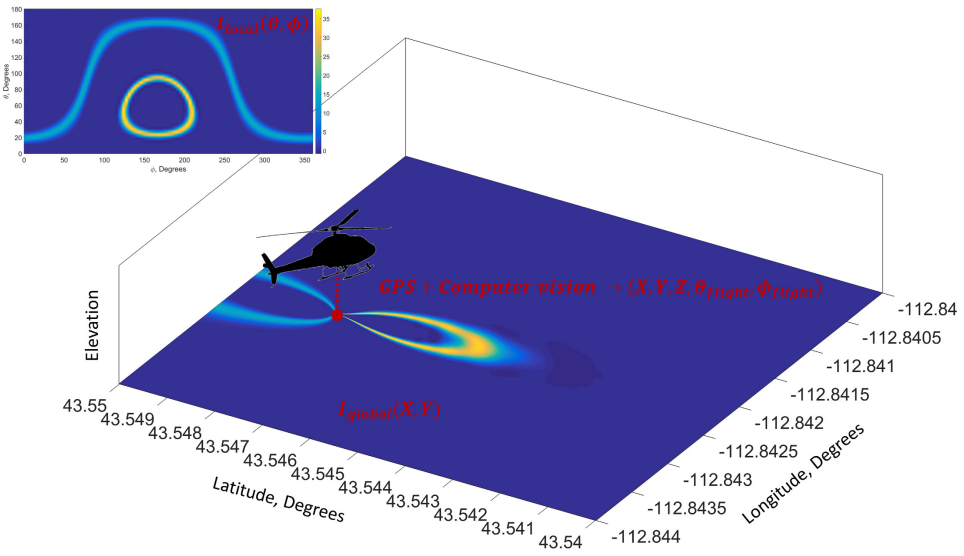

Figure 5.10: Stationary gamma-ray measurements are typically reconstructed in local, angular space ($I_{local}(\theta, \phi)$) around a detector as shown in the inset Compton image. Data can also be reconstructed on some common, global spatial domain ($I_{global}(X, Y)$) using position and pose from sources such as GPS or computer vision. Identical data is reconstructed in each space where $(\theta, \phi) = (90, 90)^\circ$ corresponds to the direction beneath the helicopter.

completely eliminate operator dose in emergency response scenarios.

CHAPTER VI

Fast Neutron Source Localization

6.1 CdZnTe Fast Neutron Detection

Fast neutron recoil detectors are typically hydrogenous as the maximum, fractional energy loss for a single neutron scatter decreases with increasing atomic mass, A, as shown in Eq. 2.2. CdZnTe is primarily composed of cadmium and tellurium, with A_{eff} of 112.4 and 127.6 respectively. In tellurium, this corresponds to a 3%, maximum energy loss for a single, elastic neutron scatter. For 2.5 MeV neutrons, generated by deuterium-deuterium (DD) fusion, 3% propagates to a 75 keV energy deposition. However, not all the kinetic energy imparted to the scattered nucleus is recorded as electron-hole pairs. Nuclei are less efficient at generating electron-hole pairs than electrons of similar energy [111]. Reported values for the quenching factor, the ratio of electron-hole pairs generated by a recoil nucleus and electron of the same energy, is about 0.25. This brings the maximum, recorded energy of a backscattered, DD neutron to about 20 keVee (keV electron-equivalent). The recent development of low-noise, digital ASICs, spearheaded by Dr. Zhu, has pushed CdZnTe low-energy thresholds to around 5 keV [40,112]. Fast-neutrons from ^{252}Cf, PuBe and DD neutron sources have been detected previously using a low-noise CdZnTe system [15]. Fast neutron sources can be coarsely localized using the distribution of counts across a position-sensitive array. 1-D neutron source localization is discussed following the

work presented in *Goodman et al.* [113].

6.2 Fast Neutron Source Localization

Fast neutrons sources can be localized using a variety of techniques. Scatter camera systems require two, recorded neutron interactions. Scatter cameras record both the 3-D position and energy deposited at each interaction, alongside the transit time between them. Using scattering kinematics, this information is sufficient to localize the incident neutron to the surface of a cone in a manner similar to Compton imaging [114, 115]. Fast neutron coded aperture is another common localization modality that uses a hydrogenous mask to encode source directionality [116]. Other systems simply measure the attenuation of interactions across multiple detectors or a voxelized volume to coarsely estimate source directionally [62]. Coarse, 1-D source localization was demonstrated by recording the attenuation of DD neutrons across a four crystal CdZnTe array.

6.2.1 Attenuation Model and Maximum-Likelihood

2.5 MeV neutrons interact via inelastic and elastic scattering with CdZnTe crystals. These crystals modulate the incident flux with a macroscopic cross section $\Sigma_T \simeq 0.15$ cm^{-1}. Due to the complex nature of neutron scatter kinematics, a first order model was implemented assuming any interaction removes neutrons from the system, preventing subsequent signals. Notably this approximation overestimates detector attenuation. Using this model, the likelihood p an interaction in detector pixel n at position $\bar{r}_n$ was emitted from azimuthal direction ϕ is

$$p_n(\phi) = e^{-x(\bar{r}_n,\phi)\Sigma_T} \tag{6.1}$$

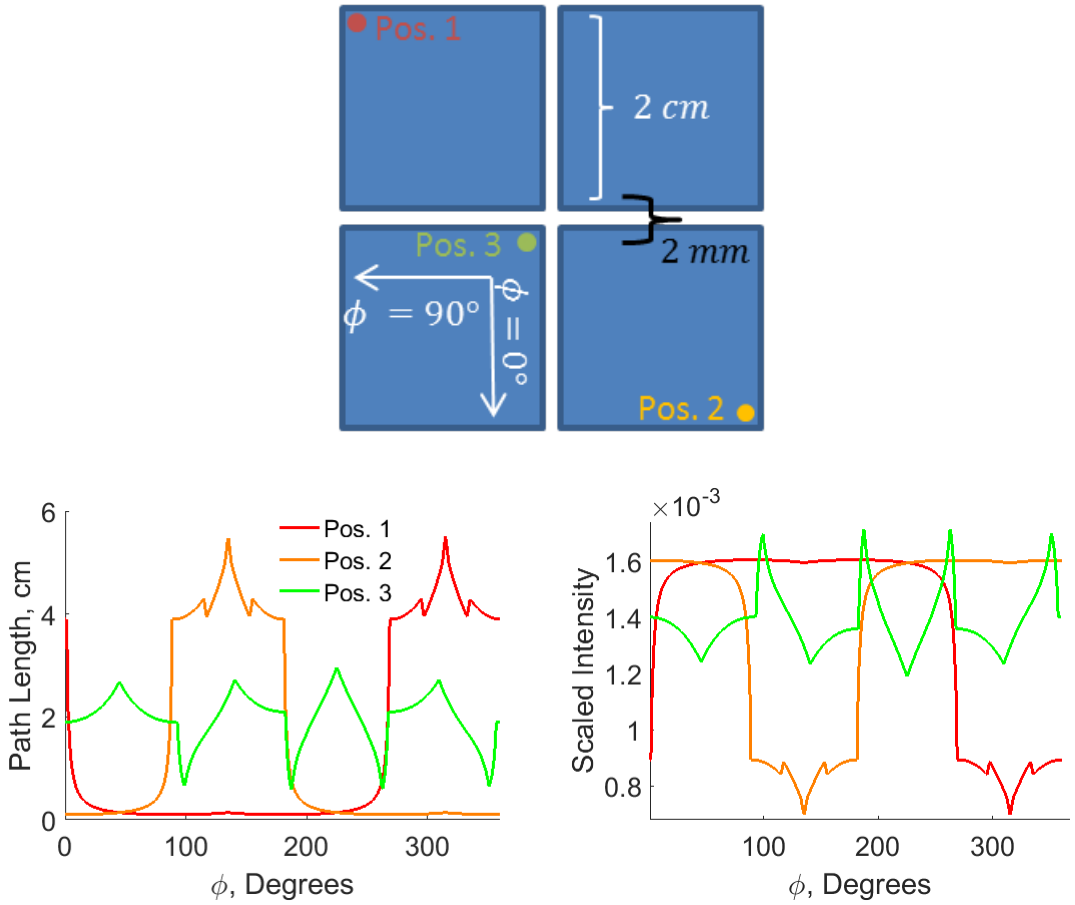

Figure 6.1: (Top) Three hypothetical fast neutron scatters recorded in a four crystal CdZnTe system. Bottom) Path lengths x^d (bottom left) and relative incident neutron direction probabilities (bottom right) for each event calculated through the first order attenuation model. Path length fluctuations in position three are caused by detector gaps.

where $x(\bar{r}_n, \phi)$ is the ray traced path length through all CdZnTe from pixel location $\bar{r}_n$ in direction ϕ.s

Sample distributions, $p(\phi)$, for three detector pixels in a four crystal array are shown in Fig. 6.1. Ray traced responses from all detector pixels were then used to predict expected detector pixel counts

$$\boldsymbol{E}[\boldsymbol{g}|\phi_j] = \boldsymbol{\lambda}_j \tag{6.2}$$

for given source direction ϕ_j. Note expectation means from all directions are scaled

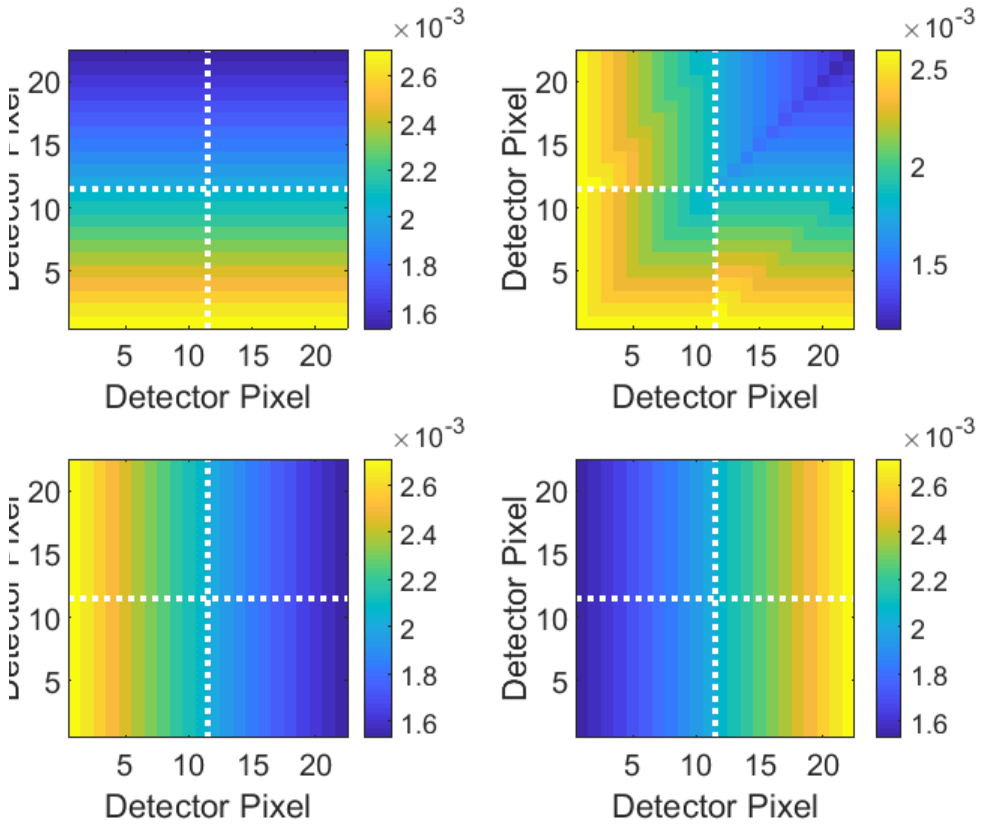

Figure 6.2: From top left to bottom right: Expected pixel counts $\boldsymbol{\lambda}$ for source directions $\phi = 0, 45, 90, 270°$ given uniform detector sensitivity. Note the clear attenuation of neutron counts across the detector volume. Individual detectors, with 11 x 11 anodes, are demarcated by white, dashed lines.

to measured counts. Example expectations are shown in Fig. 6.2. Model mismatch stemming from the first order attenuation model was investigated via simulation in Geant4 as shown in Fig. 6.3 but chosen as acceptable [117]. These expectations were then sensitivity corrected via a cathode flood, where all detector pixels were evenly illuminated, as shown in Fig. 6.4. Using these expectations a maximum-likelihood estimator, assuming a single source direction, was implemented. The likelihood a source in position ϕ_j caused the measurement of detector pixel counts $\boldsymbol{g}$ given expectation $\boldsymbol{\lambda}_j$ is

$$L(\boldsymbol{g}|\boldsymbol{\lambda}_j) = \prod_{n=1}^{N} \frac{\lambda_n^{g_n} e^{-\lambda_n}}{g_n!} \tag{6.3}$$

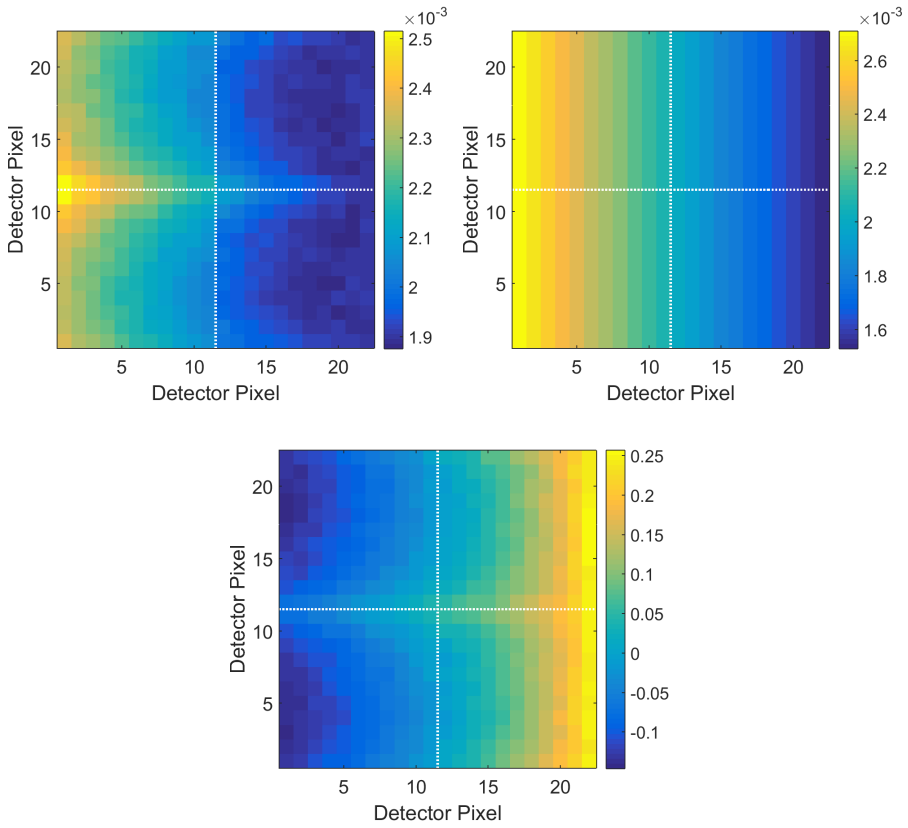

Figure 6.3: $\boldsymbol{\lambda}$ for $\phi = 90°$ simulated using Geant4 (left) and the first order attenuation model (right) with fractional differences (bottom). Systematic overestimation of attenuation is seen across the detectors yielding a maximum 25% bias.

where λ_n is the expected number of counts in detector pixel n for given source direction j, g_n is recorded counts in detector pixel n and there are N total active detector pixels. For computational ease, the natural logarithm was taken for the log-likelihood

$$l(\boldsymbol{g}|\boldsymbol{\lambda}_j) = \sum_{n=1}^{N} g_n \ln(\lambda_n) - \lambda_n \tag{6.4}$$

where the maximum across J possible, discrete source directions

$$\hat{\phi}_{est} = \underset{j\in[1,2,\ldots,J]}{\operatorname{argmax}} \{l(\boldsymbol{g}|\boldsymbol{\lambda_j})\} \tag{6.5}$$

was used as a scalar estimate of source direction ϕ with the estimator error ϵ_ϕ defined as

$$\epsilon_\phi = |\hat{\phi}_{est} - \phi_{true}|. \tag{6.6}$$

Elastic neutron scatter cross sections increase for fission energies, roughly 1 MeV, and decrease towards 5 MeV. This suggests that the count rate gradients used in this work for localization would be enhanced for fission neutrons and degraded for harder sources, such as PuBe.

Detector leakage current was found to be slightly time dependent. This change as a function of time could affect observed pixel trigger rates. Sensitivity scaled pixel counts were binned for localization measurements and outliers were clearly identified as shown in Fig. 6.4. After identification, the noisy pixel was removed from reconstructions. The pixel with increased noise triggering was shared between measurements and occurred on a detector corner. The hypothesized source of the temporal noise behavior stems from humidity and temperature fluctuations modifying leakage to detector guard rings.

Fast neutron localization using attenuation in current pixelated CdZnTe systems is limited to 1-D due to the lack of depth information for interactions. For gamma-

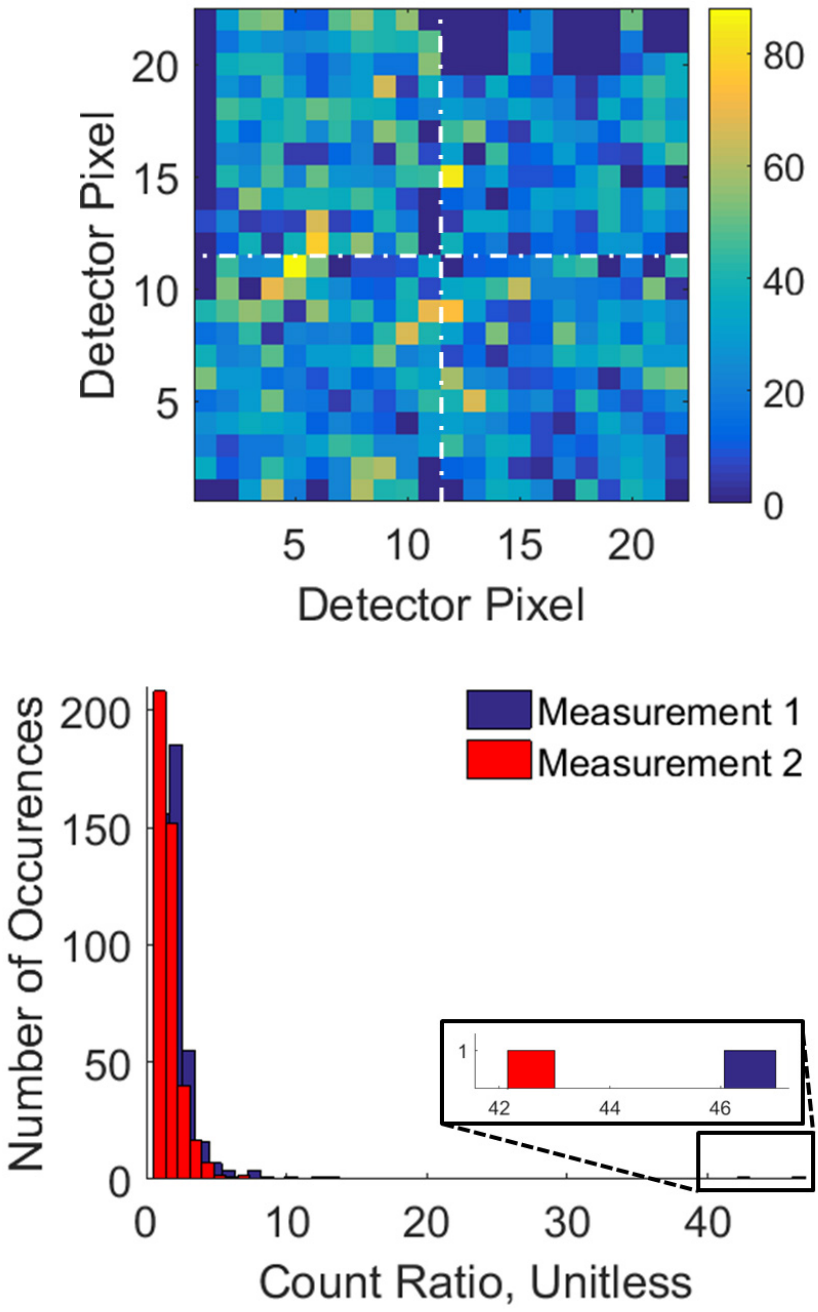

Figure 6.4: (Top) Pixel sensitivity s_n measured using a cathode illumination where each pixel was exposed to a similar fast neutron fluence. Individual detectors are demarcated by white, dashed lines. Pixels with zero counts were disabled due to poor noise performance: individual pixel thresholds can only be slightly changed from a global detector threshold. Note Poisson uncertainties in pixel sensitivities are large. (Bottom) Sensitivity scaled pixel counts were histogrammed for all 484 detector pixels. Clear outliers, box in black with vastly increased sensitivity scaled counts compared to all other pixels, are seen.

ray interactions, depth is computed using the cathode to anode ratio [39]. However, cathode electronic noise degrades depth resolution for small, 5 keVee neutron scatter pulses. This depth uncertainty blurs count rate gradients, making source localization using attenuation along depth difficult.

6.2.2 DD Generator Measurements

A Thermo-Fisher MP320 DD neutron generator was used to illuminate the Orion system with roughly mono-energetic 2.45 MeV neutrons. The DD generator ran at 80 kV with a tube current of 60 μA. Nominal neutron flux was estimated as 10^6 n/s into 4π. Significant levels of bremsstrahlung radiation were generated by the movement of deuterium ions and was mitigated by covering the generator with thin layers of lead. Before neutron measurements a ^{133}Ba source was placed on the generator to confirm that its 80 keV emission was adequately shielded. The generator and detector system were elevated to reduce the amount of environmental capture gamma-rays and room scattered neutrons. First a sensitivity measurement was taken by illuminating the cathode side of all crystals uniformly for 45 minutes. Then the Orion prototype system was placed 50 cm away from the MP320 target plane with detector sides, not cathodes or anodes, facing towards to the generator as shown in Fig. 6.5. Each side irradiation was conducted for 45 minutes with the Orion prototype being rotated laterally between measurements.

6.2.3 Results

An overnight background spectrum, with no MP320 generator, and spectrum while the generator was running were collected. A background subtracted generator spectrum was then calculated as shown in Fig. 6.6. A clear peak in the 5-15 keV region is seen from elastic scatter. This peak is formed by an upwards trend towards lower energies convolved with pixel-to-pixel thresholding effects. Prominent inelastic

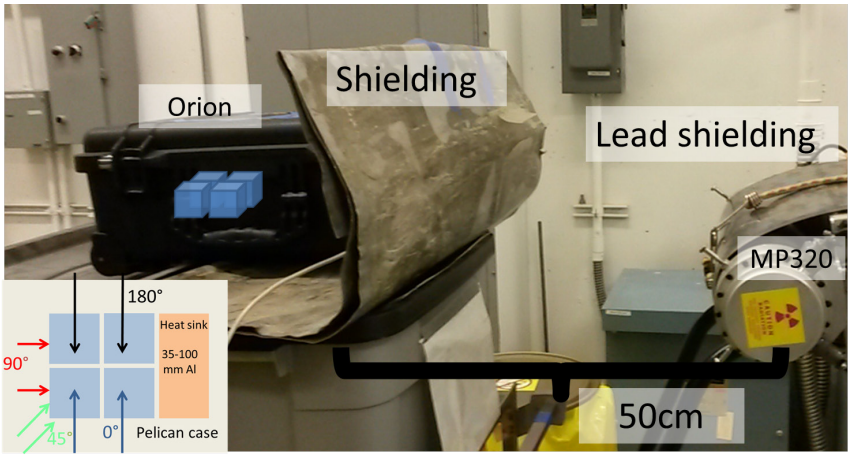

Figure 6.5: Relative geometry between the MP320 generator and the Orion prototype with the relative position of crystals shown in blue. Fast neutron irradiation directions of Orion used in subsequent measurements are inset.

gamma-ray lines from cadmium and tellurium are seen. Furthermore, the inelastic 558 and 651 keV lines are enhanced from the capture of environmentally thermalized source neutrons on ^{113}Cd.

The log-likelihoods for each illumination angle shown inset in Fig. 6.5 are tabulated in Fig. 6.7 over 0.5° bins. An irradiation from 270° was taken but omitted due to the attenuation from the aluminum heatsink. Discontinuities occurring at several angles across reconstructions stem from clusters of pixels disabled due to poor noise performance being excluded from the likelihood. Directional estimates $\hat{\phi}_{est}$ and associated errors ϵ_{ϕ} were tabulated in Table 6.1. The absolute error of the estimator was small, between 2.5 and 14.0°, even given large uncertainties in pixel sensitivities from Poisson error and use of a naïve attenuation model.

6.3 Conclusion

The reduced low-energy thresholds of digitized, 3-D position-sensitive CdZnTe detectors has enabled detection of fast neutron via atomic recoils. Coarse, 1-D DD neutron generator localization was experimentally demonstrated using a single scatter

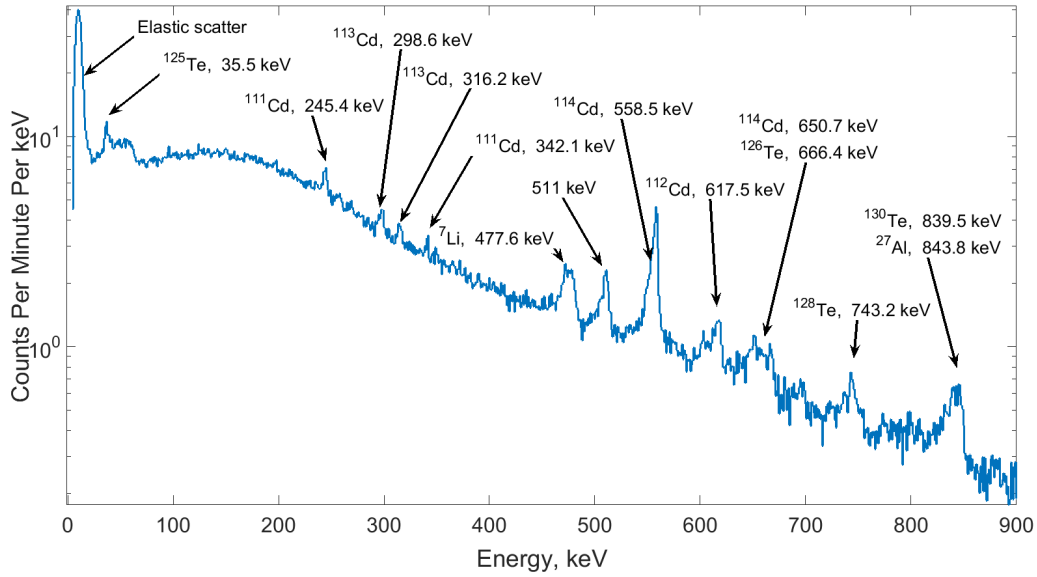

Figure 6.6: Background subtracted MP320 spectrum summed across all measurements. Several prominent environmental and detector inelastic and capture gamma rays are seen.

Table 6.1: True and estimated source locations using a maximum-likelihood estimator and first order attenuation model.

ϕ_{true}, °	$\hat{\phi}_{est}$, °	$\lvert\hat{\phi}_{est}-\phi_{true}\rvert$, °
0.0	352.5	7.5
45.0	59.0	14.0
90.0	87.5	2.5
180.0	172.5	7.5

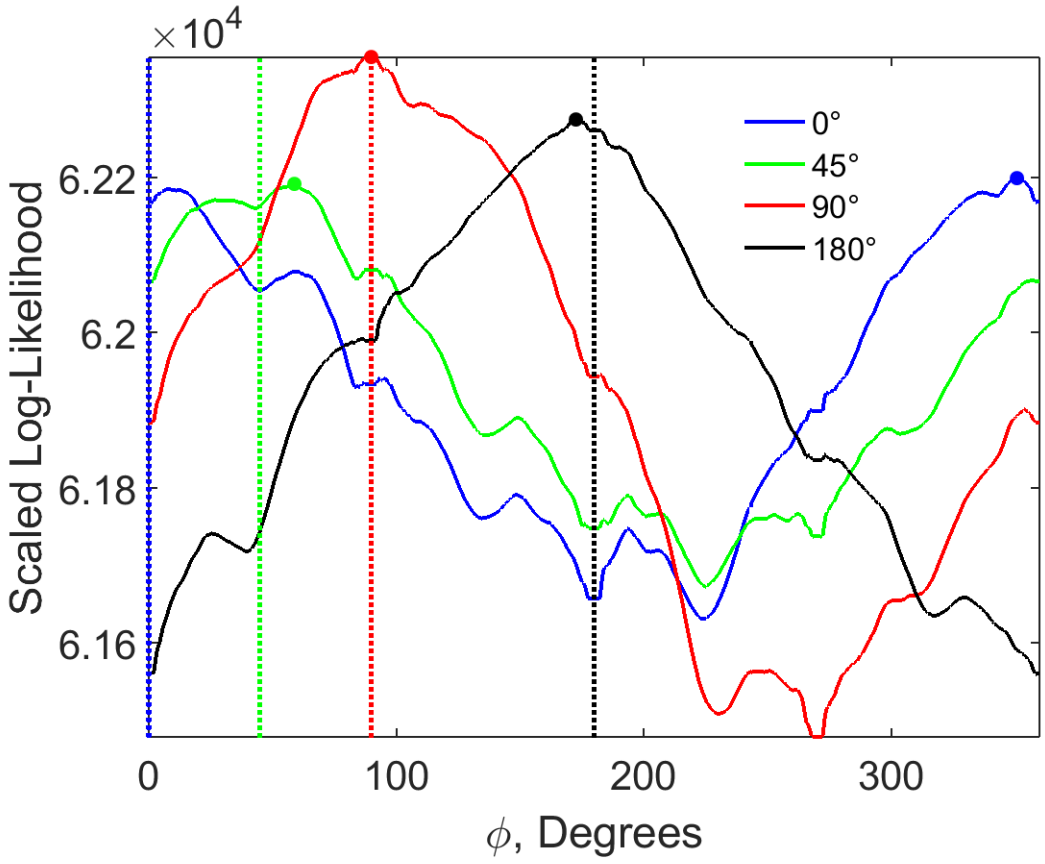

Figure 6.7: Log-likelihoods reconstructed using all events in the 5-20 keV window for each illumination angle. Log-likelihoods were scaled to have the same mean for ease of plotting. Estimated locations are marked with equivalently colored points. True source locations are marked with equivalently colored, dotted lines.

model and maximum-likelihood based algorithm with mean error of less than 10°.

The efficiency of a four crystal CdZnTe system with 5 keVee low-energy threshold is very low, around 8%, to Watt spectrum fast neutrons [15]. The efficiency of neutron detection using 3-D CdZnTe will only improve as system active volumes increase. Large systems with over 300 cm^3 active volume, more than 1.8 kg of CdZnTe, have been fielded for medical applications [118]. Design of the next generation of digital ASICs, with lower, low-energy thresholds, is nearing completion. Further reduction of detector low-energy thresholds will improve CdZnTe fast neutron sensitivity. Even with these improvements CdZnTe-based fast neutron detection and localization systems will never be competitive with traditional fast neutron detectors using organic scintillators or moderated ^{3}He. However, digital CdZnTe systems offer fast neutron detection and localization capabilities, albeit poor, 'for free' when deployed for high-performance, photon spectroscopy. This provides users additional information on measurements of heavily shielded black-boxes where gamma-ray signals are limited.

CHAPTER VII

Neutron-Induced Gamma-Ray Imaging

Radioactive sources are often shielded by compound materials. Compound materials, materials comprised of multiple elements, are difficult to probe using gamma-ray-based shielding detection algorithms. These algorithms, discussed in Chapter III, are primarily sensitive to 'effective' atomic number and areal thickness. As such, the combination of high-and-low-Z shielding appears similar to that of a single, moderate-Z one. Furthermore, gamma-ray based shielding detection algorithms are completely insensitive to isotopics, as gamma rays only interact with electrons. Therefore realistic scenarios containing compound shields, or cases where isotopic information is desired, require a different approach.

Some radioactive objects, such as SNMs, emit both fast neutrons and gamma rays. In combined neutron and gamma-ray fields, such as those around plutonium, characteristic neutron-induced gamma rays from neutron interactions in shielding offer a complimentary, isotope-specific signal of shielding composition [119, 120] as discussed in Chapter I. These characteristic neutron-induced gamma rays can be detected and imaged using CdZnTe detectors in a manner identical to those produced by traditional radioisotopes to provide spatially-resolved estimates of shielding isotopics around SNMs. This chapter closely follows the discussion presented in *Goodman et. al* [121] and demonstrates the novel, spatially-resolved characterization of shielding

isotopics in polyethylene and polyvinyl chloride plastic targets, excited via a neutron source, using an array of pixelated, CdZnTe detectors and Compton imaging.

7.1 Modified High-Energy Event Processing

Characteristic, neutron-induced gamma rays can be energetic with energies exceeding several MeV. These photons can be detected using CdZnTe detectors and spatially localized via Compton imaging. High-energy, gamma-ray interactions in CdZnTe produce large charge clouds with sizes comparable to that of the anode pixel pitch [122]. Large charge clouds are collected across multiple, neighboring anode pixels, triggering them, and generating what is known as a charge sharing event. The true gamma-ray interaction position must therefore be estimated using the signal from some array of spatially-contiguous, anode pixels. The interaction location is estimated using the energy-weighted centroid of the cluster of anode pixels. The energy deposition of the interaction is then naïvely estimated via summing the energies of each pixel. Combined, these two rules were used to cluster groups of triggered, side-neighbor pixels into individual, interaction sites. These high-energy, gamma-ray interaction sites were then used in Compton imaging to estimate incident source direction.

High-energy, Compton imaging deals with slightly different detector physics. The pair production cross section of high-energy photons is non-negligible in CdZnTe. Photons that undergo pair-production as their first interaction are not imagable. First-interaction, pair production events can fall into photopeaks if subsequent, 511 keV annihilation photons are absorbed. Therefore, first-interaction, pair production events should be discriminated from first-interaction, Compton scatter events to maximize image quality. Several techniques exist to remove pair production events recorded using position-sensitive readout. A simple and effective algorithm simply discards events where any number of interactions sum to 511 keV within some un-

certainty [123]. However for simplicity, this work does not attempt to remove any pair production events. These unwanted, pair production events were not expected to significantly degrade image quality in the sparse scenes investigated. As such, all events within selected photopeaks were used in Compton reconstructions.

Detection and spatial localization of large-energy deposition events is difficult in CdZnTe. Previous measurements of high-energy, gamma-ray sources using analog ASICs suffered from insufficient dynamic range and corresponding signal saturation [124]. The energy resolution of high-energy photopeaks was additionally degraded by uncorrected transient signals induced on neighboring anode pixels [125]. Recent, high-dynamic range, digital ASICs have made the problem more tractable [30]. Complete waveform digitization in new, digital CdZnTe systems enables correction of severe transient signal crosstalk between neighboring anode pixels. Crosstalk corrections improve system energy resolution for high-energy photons, enabling isotope specific imaging by selecting specific photopeaks.

7.2 Qualitative Shielding Analysis

The spatial production of neutron inelastic scatter and capture interactions in an object is strongly coupled to the free neutron density. Given some neutron source, the reaction rate of interaction type i in spatial region $d\bar{r}$ about $\bar{r}$ in an object is

$$I_i(\bar{r}) = \int_0^{E_{max}} v(E)N(\bar{r},E)\Sigma_i(\bar{r},E)dE \tag{7.1}$$

where $N(\bar{r},E)$ is the free neutron density in $d\bar{r}$ about $\bar{r}$ and dE about E, $v(E)$ is neutron velocity as a function energy and $\Sigma_i(\bar{r},E)$ is the cross section for interaction type i in $d\bar{r}$ about $\bar{r}$ and dE about E [26]. Energy dependent neutron flux, $v(E)N(\bar{r},E)$, will not be known in an object *a priori*. Therefore, only general statements about the presence of isotopes, not quantitative amounts, can be made from

recorded gamma-ray spectra.

Gamma rays from inelastic scatter or neutron capture in region $d\bar{r}$ about $\bar{r}$ can be localized spatially using gamma-ray imaging. Typically, only photopeak gamma rays are imaged. Selecting photopeaks insures emitted gamma rays have traveled through object shielding without subsequent interaction, which could change the apparent emission location, before detection. Assuming angularly isotropic detector efficiency, the number of detected, uninteracted, photopeak gamma rays per unit time from region $d\bar{r}$ about $\bar{r}$ is

$$D_i(\bar{r}) = \frac{\Omega(\bar{r}) f_i \epsilon_i I_i(\bar{r})}{4\pi} \int_{\bar{R}_{path}} e^{-\Sigma_T(i,\bar{r})} d\bar{r} \tag{7.2}$$

where ϵ_i is the detector photopeak efficiency at the photon energy emitted by reaction i, $\Sigma_T(i,\bar{r})$ is the macroscopic cross section at $d\bar{r}$ about r at the photon energy emitted by reaction i, f_i is the fraction photon yield from interaction i, $\Omega(\bar{r})$ is the solid angle subtended by the detector for interactions at $\bar{r}$ and $\bar{R}_{path}$ is the path between $\bar{r}$ and the detector.

Most single-view, gamma-ray imaging techniques cannot provide 3-D, spatial information on gamma rays emitted in the far-field where there is no detector parallax. Due to this lack of parallax, gamma-ray images are commonly reconstructed in a spherical, 2-D angular domain. In this imaging domain, the gamma-ray signal from spatial voxels in the same angular direction (θ, ϕ) are integrated together through

$$D_i(\theta,\phi) = \int_{\bar{R}_{(\theta,\phi)}} D_i(\bar{r}) d\bar{r} \tag{7.3}$$

where $\bar{R}_{(\theta,\phi)}$ is a ray in direction (θ, ϕ) starting from the detector. This undesirable integration prevents the estimation of voxelized intensities when using only a single measurement view. Therefore qualitative statements about isotopic distributions can

only be made in the angular domain. However, research towards quantitative measurement of 3-D, elemental distributions is underway for small samples, placed in the near-field where there is large detector parallax, using a thermal neutron beam [126].

7.3 PVC and Polyethylene Experiment

Large polyvinyl chloride (PVC: C_2H_3Cl) and polyethylene (PE: C_2H_4) neutron targets were manufactured. The PVC target was constructed using six, 2.5 x 30 x 30 cm^3 PVC sheets held together by PVC dowels. A 5 cm diameter hole was drilled in five of the six PVC layers to allow for neutron source insertion. The PE target was a right-circular cylinder of 30 cm radius and 12 cm height. The targets were combined, separated by a hollow PE spacer, forming a 'dumbbell' shape. A ^{238}PuBe source was inserted into the PVC target hole. A technical drawing and photograph of the dumbbell geometry is shown in Fig. 7.1.

The CdZnTe detector was placed 45 cm away from the dumbbell centerline and elevated 15 cm above the table surface. Spectra and Compton images were collected over a three hour dwell at a 8.5 mR/h gamma-ray dose rate which corresponded to 2000 counts per second. A low, 100 keV low-energy-threshold was chosen, although it induced substantial detector dead time, to insure low-energy interactions in Compton scatter events were recorded.

7.3.1 MCNP Simulation

The dumbbell geometry was simulated using MCNP-PoliMi with PVC and PE material compositions taken from the PNNL Material Compendium [88,127]. Neutron inelastic scatter and capture cross sections for elements in the plastic targets were plotted in Fig. 7.2 for clarity while gamma rays emitted from each element are tabulated in Table 7.1. Hydrogen, chlorine and carbon inelastic scatter and capture locations were extracted from the collision file and plotted in Fig. 7.3. ^{35}Cl has a

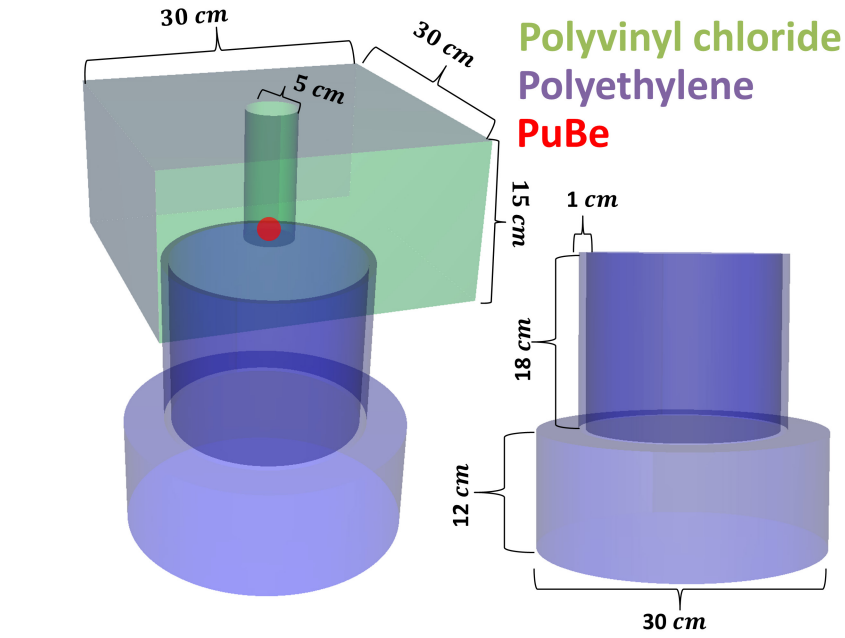

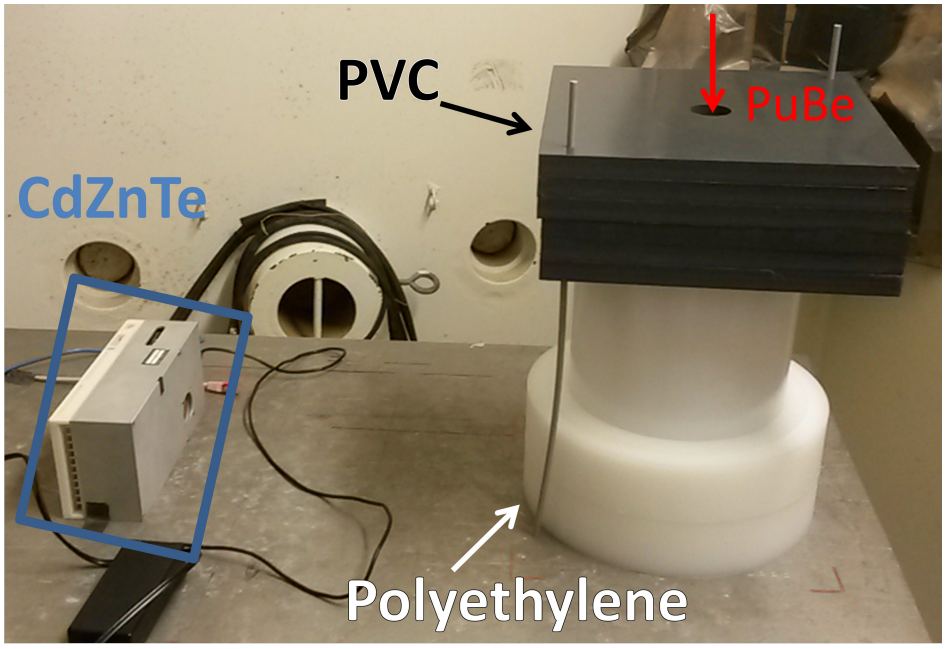

Figure 7.1: (Top) MCNP rendering of the dumbbell geometry consisting of two, large PVC and PE targets separated by a low mass spacer. Note the 18 cm PE spacer is hollow, with only 1 cm thick walls, to minimize the neutron interactions between the targets. (Bottom) Measurement setup before elevating the detector towards the center of the dumbbell. The detector was eventually elevated 15 cm above the table surface, 45 cm away from the target centerline.

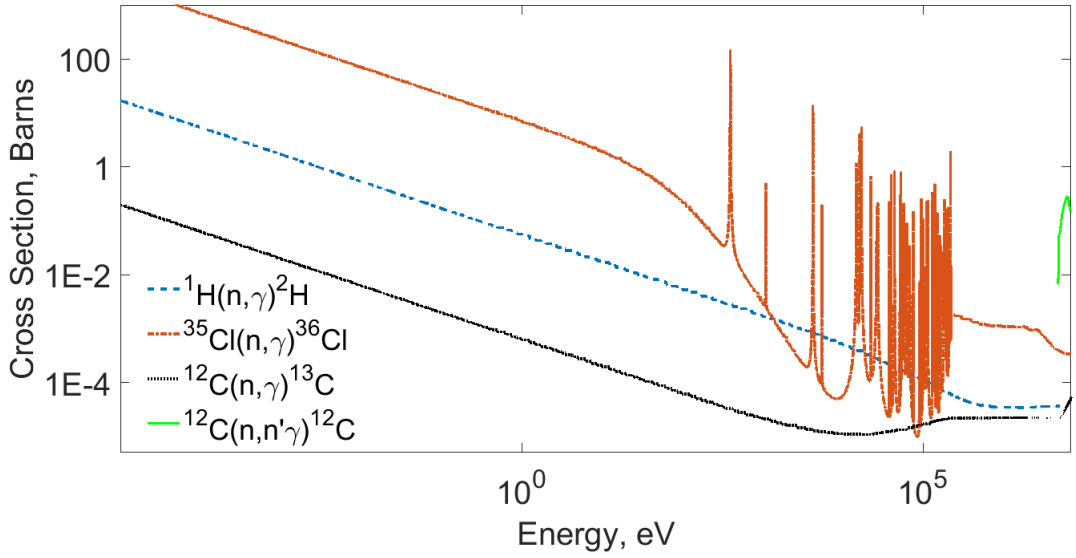

Figure 7.2: Neutron inelastic scatter and capture cross sections as a function of energy for ^{35}Cl, ^{1}H and ^{12}C. Note the resonant capture behavior in ^{35}Cl and threshold energy for inelastic scatter on ^{12}C. The thermal capture cross section of $^{35}\text{Cl} \gg {}^{1}\text{H} \gg {}^{12}\text{C}$.

much larger neutron capture cross section than ^{1}H, causing a great majority of PVC neutron captures to occur on ^{35}Cl. In PE, ^{1}H capture dominates over ^{12}C capture. Adding the low-mass spacer produces strong, spatially separated regions of mostly ^{1}H and ^{35}Cl neutron capture. This spatial separation corresponds to an angular separation of about 33° at a standoff of 45 cm. This angular separation is well within the resolving power of CdZnTe Compton imaging systems.

7.3.2 Measured Results

Spectra from a measurement of PVC alone and the combined PVC/PE dumbbell were plotted in Fig. 7.4. In the 1800-2400 keV spectral region, there are ^{35}Cl and ^{1}H capture peaks at 1.9 and 2.2 MeV, respectively. When the PE target is added, we see relatively more ^{1}H capture when compared to the PVC target alone. Clearly, the addition of PE introduced additional ^{1}H capture. Evidence of thermal neutron capture on ^{113}Cd and ^{10}B in the CdZnTe detector and printed circuit boards is also seen with peaks at 558 and 478 keV respectively [17]. Furthermore, Doppler broadened

Table 7.1: Prominent capture and inelastic gamma rays produced by chlorine, hydrogen and carbon [120] with corresponding isotopic abundances [119].

Element, % Abundance	Capture, E (keV)	Inelastic, E (keV)
^{35}Cl, 75.8%	517.1, 786.3, 788.4 1164.9, 1170.9 1951.1, 1959.3, 2863.8, 6111.0 6619.7, 6627.9, 7414.1, 7790.5	1219.3,1793.0, 2645.7 2693.8, 3002.3, 3162.8
^{1}H, 99.99%	2223.3	N/A
^{12}C, 98.9%	1100.0, 1261.8, 1270.0, 1860.0 3090.00, 3683.9, 4954.0, 4950.0	4438.9

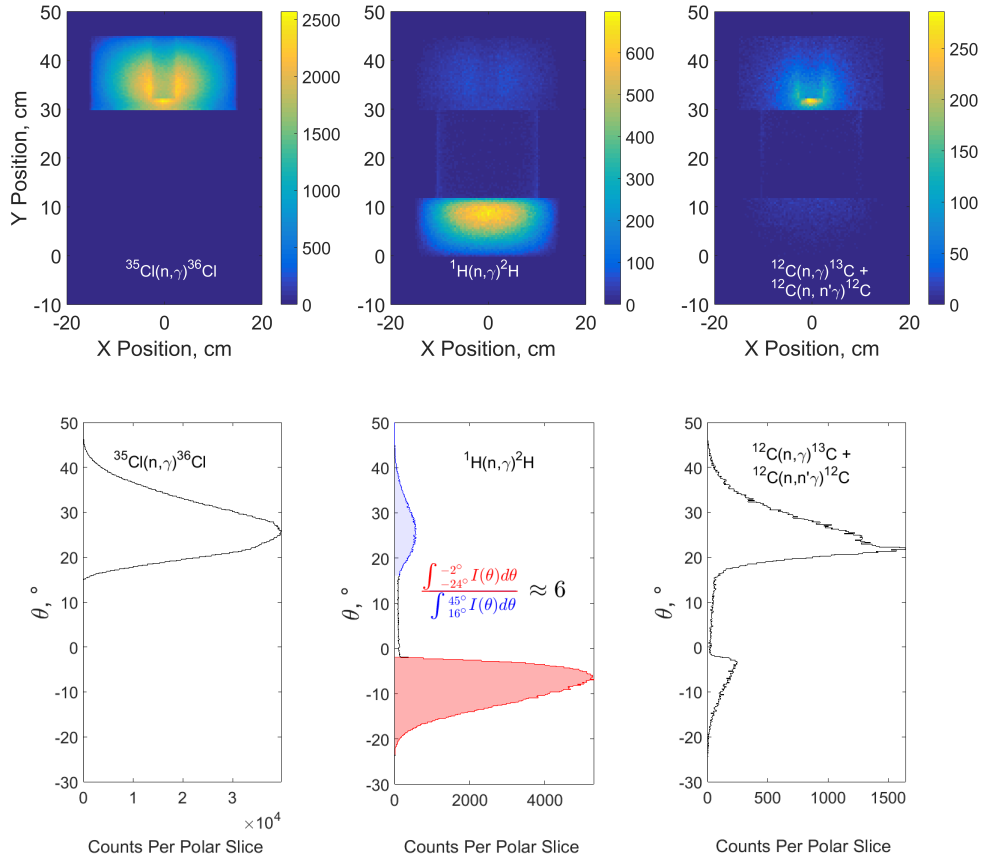

Figure 7.3: (Top) Cartesian projection of ^{35}Cl, ^{1}H and ^{12}C neutron inelastic scatter and capture in the dumbbell geometry simulated using MCNP-PoliMi. The PVC and PE targets span $y = [30, 45]$ cm and $y = [0, 15]$ cm respectively. (Bottom) Interaction locations on the Cartesian grid wee converted to spherical coordinates using $\bar{r} = [0, 15, 45]$ cm as an origin. Polar slices, computed by summing across the azimuthal direction, show clear separation of capture regions.

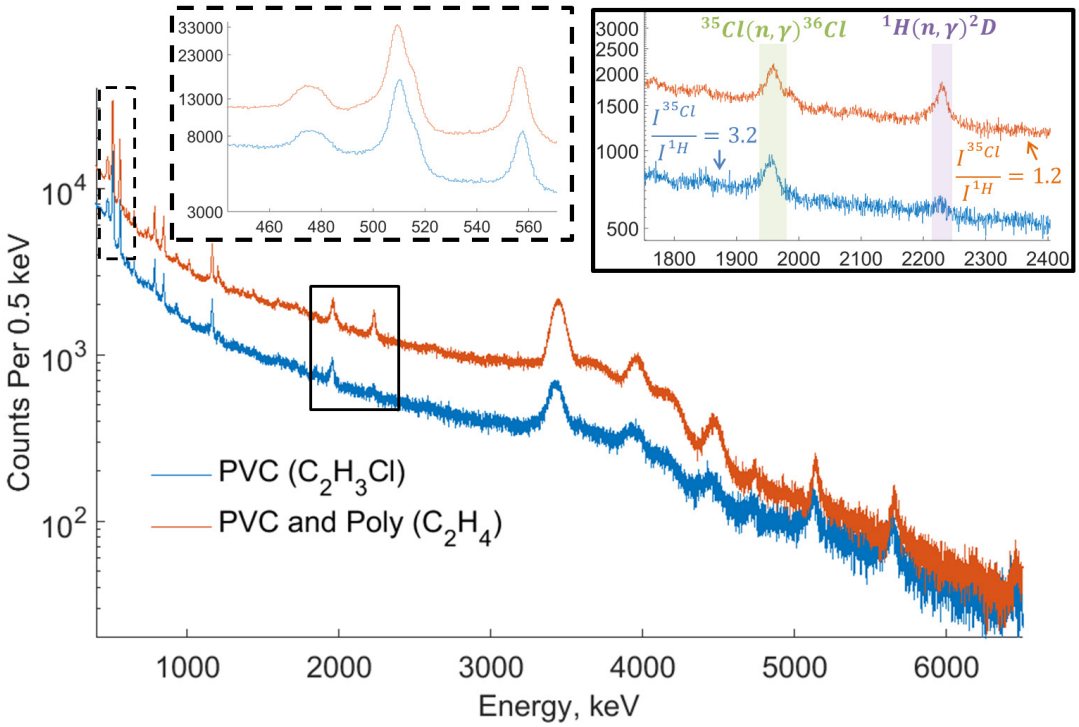

Figure 7.4: Gamma-ray spectra from the PVC target alone (blue) and the dumbbell geometry with PVC and PE (orange). The ratio of ^{1}H to ^{35}Cl capture increases with the addition of PE as shown in the solid, inset panel. Contamination the 517 keV ^{35}Cl capture gamma ray by pair production is seen in the dashed, inset panel.

4.4 MeV gamma rays from the deexcitation of ^{12*}C from ^{9}Be(α,n)^{12*}C in the PuBe source itself is seen.

The chlorine, neutron-induced, gamma-ray spectra appears to be dominated by thermal capture as evidenced by the relatively small, inelastic production of 1763 keV gamma rays relative to capture gamma rays at 1959 keV [128]. The small inelastic-to-capture ratio, used to estimate hydrogen content in chlorinated chemical weapons, is unsurprising given the three-to-one atom fraction of hydrogen to chlorine in PVC.

Compton images were generated using simple back-projection, binning on ^{35}Cl and ^{1}H capture gamma-ray energies and shown in Fig. 7.5. Compton images binning on 517, 1164 and 1951/1959 keV ^{35}Cl emissions show clear source hotspots around $(\theta, \phi) = (116, 273)°$. Notably, the 517 keV Compton image from ^{35}Cl capture is

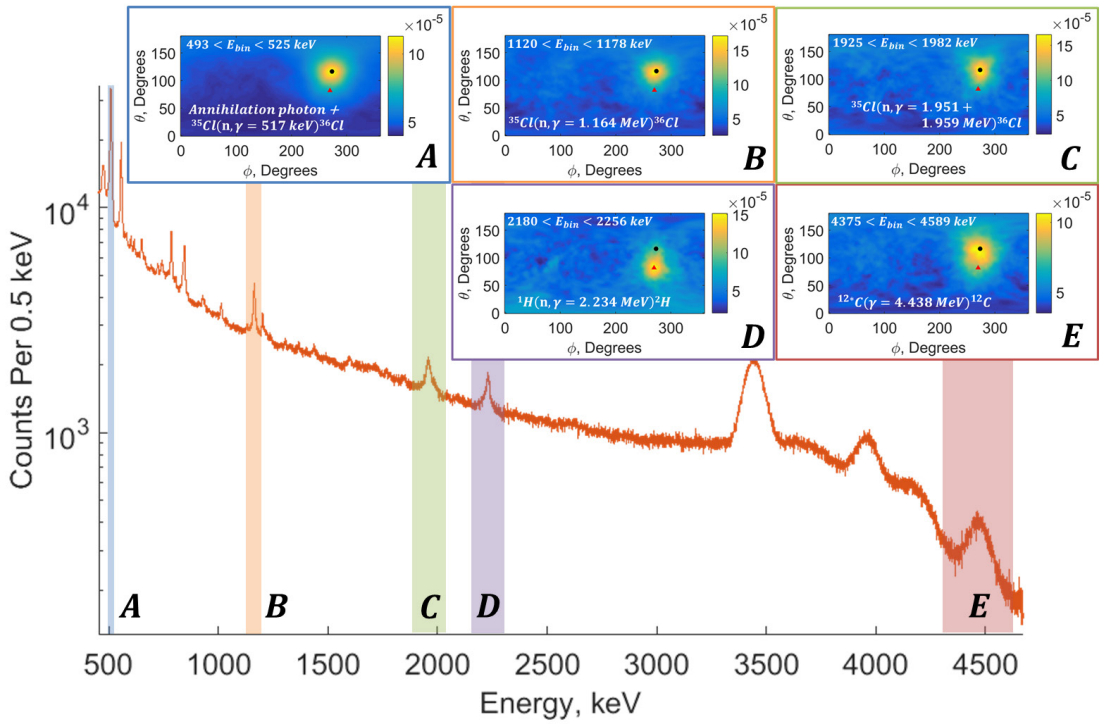

Figure 7.5: Compton simple-backprojection of ^{35}Cl(n,γ)^{36}Cl, ^{1}H(n,γ)^{2}H and ^{12*}C(γ)^{12}C gamma-ray lines. Compton back-projections of individual energy bins are color coded and lettered. A red triangle and black circle are placed in the center of hydrogen and chlorine hot spots, respectively, to guide the eyes.

slightly contaminated by annihilation photons from pair production of higher energy gamma rays in the targets. Binning on the 4.4 MeV ^{12*}C deexcitation line produces a hotspot in a similar direction to ^{35}Cl gamma rays. This is unsurprising as the PuBe source was placed inside the PVC target. Contrastingly, binning on the 2234 keV emission of neutron capture on ^{1}H produces a hotspot at $(\theta, \phi) = (82, 270)°$. Polar slices through the center of Compton hotspots are shown in Fig. 7.6, emphasizing the similar locations of ^{35}Cl and ^{12*}C hotspots, which are well separated from ^{1}H. Taking the maximum of each polar slice as the hotspot centroid, ^{35}Cl and ^{1}H captures appear separated by roughly 34° in the polar dimension, which agrees well with the value predicted from MCNP simulation. This shows that neutron-induced gamma rays can be Compton imaged to provide angularly resolved estimates of shielding material isotopics.

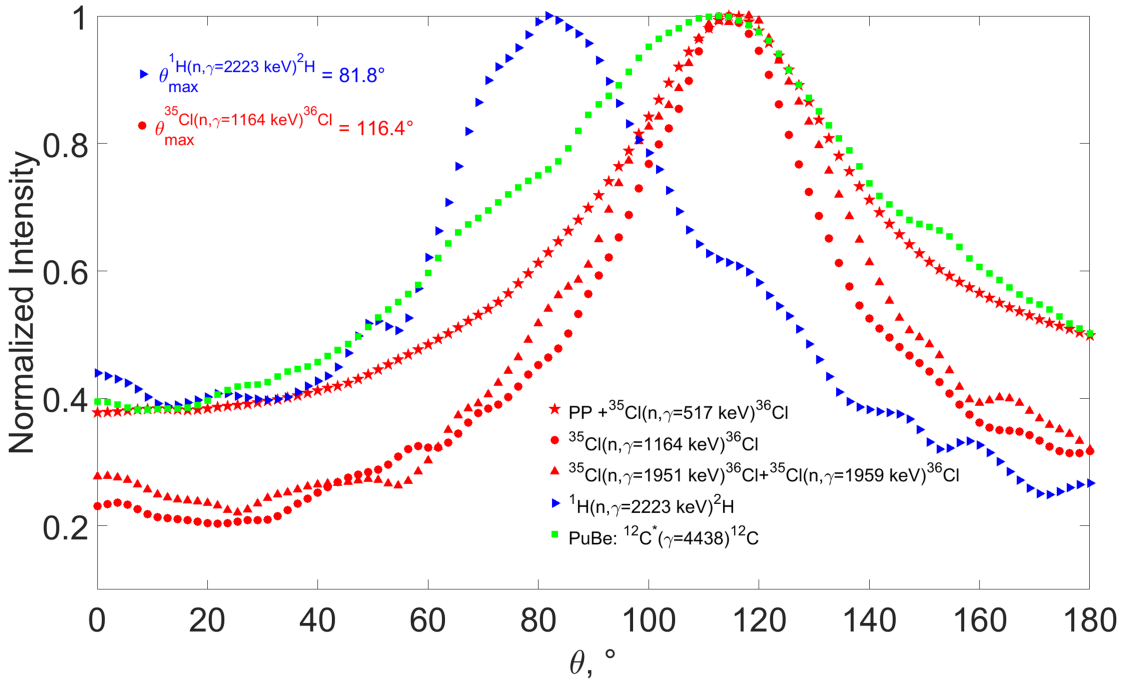

Figure 7.6: Polar slices (θ) through each hot spot in Fig. 7.5. The separation between ^{35}Cl(n,γ)^{36}Cl hot spots, in red, and ^{1}H(n,γ)^{2}H hot spot in blue is roughly 35°.

Neutron-induced gamma rays can also be externally excited. One example is the Portable Isotopic Neutron Spectroscopy (PINS) system at INL. In the PINS system unknown objects, such as artillery shells, are interrogated using ^{252}Cf or neutron generators where outgoing gamma rays from explosives or chemical weapons are detected using a non-imaging, HPGe detector [129]. Similar spatially-resolved, isotopic maps could be generated using pixelated CdZnTe. Imaging neutron-induced gamma rays from a surrogate artillery shell, shown in Fig. 7.7, was attempted. However, this measurement was unsuccessful due to insufficient system efficiency. A larger, more efficient CdZnTe system consisting of four, 3 by 3 planes of 2.0 x 2.0 x 1.5 cm^3 crystals is being developed. With four times the active volume of current systems, the detection efficiency of high-energy gamma rays should be greatly improved.

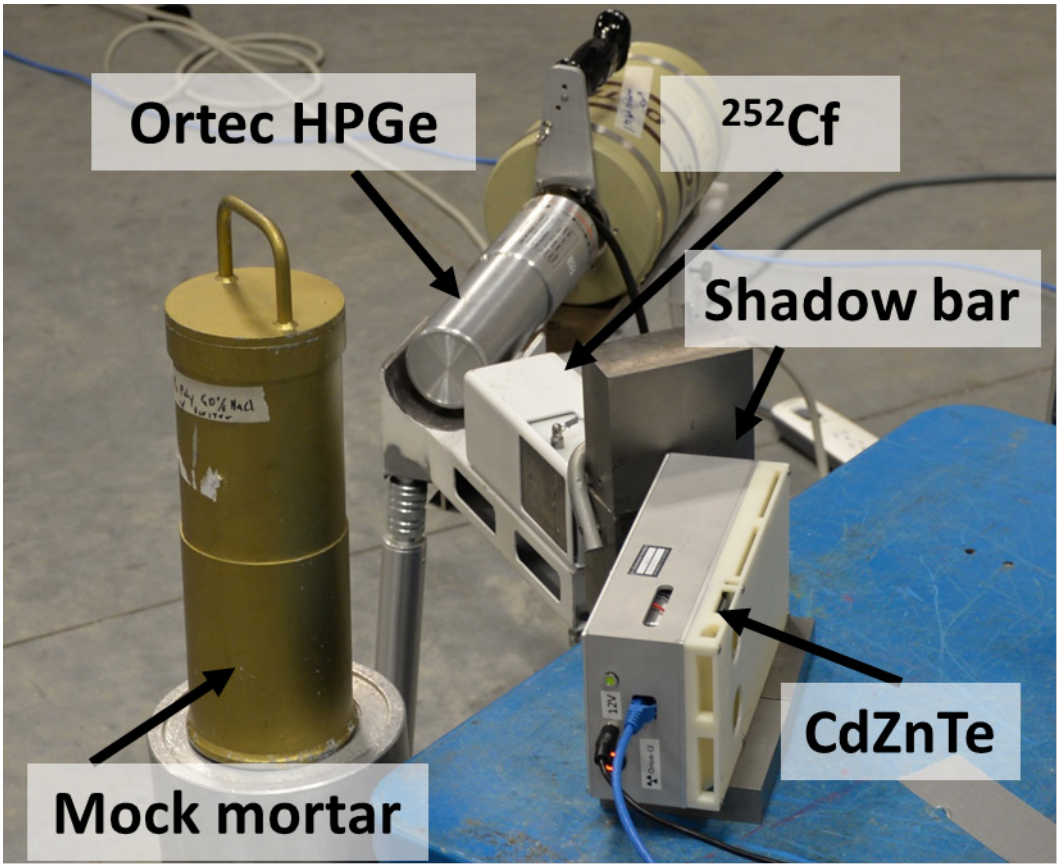

Figure 7.7: Neutron interrogation of a surrogate artillery shell via ^{252}Cf using the commercial, HPGe-based PINS system and a CdZnTe array.

7.4 Conclusion

Neutron-induced gamma rays can be detected and imaged using 3-D, pixelated CdZnTe detectors. Neutron-induced gamma rays offer isotope-specific, compound-shielding signals that are complementary to photon-attenuation-based shielding characterization techniques. These compound-shielding signals can be leveraged to provide contextual information on unknown spaces. For example, the presence of high-explosives around plutonium could be verified by imaging both neutron-induced gamma rays from nitrogen, carbon and hydrogen as well from plutonium decay [88]. In principle, the spatial relationship between gamma-ray hot spots from plutonium and high-explosives could be used to verify warhead dismantlement. Furthermore, these techniques can be expanded to 3-D via collecting multiple object views at different angles.

Associated particle imaging (API) neutron generators [130] can be leveraged to produce high-resolution, source distributions. API neutron generators record the momentum vector of either the triton or alpha particle, for DD and DT fusion respectively, to estimate the direction of individual, outgoing neutrons. Assuming inelastic gamma rays are produced on the first neutron scatter, the API momentum vector and Compton cone only agree at two, discrete points. This could be used to greatly improve Compton imaging algorithms used in mapping isotopics. Furthermore, Compton imaging offers the ability to spatially localize neutron capture gamma rays. Neutron capture cross sections typically increase with decreasing neutron energy, requiring generator neutrons to undergo several scatters. These scatters deflect neutrons off their original directional vector. This limits API localization performance for elements detected via thermal capture. None such limitation exists with Compton imaging systems, as the technique is agnostic to the number of preceding, neutron scatters.

CHAPTER VIII

Gamma-Ray-Based SNM Grading

8.1 International Safeguards and Nondestructive Assay

Both plutonium and uranium can be encountered in many isotopic forms. Natural uranium consists of both ^{235}U and ^{238}U with roughly 0.7 and 99.3 % relative, isotopic abundances. Plutonium, a non-natural element made in nuclear reactors, has isotopes ranging from ^{238}Pu through ^{244}Pu. Although both plutonium and uranium have peaceful applications in nuclear power, research and medicine, certain fissile isotopes, such as ^{233}U, ^{235}U and ^{239}Pu, can be used in nuclear weapons. Therefore, the use of both plutonium and uranium is controlled and monitored through the IAEA to prevent the proliferation of nuclear weapons.

In general, only plutonium containing less than 6.0% ^{240}Pu, known as weapons-grade plutonium (WGPU), or uranium containing greater than 93% ^{235}U, known as highly-enriched uranium, are used in nuclear weapons [131]. Many IAEA tasks center around verifying whether the isotopics of unknown plutonium and uranium samples match user declared values. Many techniques exist to quantitatively assay plutonium and uranium isotopics. Assay is broken down into either destructive or non-destructive categories. Destructive techniques, such mass spectroscopy, destroy the original sample, while non-destructive techniques, such as radiation detection, leave the specimen undamaged. As such, non-destructive techniques are greatly preferred.

Unknown plutonium and uranium isotopics can be measured non-destructively using neutron and gamma-ray emissions [24]. This work focuses on the non-destructive, gamma-ray-based assay of both uranium and plutonium isotopics following the analysis presented in *Goodman et. al* [132].

8.2 FRAM v5.2 Spectroscopy Software

FRAM (Fixed-energy Response function Analysis with Multiple efficiency) is a software that estimates both plutonium grade and uranium enrichment from gamma-ray spectra. FRAM estimates spectral peak areas, correcting for object self-shielding and detector efficiency in a combined efficiency curve, to estimate an emitted gamma-ray flux. Prominent characteristic gamma rays from uranium and plutonium isotopes used by FRAM are tabulated in Tab. 8.1 and Tab. 8.2 respectively. Uranium isotopics in FRAM can be estimated using two energy ranges: 120-1001 keV, where 186 and 1001 keV is used for ^{235}U and ^{238}U respectively, and 60-250 keV, where 186 keV is used for ^{235}U and 92.4 keV along with x-rays are used for ^{238}U. Contrastingly, ^{240}Pu has strong emissions spanning from 45-624.5 keV. This means FRAM can estimate ^{240}Pu content, and therefore determine whether unknown plutonium material can be used in a weapon, via several energy windows. Common FRAM plutonium windows include 60-230, 120-460 and 180-1010 keV which target low, medium and high-energy emissions respectfully.

FRAM is traditionally run on gamma-ray spectra from either planar or coaxial HPGe detectors. Planar germanium detectors typically have better energy resolution at the expense of lower high-energy efficiency [133]. FRAM has also been demonstrated on CdTe detectors and microcalorimeters [134, 135]. However, CdTe-based measurements were hindered by limited detector efficiency. Recent spectra from digital CdZnTe systems are similar to that of large, coaxial germanium detectors with single-pixel energy resolutions of around 0.4 % FWHM for large, efficient, nine-crystal

Table 8.1: Energies and intensities of prominent, uranium gamma rays for common isotopes taken directly from [24].

Isotope	Energy, keV	Specific Intensity, $\frac{\gamma}{g \cdot s}$
^{232}U	129.1	$6.5 \cdot 10^8$
	270.5	$3.0 \cdot 10^7$
	327.8	$2.7 \cdot 10^7$
^{233}U	119.0	$3.9 \cdot 10^4$
	120.8	$3.2 \cdot 10^4$
	146.4	$6.6 \cdot 10^4$
	164.6	$6.4 \cdot 10^4$
	245.3	$3.8 \cdot 10^4$
	291.3	$5.8 \cdot 10^4$
	317.2	$8.3 \cdot 10^4$
^{235}U	143.8	$7.8 \cdot 10^3$
	163.4	$3.7 \cdot 10^3$
	185.7	$4.3 \cdot 10^4$
	202.1	$8.0 \cdot 10^2$
	205.3	$4.0 \cdot 10^3$
^{238}U in eq. with ^{234m}Pa	742.8	$7.1 \cdot 10^0$
	766.4	$2.6 \cdot 10^1$
	786.3	$4.3 \cdot 10^0$
	1001.0	$7.5 \cdot 10^1$

Table 8.2: Energies and intensities of prominent, plutonium gamma rays for common isotopes taken directly from [24].

Isotope	Energy, keV	Specific Intensity, $\frac{\gamma}{g \cdot s}$
^{238}Pu	43.5	$2.5 \cdot 10^8$
	99.9	$4.6 \cdot 10^7$
	152.7	$6.1 \cdot 10^6$
	766.4	$1.4 \cdot 10^5$
^{239}Pu	51.6	$6.2 \cdot 10^5$
	98.8	$2.8 \cdot 10^4$
	129.3	$1.4 \cdot 10^5$
	203.5	$1.3 \cdot 10^4$
	345.0	$1.3 \cdot 10^4$
	375.0	$3.6 \cdot 10^4$
	413.7	$3.4 \cdot 10^4$
	646.0	$3.4 \cdot 10^2$
	717.7	$6.3 \cdot 10^1$
^{240}Pu	45.2	$3.8 \cdot 10^6$
	104.2	$5.9 \cdot 10^5$
	160.3	$3.4 \cdot 10^4$
	642.5	$1.1 \cdot 10^3$
^{241}Pu in eq. with ^{237}U	103.7	$3.9 \cdot 10^6$
	148.6	$7.2 \cdot 10^6$
	164.6	$1.7 \cdot 10^6$
	208.0	$2.0 \cdot 10^7$
	332.4	$1.1 \cdot 10^6$
	370.9	$1.0 \cdot 10^5$

arrays. A comparison of pixelated CdZnTe spectra against common scintillators and HPGe detectors is shown in Fig. 8.1 for both uranium and plutonium. Digital CdZnTe energy resolution is competitive with that of large, coaxial HPGe detectors, while much better than new, medium resolution scintillator detectors like $LaBr_3$. Commercial pixelated CdZnTe, using analog readout, in the H3D A400 has three times better energy resolution (at 186 keV) than the CdZnTe-based FLIR R300.

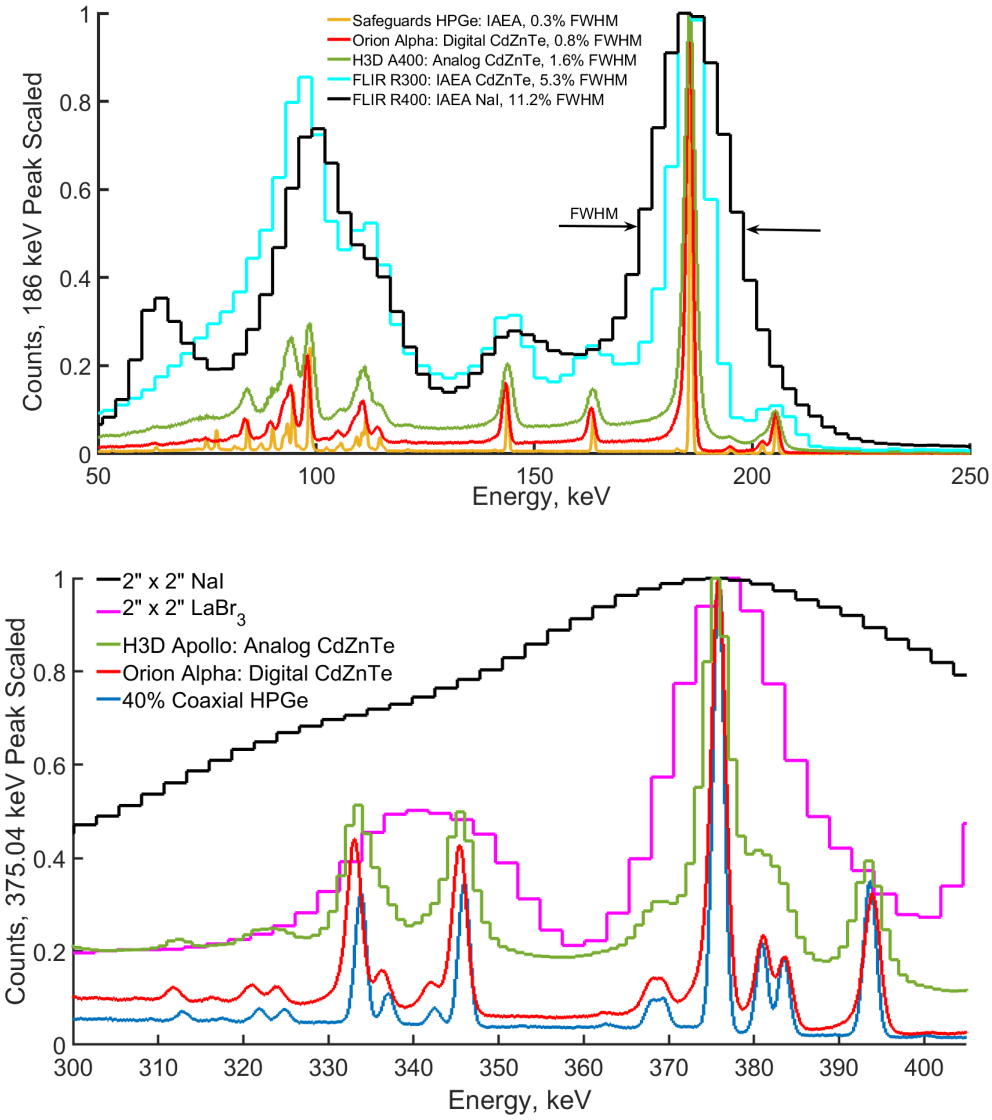

Figure 8.1: Comparing CdZnTe performance relative to scintillators and coaxial and planar HPGe detectors for uranium (top) and plutonium (bottom). Digital, pixelated CdZnTe energy resolution is closer to that of large, coaxial HPGe detectors than 'high-resolution' scintillators such as $LaBr_3$. The energy resolution of planar-like HPGe detectors, such as the hybrid safeguards detector, is much better than that of coaxial HPGe at low energies due to reduced electronic noise. Low-energy tailing is seen across pixelated CdZnTe systems stemming from the complicated, pixelated readout.

8.2.1 Coupling CdZnTe Spectra With FRAM

An effort to modify FRAM to improve analysis using medium resolution detectors, including $LaBr_3$ and CdZnTe, is underway [136], but is still in the development phase. This development includes modification of peak fitting algorithms to incorporate the large, low-energy tail present in common commercially available CdZnTe systems, which is minimized in recent, pixelated CdZnTe systems. However, attempts were made to estimate plutonium and uranium isotopics using current, pixelated CdZnTe systems and FRAM v5.2 with slightly-modified, HPGe peak shapes. Uranium and plutonium samples were measured across several Department of Energy sites. Detailed material specifications for most objects can be found in [137–144].

Gamma-ray spectra from Orion digital CdZnTe systems and a commercial H3D H400 CdZnTe detector were analyzed with the commercially released Ortec FRAM v5.2 software. No modifications to the peak fitting or other analysis algorithms were performed. Default parameter sets for analysis of uranium, plutonium and MOX with coaxial HPGe detectors in the high-energy region (120-1001 keV) were modified for shaping and energy resolution for each CdZnTe system. Robust performance was demonstrated over the range of uranium materials measured with this modified parameter set.

For several of the measurements where either large item mass, container or filter conditions allowed for efficient detection of x-rays, default parameter sets for determination of uranium and plutonium isotopic composition with planar HPGe detectors in the x-ray region (60-230 keV) were modified for shaping and energy resolution of the Orion CdZnTe systems. Due to relatively low count rates, resulting from the low detector volume and rejection of non-single pixel events, this analysis offered little improvement in evaluation of the composition of primary Pu isotopes such as ^{240}Pu and ^{239}Pu, but did allow improved measurement of ^{241}Pu, significantly decreasing the relative standard deviation (RSD) from 30-60% to 5-6%. Minimal improvement in

measurement of ^{235}U enrichment was observed using this approach.

8.3 Results

Digital Orion CdZnTe gamma-ray spectra for a subset of measured plutonium and uranium objects are shown in Fig. 8.2 and Fig. 8.4 respectively. Similar spectra were generated, albeit with slightly worse resolution, for A400 measurements. Clear differences in ^{241}Am content and total fast neutron emission rates are seen between plutonium samples. FRAM v5.2 estimates of ^{240}Pu content for each object are shown in Fig. 8.3 and tabulated in Tab. 8.3 calculated using high-energy, 120-800 keV, gamma-ray emissions. Analysis was omitted using lower-energy, 60-230 keV, gamma-ray emissions due to low object penetration, but agreed well with the higher energy results [145]. Previous work, using a smaller subset of plutonium objects, showed estimated ^{240}Pu isotopics agreed to within 3σ statistical measurement uncertainty to the true value across a wide isotopic range [132]. Subsequent analysis with more objects revealed one sample (M-2-Pu0002) with 3.1σ difference between FRAM estimated ^{240}Pu and reality. Even with this larger than 3σ deviation it appears that digital CdZnTe systems can clearly separate weapons-grade from high-burnup, reactor plutonium. Similar analysis was conducted using the H3D A400 and 0.3 keV bins. Relatively worse plutonium grading was seen using the lower-resolution system: average ^{240}Pu estimate error divided by FRAM reported uncertainty was 1.0 and 2.2 for digital systems and the A400 respectively.

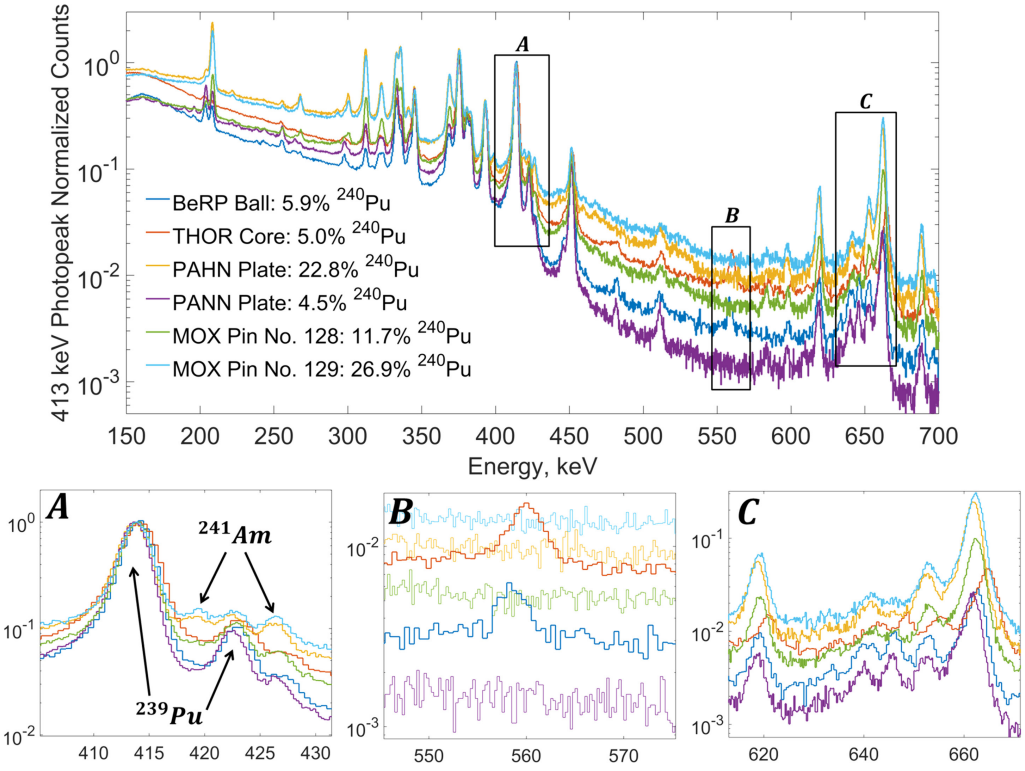

Figure 8.2: Single-pixel, CdZnTe spectra of plutonium and MOX objects normalized to the 413 keV photopeak from ^{239}Pu. Inset A shows disparate ^{241}Am content between weapons and reactor grade objects. Inset B shows evidence of thermal neutron capture on ^{113}Cd at 558 keV for massive, plutonium objects. Inset C shows the energy-region used to determine ^{240}Pu content. Source details are provided in [137, 138, 140, 141].

Differences between 186 and 1001 keV count rates were seen between low and highly-enriched uranium samples. Spectra were processed using FRAM v5.2 and modified default parameters for LEU (low-enriched uranium) and HEU (high-enriched uranium) using high-energy, 120-1001 keV gamma-ray emissions and shown in Fig. 8.5 and tabulated in Tab. 8.4. Systematic overestimation of enrichment was seen for low enrichments using LEU parameters for Orion 2.2 measurements. No data in this enrichment range was taken with other systems to tell if this error was systematic. A similar biased, overestimation may occur for the 21.0% enriched object using the Orion Alpha and H3D A400 system. Regardless of these potential issues, commercial reactor fuel, roughly 3-4% ^{235}U, can be readily separated from HEU. This shows that

Table 8.3: True and FRAM v5.2 estimates of plutonium content across several digital CdZnTe systems including Orion Alpha, Orion Beta, Orion 2.2 and the Orion Prototype. A smaller subset of measurements were conducted with a commercial, H3D A400.

	Digital CdZnTe		H3D A400	
Object	^{240}Pu, Weight % True, Estimated	^{239}Pu, Weight % True, Estimated	^{240}Pu, Weight % True, Estimated	^{239}Pu, Weight % True, Estimated
BeRP Ball	5.9, 8.4±1.5	93.7, 91.6±1.5	N/A	N/A
THOR Core	5.0, 7.3±2.2	94.6, 92.2±2.2	N/A	N/A
PAHN Plate	22.8, 21.4±7.8	76.0, 77.0±7.7	N/A	N/A
PANN Plate	4.5, 6.4±1.0	95.4, 93.5±6.4	N/A	N/A
MOX 128	11.7, 12.4±2.0	87.8, 86.9±2.0	N/A	N/A
MOX 129	26.9, 20.0±3.7	72.2, 78.0±3.6	N/A	N/A
PSS 002	5.90, 8.0±1.1	93.9, 91.9±1.1	5.90, 11.6±4.4	93.9, 88.3±4.4
M-2-Pu002	5.27, 6.7±0.5	94.6, 93.2±0.5	5.27, 2.9±1.3	94.6, 97.0±1.3
Cell 250	5.94, 7.0±0.6	93.0, 92.9±0.6	5.94, 1.3±1.2	93.0, 98.6±1.2
CBNM84	14.20, 13.9±0.7	84.4, 85.5±0.6	14.20, 10.7±1.8	84.4, 88.7±1.8
CBNM70	18.29, 13.3±2.6	73.4, 83.3±2.5	18.29, 13.1±4.7	73.4, 82.8±4.8
CBNM61	25.40, 23.0±1.4	62.6, 71.4±1.4	25.40, 11.5±3.3	62.6, 85.4±3.3
H002289	40.80, 42.2±9.9	49.6, 51.2±9.0	40.80, 52.0±5.8	49.6, 39.9±6.0
H002052	18.46, 24.0±7.4	76.3, 71.4±7.1	18.46, 20.1±3.4	76.3, 75.1±3.6
SADZ1390	5.00, 6.0±1.1	93.2, 93.8±1.1	5.00, 2.1±0.4	93.2, 97.9±0.4
STDISO9	6.89, 8.6±2.0	92.6, 91.2±2.0	6.89, 6.4±1.3	92.6, 93.4±1.3
STDISO15	15.4, 17.3±4.0	82.1, 81.7±4.0	15.4, 22.7±5.3	82.1, 76.1±5.3

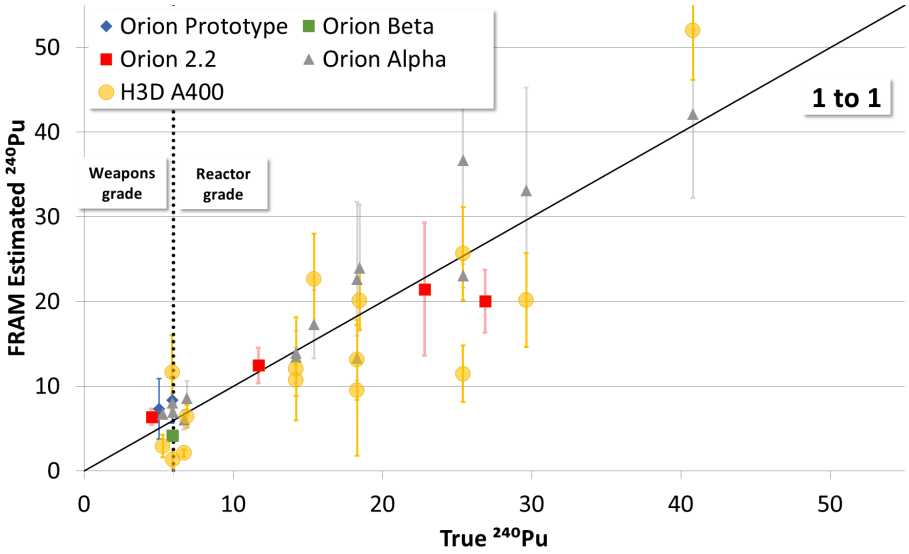

Figure 8.3: Estimated ^{240}Pu as a function of true plutonium content. Plotted error bars represent 1σ and are statistical in nature. Perfect estimation, corresponding to the 1 to 1 line, is shown in black.

digital Orion CdZnTe systems can be effectively coupled with FRAM v5.2 to estimate rough uranium enrichment. Similar analysis was conducted using commercial, A400 spectra. H3D software outputs all-events spectra with 1 keV bins by default. Single-pixel and all-events spectra were subsequently reprocessed using custom software with finer bins. Default and more finely binned, single and multi-pixel spectra, were analyzed with FRAM. Relatively good agreement between FRAM estimates of ^{235}U and true values were seen for all A400 spectra types. This suggests that commercial H3D A400 detectors, using the default, all-events spectrum with 1 keV bins, are immediately compatible with FRAM v5.2 to estimate uranium isotopics.

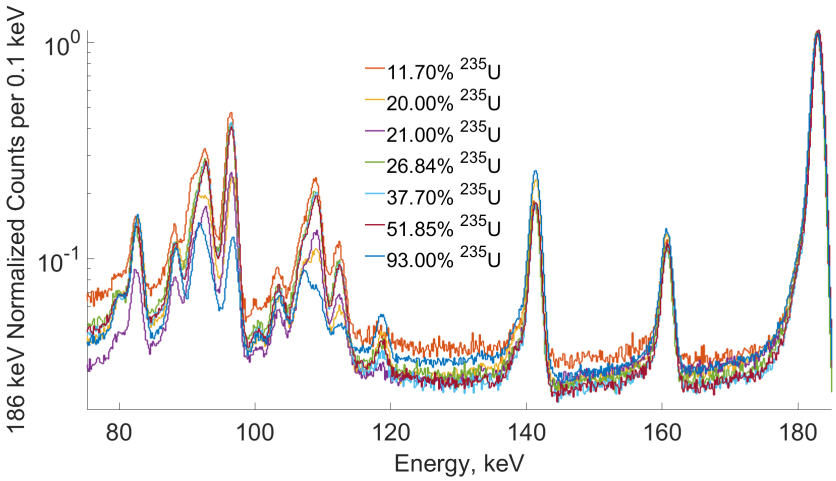

Figure 8.4: Single pixel ^{235}U spectra from several sample objects using Orion Alpha.

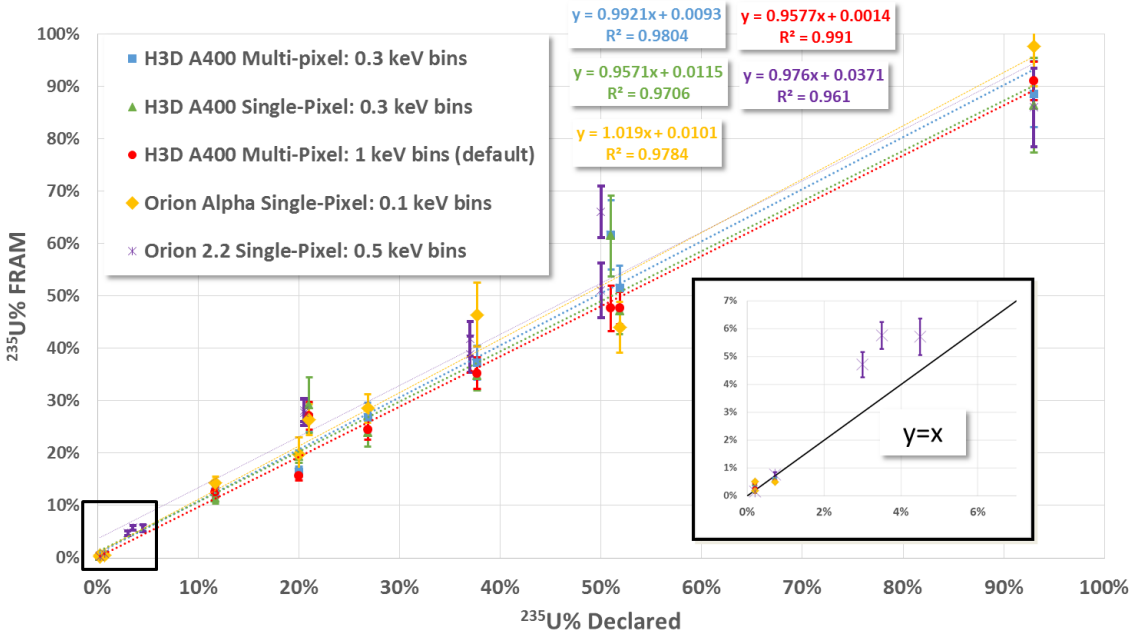

Figure 8.5: Declared and FRAM estimated ^{235}U mass percentages for two, digital CdZnTe systems and the commercial H3D A400. Plotted error bars represent 1σ and are statistical in nature. Linear fits, with associated R^2, are shown in the inset figures.

Table 8.4: (Top) True and FRAM v5.2 estimates of uranium content from Y12 [139] using the digital, Orion Prototype. Isotopic estimates were made using both LEU and HEU calibrated parameters. (Bottom) Isotopic estimates from samples at INL using both Orion Alpha and a H3D A400. Multi-pixel, A400 spectra were processed with 1 keV bins.

True Enrichment	Estimated Enrichment, LEU Parameters	Estimated Enrichment, HEU Parameters
0.2	0.15±0.05	N/A
0.7	0.76±0.08	N/A
3.0	4.7±0.5	N/A
3.5	5.8±0.5	N/A
4.5	5.7±0.7	N/A
20.5	28.2±2.2	27.8±2.5
37.0	41.8±3.2	38.8±3.4
50.0	51.1±5.3	66.0±5.0
93.0	N/A	86.0±7.5

True Enrichment	Estimated Enrichment, Orion Alpha	Estimated Enrichment, H3D A400
0.2	0.18 ± 0.03	0.19 ± 0.03
0.72	0.49 ± 0.11	0.59 ± 0.06
11.70	14.29 ± 1.23	12.61 ± 1.09
20.00	19.81 ± 3.22	16.44 ± 0.96
21.00	26.40 ± 2.92	26.82 ± 2.78
26.84	28.55 ± 2.73	26.82 ± 2.78
37.70	46.42 ± 6.06	37.28 ± 3.23
51.85	44.00 ± 4.87	51.52 ± 4.29
93.00	97.66 ± 7.72	88.56 ± 6.35

8.4 Conclusions

The energy resolutions of digital CdZnTe systems appear sufficient to coupled with the commercial software FRAM v5.2. Estimates of ^{240}Pu content calculated using gamma-ray spectra from several, digital CdZnTe systems, across multiple campaigns, show coarse agreement with declared ^{240}Pu values. Slight, systematic overestimation of ^{240}Pu content was observed for weapons-grade plutonium samples. Furthermore, larger-than-desired uncertainties in estimated ^{240}Pu content was seen across all material grades. These performance issues limit the application of coupled CdZnTe/FRAM v5.2 to simple problems, such as separating weapons-grade and very high-burnup plutonium. Coupled CdZnTe/FRAM v5.2 grading plutonium may be vastly improved using FRAM v6 with proper CdZnTe peak shapes.

Digital CdZnTe estimates of ^{235}U content using FRAM v5.2 agree with true values across two measurement campaigns. Commercial, off-the-shelf, H3D CdZnTe systems are capable of directly coupling to FRAM v5.2 to estimate uranium grade. In general, it appears that estimating plutonium isotopics is relatively more difficult than estimating uranium isotopics with both current analog and digital CdZnTe systems. Future comparisons between FRAM and H3D software estimated plutonium and uranium isotopics should be conducted.

CHAPTER IX

High-Resolution Coded Aperture Imaging of SNM

The spatial distribution of special nuclear material is informative of its designed use. For example, spherical objects may be intended for nuclear weapons while thin, cylindrical rods may be used in nuclear power [26, 131]. High-resolution imaging is required to extract source features, such as shape, from small objects. The poor angular resolution of traditional CdZnTe-based Compton imaging precludes the analysis of small, detailed objects. Coded aperture offers a higher-resolution alternative to Compton imaging. However, CdZnTe-based spatial coded aperture suffers from detector non-uniformity and gaps between crystals [64]. Detector gaps and non-uniformity cause severe, systematic artifacts which degrade image quality and complicate the extraction of detailed source shape. Furthermore, MURA-based reconstructions require an entire mask cycle to be recorded simultaneously. This constraint intrinsically limits the coupled image FOV and image resolution for a given detector size and position resolution.

Instead, an entire mask cycle can broken down into smaller, individual pieces that are recorded at different times. Mask pieces are then stitched together, forming a larger, coherent pattern, and used to reconstruct an image. This idea of temporally encoding mask information is not new, and has been implemented for a wide variety of applications ranging from medical imaging to homeland security [61, 146–148].

Recording mask information in the time domain is further simplified by the remarkably stable temporal performance of CdZnTe arrays. *Brown* illustrated near Poisson-limited temporal uniformity on analog detectors similar to those used in this work [17]. Recording information in the well-behaved time domain enables mask patterns to be recorded with high-fidelity. This process avoids the severe, spatial non-uniformity which intrinsically limits image quality in traditional, spatial-coded aperture.

Time-encoded measurements were conducted using the MIRA system. *Brown* developed the MIRA TEI system using analog, 3-D, position-sensitive CdZnTe detectors. Better than 2 mm imaging resolution was demonstrated using a single-photon emission computerized tomography (SPECT) line source [65]. Highly enriched uranium disks and a uranium radiation signature training device (RSTD) were also imaged at the Oak Ridge, Y12 facility. This chapter builds on the work of *Brown*, and leverages the MIRA system to image plutonium objects using new, digital CdZnTe arrays. In general, it closely follows the work presented in *Goodman et. al* [149].

9.1 MIRA Time-Encoded Imaging System

The MIRA TEI system consists of a position-sensitive CdZnTe readout plane, tungsten mask and translation stage as shown in Fig. 9.1. Two stepper motors temporally raster a variable thickness, rank 79 tungsten MURA mask in front of the detector array while list-mode data, containing interaction position, energy and time, are recorded [41]. In contrast to previous work, where the mask was discretely stepped through all 6241 positions, the mask was continuously rastered across each of the 79 rows to maximize imagable time per unit dwell; for measurements with discrete movements, time is wasted waiting for mask to stop and start. Furthermore, continuous movement can improve reconstructed image quality through the use of super-resolution [150]. Count rate vectors for each detector voxel and energy bin were cross-correlated with the known mask movement pattern and summed on a

common image grid after accounting for detector voxel offsets.

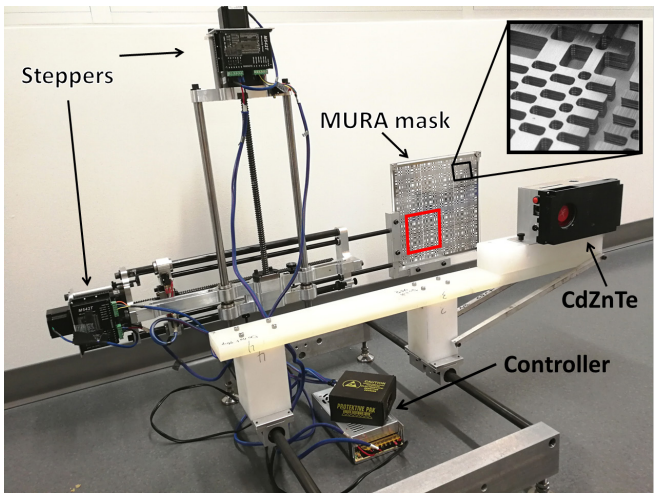

Figure 9.1: MIRA time-encoded imaging system consisting of a 2-D translational stage, position-sensitive CdZnTe detector and mask. The tungsten mask is a rank 79 MURA with 1.4 mm pixel pitch. One mask cycle is labeled in red while an inset image highlights mask detail.

9.2 Experimental Measurements

Two experimental campaigns were conducted using the MIRA TEI system instrumented with digital CdZnTe arrays. The first campaign, conducted at the Zero Power Physic Reactor (ZPPR) facility in INL, focused on old, high-burnup plutonium and MOX fuel. The second campaign focused on low-burnup plutonium inside the RSTD. Measuring both young, low-burnup and old, high-burnup plutonium is important when considering the relative photon emission intensities of isotopes tabulated in Table 8.3 of Chapter VIII. ^{241}Am, formed by ^{241}Pu which decays with a roughly 14 year half life, emits over 10^{10} 60 keV gamma rays per second per gram. ^{241}Am activity within an object depends both on the initial burnup, which dictates initial ^{241}Pu concentration, and object age, which controls how much of the initial ^{241}Pu has decayed. Example spectra illustrating the wide range of ^{241}Am concentrations encountered in this chapter are shown in Fig. 9.2. Object ^{241}Am content, and therefore

object brightness, can change by well over an order of magnitude across plutonium samples.

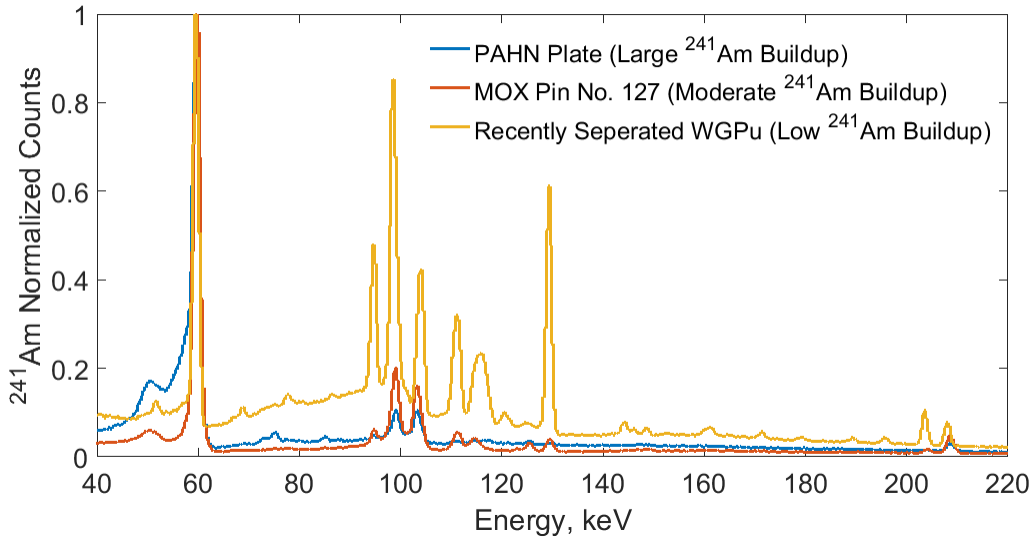

Figure 9.2: The 59.54 keV emission of ^{241}Am dominates the low-energy, coded-aperture-imagable spectra of old, high-burnup plutonium objects. X-ray emissions are comparable to the intensity of ^{241}Am in recently separated WGPu. Spectra were collected with Ortec Micro-Detectives [28]. Spectral differences are also convolved with the effects of slightly different shielding.

9.2.1 Aged Plutonium and MOX

A PAHN plutonium plate, collimated between two bismuth bricks to form a line source, was imaged at a mask-to-source and mask-to-detector distance of 10.7 and 35.5 cm respectively. Detailed source specification is provided elsewhere [140]. 1.7 mm of lead was placed between the source and mask to reduce detector dead time to a reasonable level while an image was rastered over 30 minutes. An image reconstructed using the 59.5 keV emission of ^{241}Am is shown in Fig. 9.3. Clear source shape and extent can be extracted from the image. The image generated using 59.5 keV gamma rays and the true object are functionally identical, showing that ^{241}Am can be used as a bright, imagable surrogate for plutonium.

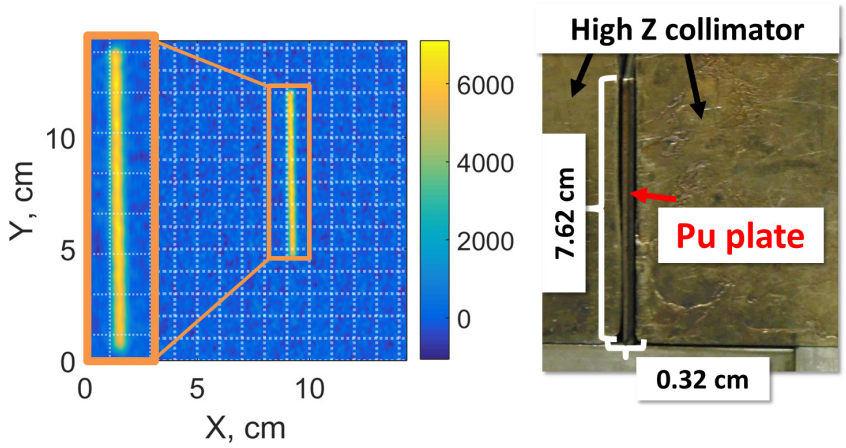

Figure 9.3: (Top) Time-encoded image of a PAHN plate collimated by two bismuth bricks to form a line source. The image formed using 59.5 keV gamma rays shows that ^{241}Am is a bright, imagable surrogate for plutonium. Inset images show the magnified source region. The white image grid has 1 cm spacing.

A second PAHN plate was added, separated from the first by a 6.3 mm bismuth spacer to form two parallel line sources, and imaged using the 59.5 keV signal over 30 minutes as shown in Fig. 9.4. The image signal-to-noise ratio (SNR) was decreased compared to Fig. 9.3 although the reconstruction has 1.5 times more imagable counts. This was unsurprising as the SNR of images reconstructed with a MURA mask decreases with increasing source extent [151]. Furthermore, the non-linear effect of detector dead time was larger given the increased source extent and therefore increased 59.5 keV count rate from the plutonium surface. Dead time degrades time-encoded images by scaling the recorded source pattern at a given time. This scale factor depends on incident count rate, which changes as the mask moves. Summing pieces of the true pattern, each scaled by a different dead time fraction, produces a systematically biased image. MIRA time-encoded reconstructions were found to be relatively robust to the non-linear effects of dead time for the measured, homogeneous, extended sources. Roughly the same amount of plutonium was unoccluded by the mask throughout the entire measurement, due to large object extent, causing similar dead time throughout the whole measurement. This relatively consistent level of dead

time limits systematic artifacts. However, dead time effects may be more severe for scenarios with bright point sources near the mask plane. For example, consider a measurement with two point sources near the mask plane. In this case, each point source will be completely covered and uncovered by mask elements. When covered, the count rate contribution from a source drops to near zero. Therefore the fraction of detector live time available to the other source, given that it is uncovered, will change drastically. As the number of point sources increases, which can be thought of as an extended source, roughly half will be uncovered at all times. This causes similar levels of dead time which limits degradation.

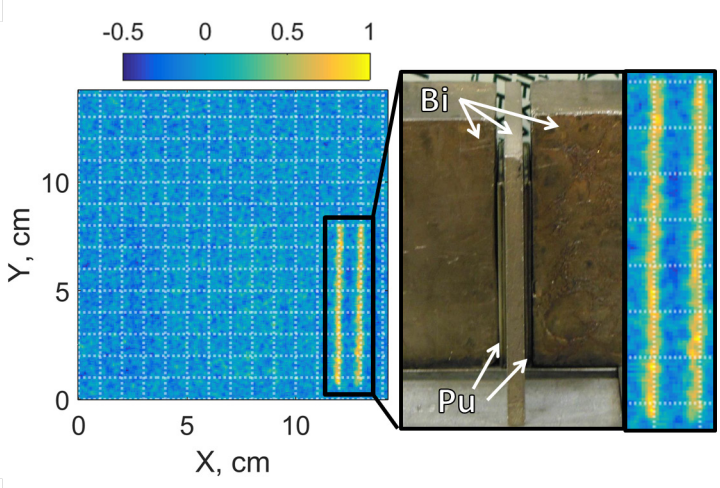

Figure 9.4: Time-encoded image of two PAHN plates collimated by two bismuth bricks and a 6.3 mm bismuth spacer to form two line sources. The image was formed using ^{241}Am gamma rays.

Four cylindrical MOX pins (ID. No 128) were placed into an aluminum holder and imaged from the top down looking at the disk faces at a mask-to-source and mask-to-detector distance of 10.5 and 39.5 cm respectively. Detailed source specifications are provided elsewhere [141]. A 30 minute image was taken with no additional lead shielding and is shown in Fig. 9.5. All four pins can be clearly separated in the aluminum holder while a central, steel cap is seen attenuating the low-energy, ^{241}Am gamma rays from all pins. This show that the distribution of both plutonium and

moderate shielding can be simultaneously measured.

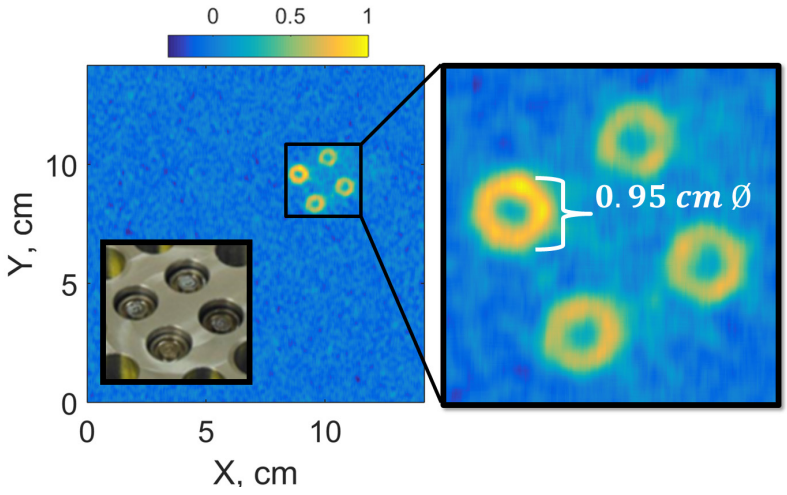

Figure 9.5: Time-encoded image of four No. 128 MOX pins in an aluminum holder. Pins were viewed disk face-on as shown in the inset image. The attenuating steel cap in the center of each pin is clearly seen while all four pins can be visibly separated.

9.2.2 Recently Separated Weapons Grade Plutonium

The low-energy emissions of recently separated WGPu are relatively weak given the small build-in of ^{241}Am. However, WGPu can still be readily imaged using emissions from plutonium itself. Coded aperture images of WGPu were taken using the RSTD. No detailed, isotopic datasheet on the RSTD was available but FRAM estimated 5.0±0.6% ^{240}Pu using spectra from an Ortec Micro-Detective. The RSTD is designed to simulate a large, spherical mass of plutonium using a thin, low-mass plutonium shell and internal ^{252}Cf neutron source. Plutonium in the center of an object can be omitted as gamma rays emitted near the center are attenuated by a large mass of plutonium. For example, the prominent 413 keV emission of ^{239}Pu has a mean-free-path (MFP) of only 1.8 mm in pure plutonium metal with a nominal density of 20 g/cm^3. Missing fission neutrons, which are more penetrative, are simulated via an internal ^{252}Cf source, albeit with lower fission-chain length. The roughly spherical RSTD is constructed of individual triangular facets placed into a steel frame.

Individual facets are broken down by internal baffles, forming four distinct triangular regions in a 'triforce'-shaped configuration. Slight gaps in the baffles allow for material migration between subtriangles. Subtriangles contain a plutonium-laden, ceramic felt. Triangles were carefully manufactured to contain the same cumulative activity. Triangle walls were made of thick stainless steel. This steel casing non-negligibly attenuates low-energy photons. Note that the low-burnup plutonium used in the RSTD and non-negligible steel shielding means that the recorded 60 keV signal of ^{241}Am is weak compared to that measured in either the MOX pins or ZPPR plates.

Two RSTD triangles were compared sided-by-side at high source magnification as shown in Fig. 9.6. Plutonium appears poorly-adhered to the ceramic felt in triangle C1-0101. Furthermore, poorly adhered powder appears to gather at the bottom of baffles due to gravity. Triangle C1-0101 was then rotated 180° and shaken ten times while the triangle C1-0122 was carefully rotated 180° without agitation. Both triangles were then re-imaged. Unsurprisingly, free powder in triangle C1-0101 moved with mechanical agitation, coming to rest in a new orientation. This clearly illustrates that time-encoded imaging can be used to distinguish small, object substructure in WGPu.

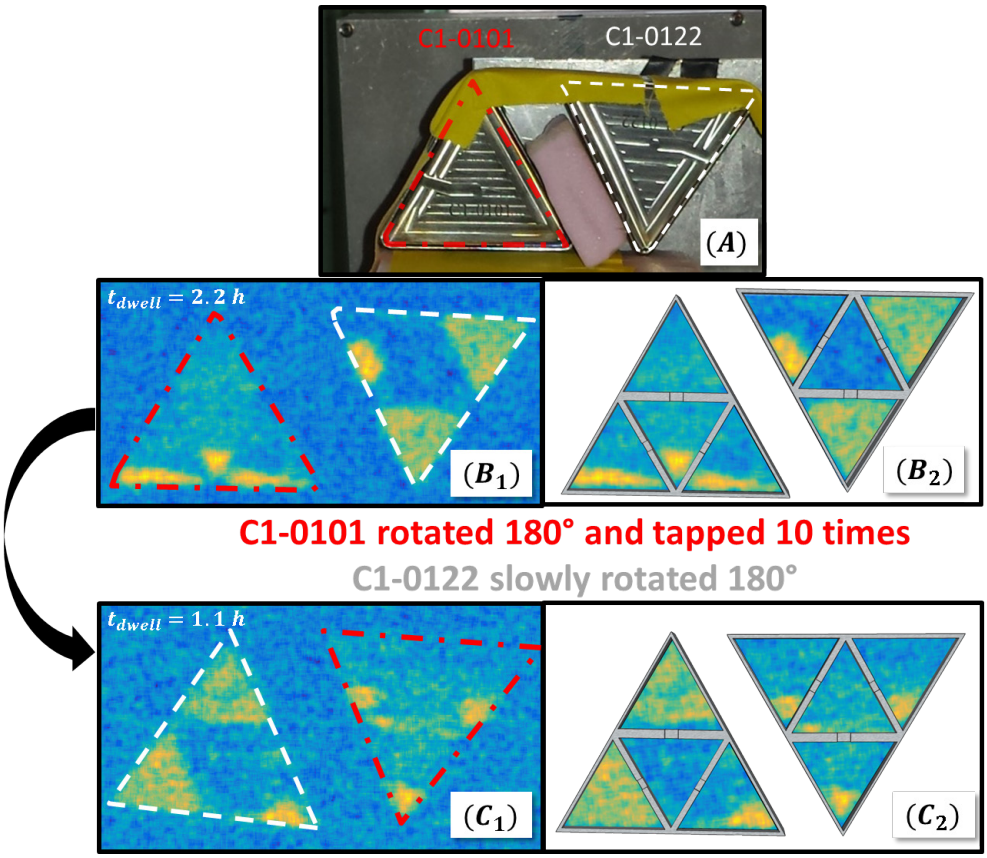

Figure 9.6: (A) Side-by-side triangular RSTD facets (C1-0101 and C1-0122) at source-to-mask and detector-to-mask distances of 2.5 and 20 cm respectively. (B_1) Simultaneous reconstruction of both triangular facets with object margins highlighted in red and white respectively. (B_2) Reconstructed images can be textured onto 3-D source models for context. Plutonium powder clearly rests at the bottom of baffles in C1-0101. (C_1) C1-0101 was then rotated 180° and tapped ten times. C1-0122 was slowly rotated without agitation. (C_2) Clear movement of free powder is seen in C1-0101. This suggests that plutonium inside facet C1-0101 is poorly attached to the ceramic felt when compared to C1-0122. Notably, some slight movement of free powder in C1-0122 was also seen.

The same triangular facet was imaged for roughly one hour at vastly different magnifications in Fig. 9.7 to demonstrate the trade off between imaging resolution and FOV. Imaging resolution, as discussed in detail by *Brown*, is controlled by the magnified size of projected mask features at the image plane

$$p_{image} = p_{mask}(1 + \frac{b}{a}) \tag{9.1}$$

where p_{mask} is the mask pitch, a is the mask-to-detector distance and b is the source-to-mask distance. As the size of the projected mask element, p_{image}, increases, imaging resolution decreases. This occurs when b, the source-to-mask distance, increases. Contrastingly the size of the FOV

$$L_{FOV} \simeq R p_{image} \tag{9.2}$$

increases with increasing source-to-mask distance where R is the mask rank. For the small source-to-mask standoff in panel B, all individual subtriangle elements are visible. Some evidence of the non-radioactive, stainless steel baffles is also seen. For the large source-to-mask standoff in panel A, the three bottom subtriangles blur together. However, as a trade-off, the size of the FOV substantially increased. In practice, an optimum resolution, SNR and FOV trade off can be decided *a priori* given some prior knowledge on the expected source configuration.

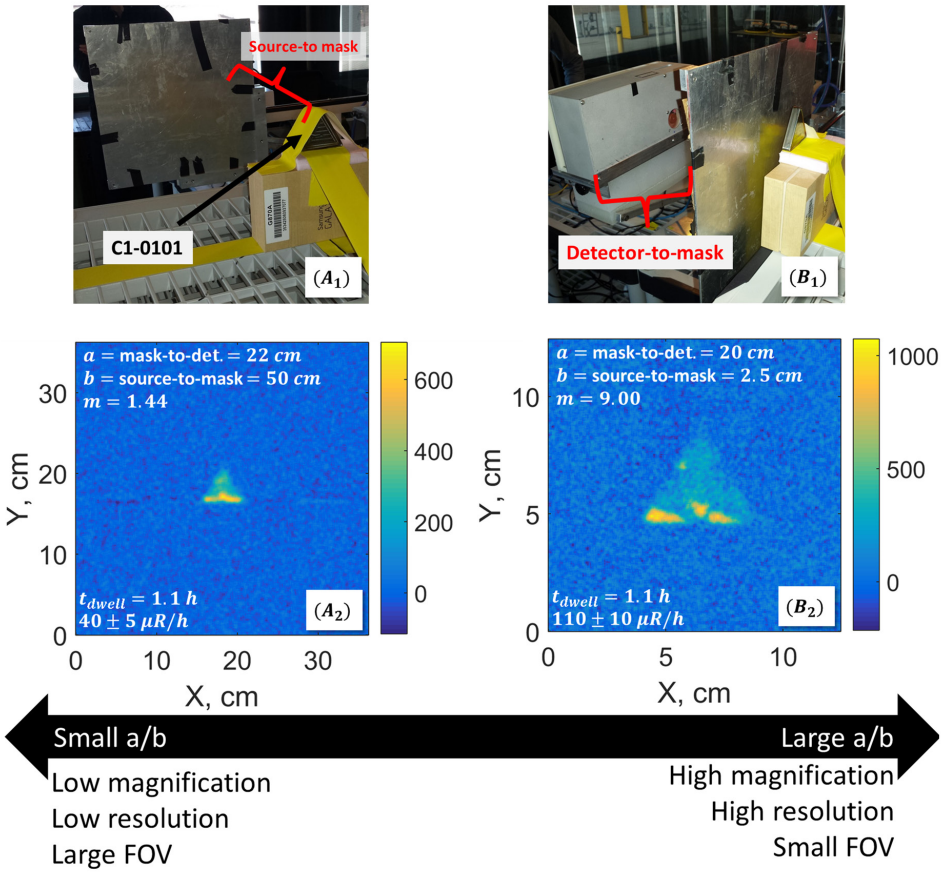

Figure 9.7: The ratio of source-to-mask and detector-to-mask distances controls mask pattern magnification at the detector plane, and therefore image resolution. Higher mask-pattern magnification produces better image resolution in B. However, reconstructed SNR in coded aperture reconstructions decreases with corresponding source extent in the FOV [151]. Similarly as image resolution decreases in A the size of the reconstructed FOV increases.

A high-resolution, time-encoded image of the assembled RSTD is shown in Fig. 9.8. The non-spherical, faceted shape of the RSTD is evident. Regions within the RSTD appear non-uniform, with maximum intensities between 'triforce' subfacets differing by as much as 50%. This facet non-uniformity is unsurprising given the mobile nature of poorly-adhered plutonium powder within each facet.

High spatial-resolution, quantitative imaging is possible using TEI. Source intensity within a region-of-interest (ROI) can be computed by summing pixel-wise image intensities. However, large covariance between image pixel intensities is seen in coded

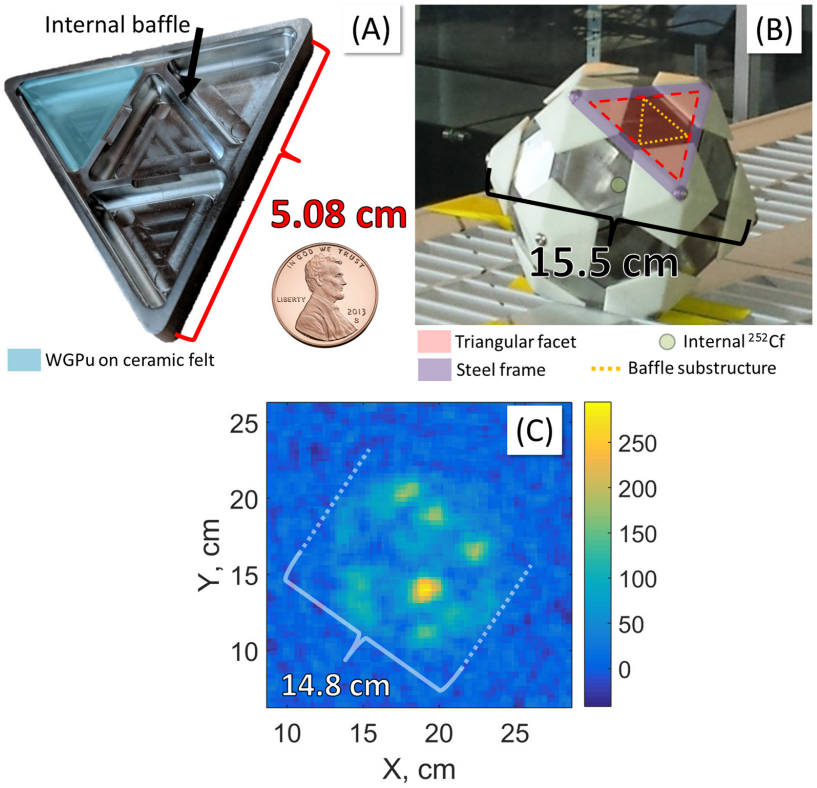

Figure 9.8: (A) The RSTD is composed of 5.08 cm triangular facets. Each facet contains an internal baffle substructure inside which plutonium felt is placed. (B) Each triangular facet rests in a steel frame with plastic end caps. A weak ^{252}Cf source is also placed in the sphere center to mimic the fast neutron emission rate of a solid sphere. (C) Coded aperture reconstruction of the whole RSTD taken at a mask-to-source and mask-to-detector distance of 100 and 22 cm respectively. Clear object heterogeneity is seen with non-spherical margins.

aperture imaging. This unwanted covariance complicates uncertainty estimates. Covariance between image pixels, which is particularly large for sub-sampled mask patterns, causes systematic underestimation of uncertainty in ROI intensity [152]. The effects of image pixel covariance are explicitly included when estimating uncertainty via bootstrapping. Bootstrapped intensity estimates of two triangular RSTD facets are shown in Fig. 9.9. Summed intensities from both triangles appear identical to within reconstructed uncertainties. This is unsurprising given the triangle manufacturing controls, suggesting that time-encoded imaging can be used for quantitative

analysis of complex, plutonium objects.

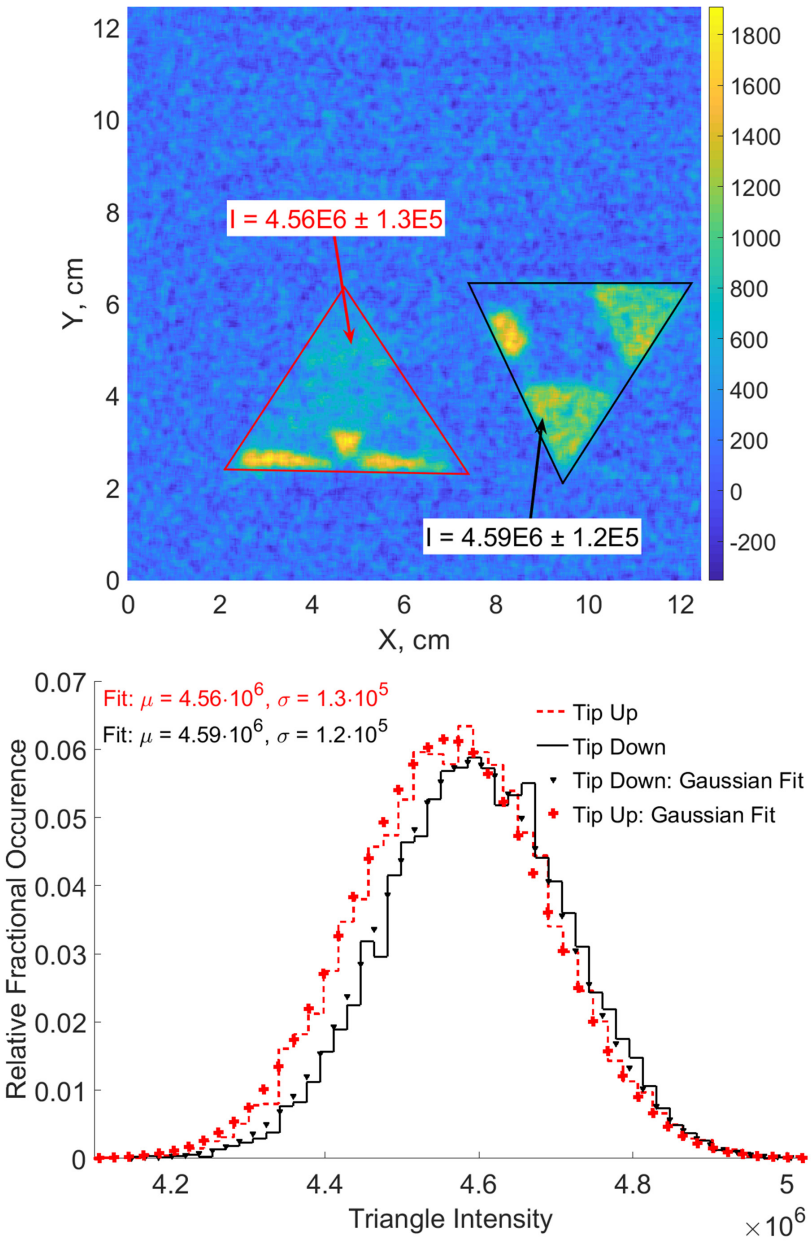

Figure 9.9: Quantitative intensity analysis for two, triangular RSTD facets. Selected ROIs correspond to each triangular object. The differences between estimated triangle activities appear small when considering the spread of bootstrapped intensity estimates for each triangle.

Time-encoded imaging can be used to extract directional spectra as discussed in Chapter III. A proof-of-concept, directional spectra measurement was conducted

using ^{241}Am, ^{57}Co and ^{133}Ba check sources. Sources were placed face-to-face, and separated by low-mass, plastic spacers as shown in Fig. 9.10. The assembled object was then rotated 45° and viewed edge on. Mask-to-source and mask-to-detector distances were 1.5 and 26 cm respectively over the 1 hour measurement. TEI reconstructions were conducted for each energy bin. Image pedestals were estimated and subtracted off each reconstruction using a human-chosen, non-source region. In the 60 keV window ^{241}Am is observed, as expected, alongside incomplete-energy-deposition events from ^{133}Ba. Notably, this 60 keV energy window includes tungsten x-rays produced by the photoelectric absorption of higher-energy gamma rays in the tungsten mask. However, this tungsten capture signal is constant through time and is therefore subtracted off in the image pedestal. In the 122 keV window we see ^{57}Co while above 200 keV only ^{133}Ba is visible. Directional spectral were queried from the datacube along directions noted by the dashed boxes. ^{133}Ba, ^{57}Co and ^{241}Am gamma-ray spectra are clearly separated with little source-to-source crosstalk. This clean separation of directional gamma-ray spectra is particularly important when measuring multiple sources with similar gamma-ray emissions.

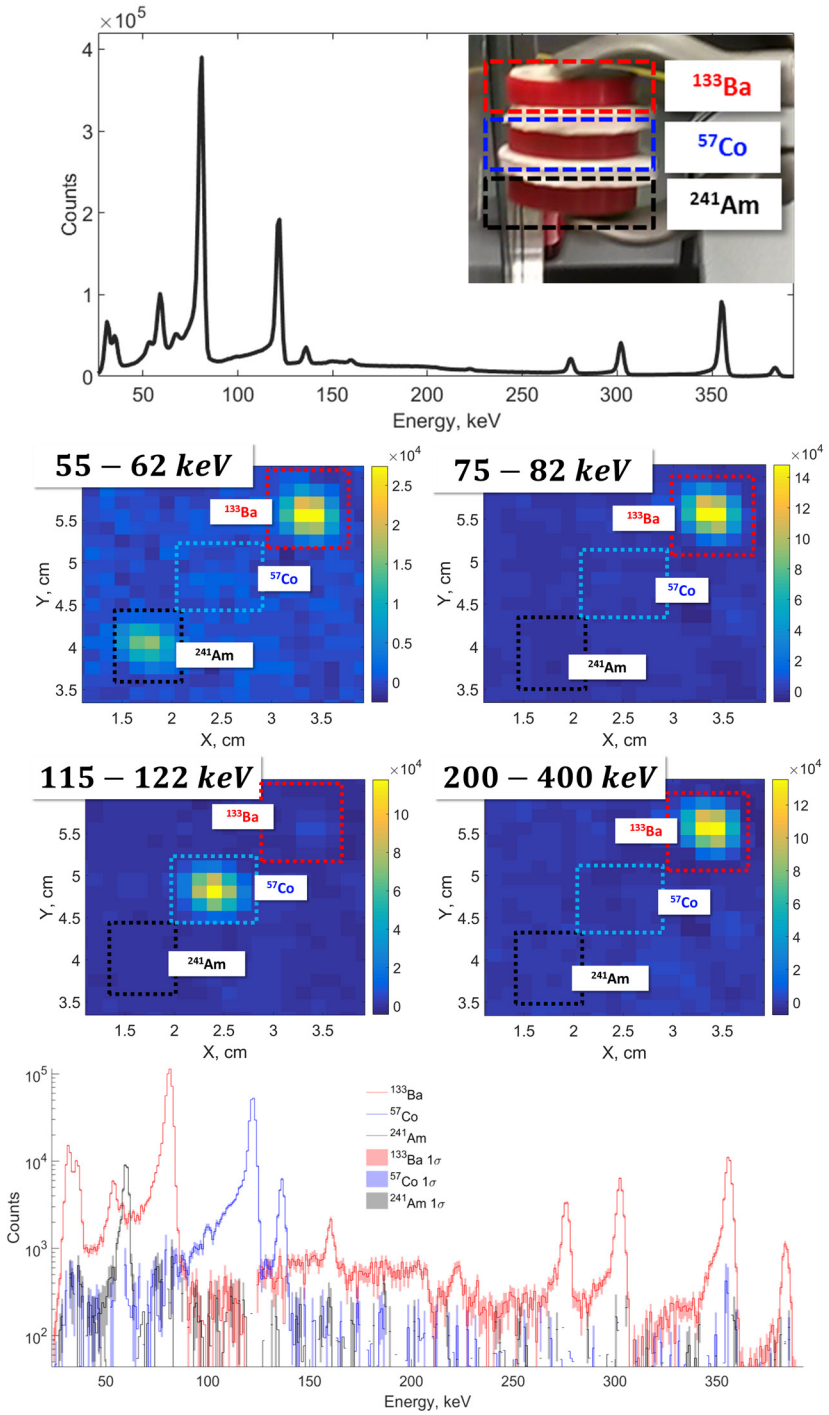

Figure 9.10: (Top) Angularly integrated gamma-ray spectra of three check sources. The relative source layout is shown in the inset figure. Relative source separations are roughly 1 cm. (Middle) Energy-specific, gamma-ray reconstructions. True source locations are shown by dashed boxes. Note sources become relatively more intense in energy windows about their gamma-ray emissions. (Bottom) Directional spectra in the direction of dashed-boxes. Incomplete-energy-deposition events are seen from the ^{133}Ba direction. Object spectra are clearly separated with little spectral-crosstalk.

9.3 Conclusions

The high-resolution, time-encoded CdZnTe imaging system developed by *Brown* is particularly effective at imaging unknown plutonium distributions. Detailed, high-resolution reconstructions of high-burnup plutonium objects were generated using the 60 keV emission of ^{241}Am. Imaging resolution better than 1 cm^2 was experimentally demonstrated on MOX pins while the relationship between source magnification was clearly demonstrated. Low-burnup plutonium objects, with little ^{241}Am, were imaged using predominately x-rays and high-energy, plutonium gamma rays. Quantitative analysis of time-encoded reconstructions was experimentally demonstrated using two equal activity plutonium triangles. Bootstrapped estimates of individual triangle activities agreed to within statistical uncertainties from reconstruction. Directional spectra from three check sources, with separations of roughly 1 cm, were experimentally demonstrated with little-to-none spectral-crosstalk. High-resolution, directional spectra can be potentially combined with FRAM-based isotopic analysis to generate spatially resolved maps of SNM isotopics.

CHAPTER X

Summary and Future Work

10.1 Summary

Overall, large-volume, pixelated CdZnTe imaging spectrometers offer high-performance, room-temperature radiation detection. The high-energy resolution of direct-attached, digital readout enables CdZnTe to approach some problems traditionally limited to HPGe, such as estimating plutonium and uranium isotopics. Digital CdZnTe spectra were processed using the commercial software FRAM v5.2 to estimate both plutonium and uranium isotopics. Uranium isotopics were accurately estimated across a wide range of material grades, while plutonium estimates suffered from substantial measurement uncertainties. H3D CdZnTe spectra were also successfully processed using FRAM v5.2 to estimate uranium isotopics without the use of standards.

CdZnTe imaging capabilities were leveraged in a variety of ways. New high-resolution, TEI-based techniques developed by *Brown* were applied to various plutonium samples. Images with better than 1 cm^2 resolution were generated by leveraging the bright 60 keV emissions of ^{241}Am in high-burnup samples and x-rays in low-burnup or shielded samples. Imaging enables estimation of directional spectra, simplifying complex, multi-source problems into smaller, tractable problems for shielding characterization algorithms. Estimation of directional spectra and associated directional shielding using Compton imaging was experimentally demonstrated for ^{133}Ba sources.

Directional shielding characterization was extended to low-energy gamma rays using simulated ^{235}U sources where both shielding and absolute source activity were estimated. Air was analyzed as a low-density, low-atomic-number shield and used to estimate source-to-detector standoffs at distances exceeding half a kilometer. Source standoff was then used to estimate unknown source activity to within a factor of two for a calculated activity correction factor exceeding 10^{10}. Skyshine air-scatter was also used to localize a heavily collimated source without a direct line-of-sight.

Mobile, airborne measurements of strong gamma-ray sources were conducted using a helicopter and commercial CdZnTe detectors. Sources were localized using both $1/r^2$ and imaging information. Imaging-based source localization was found to be relatively more robust than $1/r^2$-based localization for unpenalized reconstructions without samples near the source location.

Fast neutrons elastically scattering off the CdZnTe array were detected using new, low-noise digital ASICs. The pixel-by-pixel spatial distribution of elastic scatters was used to localize a fast neutron source in 1-D, azimuthal space using a maximum-likelihood estimator and a naïve system model.

Energetic, neutron-induced gamma rays from neutron interactions in object shielding were detected using new, high-dynamic-range ASICs. Neutron-induced gamma rays were Compton imaged in a toy problem consisting of PVC and polyethylene, illustrating that CdZnTe systems can generate spatially-resolved maps of qualitative shielding isotopics. Combined, these novel algorithms and measurements illustrate several new ways CdZnTe imaging spectrometers can be used to characterize unknown spaces.

10.2 Future Work

This work only scratches the surface of the diverse problem space where large-volume, 3-D, pixelated CdZnTe detectors can be applied. Several remaining problems

that can be approached using high-energy-resolution, room-temperature, gamma-ray imaging spectrometers include utilizing scattered flux and pulsed neutron sources.

10.2.1 Source Detection Using Scattered Flux

Radiation detection and characterization follows a problem hierarchy. First, to characterize a radioactive object, the object must be 'detected' as being radioactive. This focused characterization problems, omitting the detection process, using CdZnTe detectors. However, imaging CdZnTe detectors may offer improved detection capabilities of heavily shielded sources. Previous research focusing on improvements in radioactive source detection using Compton imaging were inconclusive, suggesting imaging information offered little value [53]. However this work focused on unshielded gamma-ray sources, where the energy spectra contained strong, informative photopeaks. Given sufficient, low-atomic-number shielding, where Compton scatter is the dominant interaction, very little uncollided, photopeak gamma-ray flux should be detected. In these scatter-dominated problems, such as detecting a source through a substantial areal thickness of air or plastic, the photopeak information contained in gamma-ray spectra about the presence of a source is degraded through Compton-downscatter. Furthermore, the resulting, downscattered flux is similar in shape to that of the gamma-ray background. This increase in the spectral similarity between down-scattered source photons and background further complicates problems where background count rates are poorly known.

However, as seen in the ^{192}Ir measurements of Chapter IV, downscattered gamma rays still contain some directional information. In the most extreme case, skyshine, a source could be clearly localized with little-to-no detectable photopeak flux. Further thought should be given to whether imaging spectrometers can leverage events with degraded spectral, but reasonable directional, information to more quickly detect sources in thick, downscatter-dominated problems.

10.2.2 Imaging Time-Dependent Neutron-Induced Gamma Rays

The neutron lifetime, the time between emission and absorption or leakage, in hydrogenous objects can extend out to 10's of μs [153]. This lifetime is long compared to the roughly 10's of ns coincidence timing resolution of CdZnTe detectors [154]. Therefore the time-dependent, spatially-resolved slowing down and eventual absorption of neutrons in some unknown object can be measured. This explicitly expands on the work presented in Chapter VII where now $D_i(\theta, \phi, t)$ is measured instead of $D_i(\theta, \phi)$.

Pulsed neutron generators, which emit bright packets of fast neutrons, are ideal for combined temporally-and-spatially-resolved measurements. A toy problem to experimentally demonstrate capabilities is posed as follows. Three commonly available plastics, polyethylene (C_2H_4), borated-polyethylene with 5% boron by weight, and PVC (C_2H_3Cl) exhibit drastically different neutron lifetime properties. Simulated neutron lifetimes from MCNP-Polimi for 20 cm^3 cubes excited using a DT neutron source are shown in Fig. 10.1. Detection and imaging of hydrogen and chlorine capture gamma rays was experimentally demonstrated in Chapter VII while imaging the low-energy, 478 keV gamma ray from boron capture should be trivial. Additionally, the differences in neutron lifetimes between these materials is well within the temporal resolving time of CdZnTe systems. Therefore, combined spatially and temporally-resolved mapping of neutron-induced gamma rays should be feasible using Compton imaging.

Experimentally measured neutron capture lifetimes offer useful object information. For example, measured neutron lifetimes are sensitive to total system moderation. Alternatively, in systems with special nuclear materials, the temporal neutron density is sensitive to object multiplication. Therefore, temporally-and-spatially-resolved neutron interaction densities, estimated using neutron-induced gamma rays, can provide unique information on unknown objects.

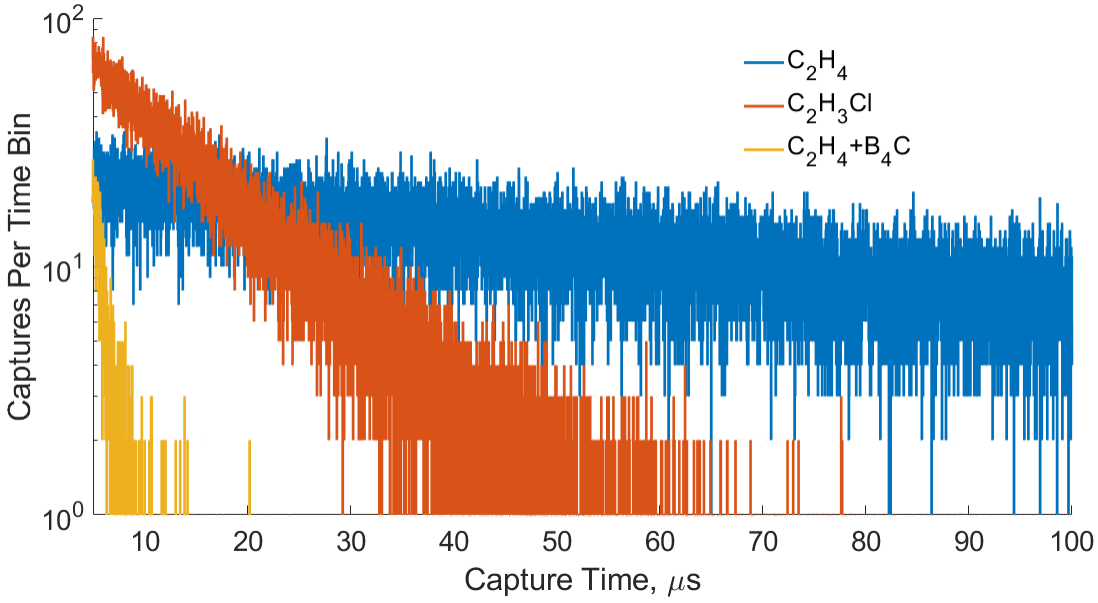

Figure 10.1: MCNPX-PoliMi time between neutron birth and capture in 20 cm cubes of polyethylene, PVC and borated polyethylene.

10.2.3 Analyses Leveraging Improved CdZnTe Systems

3-D, position-sensitive, CdZnTe detector systems are constantly improving. Material quality continues to improve alongside economically viable crystal size. 4 x 4 x 1.5 cm^3 crystals are currently under investigation as shown in Fig. 10.2. These larger crystals offer potential benefits in both energy resolution and high-energy, gamma-ray detection efficiency. ASIC-based readout continues to substantially improve with each ASIC generation. The next ASIC generation offers more user-configurable options than current VAD_UMv2.2 ASICs. For example, the length of event sampling windows can be changed to potentially improve system throughput or energy resolution. Improvements in system throughput can be immediately leveraged when coded aperture imaging bright ^{241}Am emissions from plutonium. Improvements in system energy resolution will benefit applications across the board from imaging to isotopic characterization. Any of these improvements, whether from crystal quality, size or ASIC readout, will enable better information extraction in black-box problems.

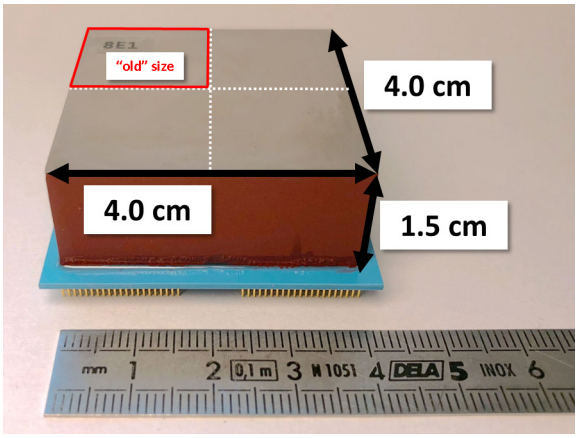

Figure 10.2: 4 x 4 x 1.5 cm^3 CdZnTe detectors from eV Products are currently under investigation. Each crystal corresponds to the volume of four CdZnTe crystals used in this work and is instrumented with a 22 x 22 array of anodes. Base image courtesy of Yuefeng Zhu.

BIBLIOGRAPHY

BIBLIOGRAPHY

[1] E. Goldfinch, "Containers for Packaging of Solid and Intermediate Level Radioactive Wastes," tech. rep., IAEA, Vienna, Austria, 1993.

[2] "UK Strategy for the Management of Solid Low Level Waste from the Nuclear Industry," tech. rep., Department of Energy and Climate Change, London, England, 2016.

[3] "10 CFR 74: Material Control and Accounting of Special Nuclear Material," tech. rep., US NRC, Rockville, MD, 2018.

[4] W. D. Ruther, T. Wang, and C. Hayden, "Uranium Enrichment Measurements without Calibration using Gamma Rays Above 100 keV," in *Symposium on International Safeguards; Verfication and Nuclear Material Security*, 2001.

[5] R. Berndt, E. Franke, and P. Mortreau, "^{235}U enrichment or UF_6 mass determination on UF_6 cylinders with non-destructive analysis methods," *Nuclear Instruments and Methods in Physics Research A*, vol. 612, no. 2, pp. 309–319, 2010.

[6] J. Yan and A. Glaser, "Nuclear Warhead Verification: A Review of Attribute and Template Systems," *Science & Global Security*, vol. 23, pp. 157–170, 2015.

[7] "A Framework Document with Terms and Definitions, Principles, and Good Practices: Principles for Nuclear Disarmament Verification," tech. rep., International Partnership for Nuclear Disarmament Verification, 2017.

[8] C. A. Curling and A. Lodge, "Review of Radioisotopes as Radiological Weapons," tech. rep., Office of The Surgeon General, Falls Church, VA, 2016.

[9] R. Maxwell, R. W. Paine, T. Shea, H. Mitchell, and E. Ballinger, "Evaluation of Radioactive Fall-Out," tech. rep., Defense Nuclear Agency, Washington, D.C., 1955.

[10] S. Glasstone, *The Effects of Nuclear Weapons*. Washington, D.C.: United States Atomic Energy Comission, 1964.

[11] A. Sharon, I. Halevy, D. Sattinger, Z. Berenstein, R. Neuman, P. Banaim, M. Pinhas, and I. Yaar, "Ground deposition pattern of an explosive radiological dispersal device (RDD)," in *Nuclear Forensices and Security*, 2014.

[12] "Radiological Dispersal Device Playbook," tech. rep., US Department of Human Services, Washington, D.C., 2010.

[13] "Guidance for Emergency Response Dosimetry," tech. rep., National Council on Radiation Protection and Measurements, Bethesda, MA, 2017.

[14] M. Streicher, S. Brown, Y. Zhu, D. Goodman, and Z. He, "A Method to Estimate the Atomic Number and Mass Thickness of Intervening Materials in Uranium and Plutonium Gamma-Ray Spectroscopy Measurements," *IEEE Transactions on Nuclear Science*, vol. 63, no. 5, pp. 2639–2648, 2016.

[15] M. Streicher, D. Goodman, Y. Zhu, S. Brown, S. Kiff, and Z. He, "Fast Neutron Detection Using Pixelated CdZnTe Spectrometers," *IEEE Transactions on Nuclear Science*, vol. 64, no. 7, pp. 1920–1926, 2017.

[16] M. Streicher, S. Brown, Y. Zhu, D. Goodman, and Z. He, "Special Nuclear Material Characterization using Digital 3-D Position Sensitive CdZnTe Detectors and High Purity Germanium Spectrometers," *IEEE Transactions on Nuclear Science*, vol. 63, no. 5, pp. 2649–2655, 2016.

[17] S. Brown, *Time-Encoded Thermal Neutron Imaging Using Large-Volume Pixelated CdZnTe Detectors*. PhD thesis, University of Michigan, 2017.

[18] G. F. Knoll, *Radiation Detection and Measurement*. Hoboken, New Jersey: Wiley, 3rd ed., 2000.

[19] R. Deslattes, E. Kessler, P. Indelicato, L. Billy, E. Lindroth, J. Coursey, J. Anton, D. Schwab, C. Chang, R. Sukumar, K. Olsen, and R. Dragoset, "X-ray Transition Energies (version 1.2)," 2005.

[20] A. H. Compton, "A Quantum Theory of the Scattering of X-Rays by Light Elements," *Physical Review*, vol. 21, no. 5, pp. 483–502, 1923.

[21] O. Klein and Y. Nishina, "The scattering of light by free electrons according to Dirac's new relativistic dynamics," *Nature*, vol. 122, p. 3072, 1928.

[22] S. F. Nowicki, S. E. Anderson, and A. M. Parsons, "6 MeV Energy Calibration and Reconstruction with Pixelated CZT Detectors using Digital Methods," *IEEE Nuclear Science Symposium Conference Record*, pp. 4697–4700, 2011.

[23] B. E. Watt, "Energy Spectrum of Neutrons from Thermal Fission of U235," *Physical Review*, vol. 87, no. 6, 1952.

[24] D. T. Reilly, N. Ensslin, H. J. Smith, and S. Kreiner, *Passive Nondestructive Assay of Nuclear Materials*. 1991.

[25] H. Vega-Carrillo, E. Manzanares-Acuna, A. Becerra-Ferreiro, and A. Carrillo-Nunez, "Neutron and gamma-ray spectra of ^{239}PuBe and ^{241}AmBe," *Applied Radiation and Isotopes*, vol. 57, pp. 167–170, 2002.

[26] J. Duderstadt and L. Hamilton, *Nuclear Reactor Analysis*. New York, New York: John Wiley & Sons, 1976.

[27] P. Dorenbos, J. M. de Hass, and C. E. van Eijk, "Non-Proportionality in the Scintillation Response and the Energy Resolution Obtainable with Scintillation Crystals," *IEEE Transactions on Nuclear Science*, vol. 42, no. 6, pp. 2190–2202, 1995.

[28] Ortec, "Micro-Detective: Ultra-Light, High-Fidelity Hand-Held Radioisotope Identifier."

[29] D. S. McGregor and H. Hermon, "Room-temperature compound semiconductor radiation detectors," *Nuclear Instruments and Methods in Physics Research A*, vol. 395, pp. 101–124, 1997.

[30] M. W. Streicher, *Applications of Digitized 3-D Position-Sensitive CdZnTe Spectrometers for National Security and Nuclear Nonproliferation*. PhD thesis, University of Michigan, 2017.

[31] W. Shockley, "Currents to Conductors Induced by a Moving Point Charge," *Journal of Applied Physics*, vol. 9, pp. 635–636, 1938.

[32] S. Ramo, "Currents Induced by Electron Motion," *Proc. of I.R.E*, 1939.

[33] Z. He, "Review of the Shockley-Ramo theorem and its application in semiconductor gamma-ray detectors," *Nuclear Instruments and Methods in Physics Research A*, vol. 463, pp. 250–267, 2001.

[34] Y. Eisen and A. Shor, "CdTe and CdZnTe materials for room-temperature X-ray and gamma ray detectors," *Journal of Crystal Growth*, vol. 184, pp. 1302–1312, 1998.

[35] D. S. McGregor, R. A. Rojeski, Z. He, D. K. Wehe, M. Driver, and M. Blakely, "Geometrically weighted semiconductor Frisch grid radiation spectrometers," *Nuclear Instruments and Methods in Physics Research A*, vol. 422, pp. 164–168, 1999.

[36] P. Luke, "Unipolar Charge Sensing with Coplanar Electrodes-Application to Semiconductor Detectors," *IEEE Transactions on Nuclear Science*, vol. 42, no. 4, pp. 207–213, 1995.

[37] H. Barrett, J. D. Eskin, and H. Barber, "Charge Transport in Arrays of Semiconductor Gamma-Ray Detectors," *Physical Review Letters*, vol. 75, no. 1, pp. 156–159, 1995.

[38] F. Zhang, Z. He, D. Xu, G. F. Knoll, D. K. Wehe, and J. E. Berry, "Improved Resolution for 3-D Position Sensitive CdZnTe Spectrometers," *IEEE Transactions on Nuclear Science*, vol. 51, no. 5, pp. 2427–2431, 2004.

[39] Z. He, G. F. Knoll, D. K. Wehe, R. Rojeski, and C. H. Mastraneg, "1-D position sensitive single carrier semiconductor detectors," *Nuclear Instruments and Methods in Physics Research A*, vol. 380, pp. 228–231, 1996.

[40] Y. Zhu, M. Streicher, J. Xia, and Z. He, "Energy Resolution Improvement and High-Energy Photon Detection in CdZnTe Spectrometers with Second Generation Digital Electronics and Reduced Preamplifier Trace Length," *submitted*, 2018.

[41] S. Gottesman and E. Fenimore, "New family of binary arrays for coded aperture imaging," *Applied Optics*, vol. 28, no. 20, pp. 4344–4352, 1989.

[42] C. E. Lehner, Z. He, and F. Zhang, "4π Compton Imaging Using a 3-D Position-Sensitive CdZnTe Detector Via Weighted List-Mode Maximum Likelihood," *IEEE Transactions on Nuclear Science*, vol. 51, no. 4, pp. 1618–1624, 2004.

[43] J. Chu, M. Streicher, J. A. Fessler, and Z. He, "Unbiased Filtered Back-Projection in 4π Compton Imaging with 3D Position Sensitive Detectors," *IEEE Transactions on Nuclear Science*, vol. 63, no. 6, pp. 2750–2756, 2016.

[44] M. Hamel, *A Stochastic Imaging Technique for Spatio-Spectral Characterization of Special Nuclear Material*. PhD thesis, University of Michigan, 2017.

[45] L. Sheep and Y. Vardi, "Maximum Likelihood Reconstruction for Emision Tomography," *IEEE Transactions on Medical Imaging*, vol. 1, no. 2, pp. 113–122, 1982.

[46] W. Wang, *Techniques and Applications of Compton Imaging for Position-Sensitive Gamma-Ray Detectors*. PhD thesis, University of Michigan, 2011.

[47] H. Barret, T. White, and L. Parra, "List-mode likelihood," *Journal of the Optical Society of America A*, vol. 14, no. 11, pp. 2914–2923, 1997.

[48] S. Wilderman, N. Clinthorne, J. Fessler, and W. Rogers, "List-Mode Maximum Likelihood Reconstruction of Compton Scatter Camera Images in Nuclear Medicine," *IEEE Nuclear Science Symposium Conference Record*, vol. 3, pp. 1716–1720, 1998.

[49] L. Lucy, "An iterative technique for the rectification of observed distributions," *The Astronomical Journal*, vol. 79, no. 6, pp. 745–754, 1974.

[50] W. H. Richardson, "Bayesian-Based Iterative Method of Image Restoration," *Journal of the Optical Society of America*, vol. 62, no. 1, pp. 55–59, 1972.

[51] E. Veklerov, J. Llacer, and E. Hoffman, "MLE Reconstruction of a Brain Phanton using a Monte Carlo Transition Matrix and Statistical Stopping Rule," *IEEE Transactions on Nuclear Science*, vol. 35, no. 1, pp. 603–607, 1988.

[52] J. Llacer and E. Veklerov, "Feasible Images and Practical Stopping Rules for Iterative Algorithms in Emission Tomography," *IEEE Transactions on Medical Imaging*, vol. 8, no. 2, pp. 186–193, 1989.

[53] C. Wahl, *Imaging, Detection, and Identification Algorithms for Position Sensitive Gamma-Ray Detectors*. PhD thesis, University of Michigan, 2011.

[54] B. Yu, S. Brown, Z. He, and J. Cheng, "Application of Chambolle-Pock Algorithm on Penalized Gamma-ray Energy-Imaging Integrated Deconvolution," in *IEEE Nuclear Science Symposium and Medical Imaging Conference*, 2015.

[55] J. Chu, *Advanced Imaging Algorithms with Position-Sensitive Gamma-Ray Detectors*. PhD thesis, University of Michigan, 2018.

[56] K. Vetter, D. Chivers, B. Plimley, A. Coffer, T. Aucott, and Q. Looker, "First demonstration of electron-tracking based Compton imaging in solid-state detectors," *Nuclear Instruments and Methods in Physics Research A*, vol. 652, pp. 599–601, 2011.

[57] A. Takada, K. Hattori, H. Kubo, K. Miuchi, T. Nagayoshi, H. Nishimura, Y. Okada, R. Orito, H. Sekiya, A. Tada, and T. Tanimori, "Development of an advanced Compton camera with gaseous TPC and scintillator," *Nuclear Instruments and Methods in Physics Research A*, vol. 546, pp. 258–262, 2005.

[58] C. G. Wahl, W. R. Kaye, W. Wang, F. Zhang, J. M. Jaworski, A. King, Y. A. Boucher, and Z. He, "The Polaris-H imaging spectrometer," *Nuclear Instruments and Methods in Physics Research A*, vol. 784, pp. 377–381, 2015.

[59] W. R. Kaye, N. D. Bennett, C. G. Wahl, Z. He, and W. Wang, "Gamma-Ray Source Location by Attenuation Measurements," *IEEE Nuclear Science Symposium and Medical Imaging Conference*, pp. 1294–1298, 2007.

[60] S. Mukhopadhyay, R. Maurer, R. Wolff, S. Mitchell, P. Guss, and C. Trainham, "Exploitation of geometric occlusion and covariance spectroscopy in a gamma sensor array," in *SPIE Proceedings on Hard X-Ray, Gamma-Ray, and Neutron Detector Physics XV*, 2013.

[61] P. Marleau, J. Brennan, E. Brubaker, M. Gerling, A. Nowack, P. Schuster, and J. Steele, "Time Encoded Fast Neutron/Gamma Imager for Large Standoff SNM Detection," *IEEE Nuclear Science Symposium and Medical Imaging Conference*, pp. 591–595, 2012.

[62] R. Byrd, "Directional Fast-Neutron Detectors," tech. rep., Los Alamos National Laboratory, Los Alamos, NM, 1992.

[63] T. M. Cannon and E. Fenimore, "Coded aperture imaging: many holes make light work," *Optical Engineering*, vol. 19, no. 3, pp. 283–289, 1980.

[64] S. Joshi, *Coded Aperture Imaging Applied to Pixelated CdZnTe detectors*. PhD thesis, University of Michigan, 2014.

[65] S. T. Brown, D. Goodman, J. Chu, B. Williams, and M. Williamson, "Time-Encoded Gamma-Ray Imaging Using a 3D-Position-Sensitive CdZnTe Detector Array," *submitted*.

[66] S. Brown, C. Wahl, W. Kaye, K. Moran, J. Sowers, J. Jaworski, F. Zhang, H. Yang, M. Streicher, B. Kitchen, T. Slatina, Y. A. Boucher, W. Wang, and Z. He, "A Compact CdZnTe Coded Aperture Imaging Spectrometer for Isotopic Characterization," in *INMM 59th Annual Meeting*, 2018.

[67] K. Amgarou, V. Paradiso, A. Patoz, F. Bonnet, J. Handley, P. Couturier, F. Becker, and N. Menaa, "A comprehensive experimental characterization of the iPIX gamma imager," *Journal of Instrumentation*, vol. 11, 2016.

[68] D. Xu, *Gamma-Ray Imaging and Polarization Measurement Using 3-D Position-Sensitive CdZnTe Detectors*. PhD thesis, Univeristy of Michigan, 2006.

[69] S. M. Horne, G. G. Thoreson, L. A. Theisen, D. J. Mitchell, L. Harding, and A. Wendy, "GADRAS-DRF 18.5 User's Manual," tech. rep., Sandia National Laboratories, Albuquerque, New Mexico, 2014.

[70] K. Moats, "An Operational Shielding Algorithm System (SAS) Software for the Analysis of Gamma Ray Spectra," tech. rep., Defence Research and Development Canada, Ottawa, Canada, 2018.

[71] D. J. Mitchell, S. M. Horne, S. O. Brien, and G. G. Thoreson, "Directional Unfolded Source Term (DUST) for Compton Cameras," tech. rep., Sandia National Laboratory, 2018.

[72] P. Peerani and A. Tomanin, "Surrogates of plutonium for detection equipment testing," *Nuclear Instruments and Methods in Physics Research A*, vol. 654, pp. 613–620, 2011.

[73] M. Frank, "Plutonium Radiation Surrogate," 2010.

[74] D. Goodman, M. Streicher, Y. Zhu, and Z. He, "Identification of Intervening Materials In Gamma-ray Spectroscopy Measurements Using Angularly Deconvolved Spectra With Multiple Sources in the Field-of-View," *IEEE Transactions on Nuclear Science*, vol. 65, no. 3, 2018.

[75] B. Efron and R. Tibshirani, *An Introduction to the Bootstrap*. New York, New York: CRC Press, 1998.

[76] D. R. Haynor and S. D. Woods, "Resampling Estimates of Precision in Emission Tomography," *IEEE Transactions on Medical Imaging*, vol. 8, no. 4, pp. 337–343, 1989.

[77] D. Goodman, S. Brown, J. Chu, and Z. He, "Angular Detection and Shielding Characterization of Simulated ^{235}U Using Time Encoded Imaging and 3D Position Sensitive CdZnTe Detectors," in *IEEE Room Temperature Semiconductor Detectors Conference Record*, 2017.

[78] K. P. Ziock, N. Madden, E. Hull, W. Craig, T. Lavietes, and C. Cork, "A Germanium-Based Coded Aperture Imager," *IEEE Transactions on Nuclear Science*, vol. 49, no. 4, pp. 1737–1742, 2002.

[79] M. Streicher, Y. Zhu, F. Zhang, Y. A. Boucher, C. G. Wahl, H. Yang, and Z. He, "A Portable 2 x 2 Digital 3D CZT Imaging Spectrometer System," in *IEEE Nuclear Science Symposium and Medical Imaging Conference*, 2014.

[80] Y. Zhu, S. E. Anderson, and Z. He, "Sub-pixel Position Sensing for Pixelated, 3-D Position Sensitive, Wide Band-Gap, Semiconductor, Gamma-Ray Detectors," *IEEE Transactions on Nuclear Science*, vol. 58, no. 3, pp. 1400–1409, 2011.

[81] D. Goodman, J. Xia, D. L. Chichester, S. M. Watson, and Z. He, "Single View, Ultra-Far-Field Bare Source Detection and Absolute 3-D Localization Using HPGe and CdZnTe Detectors," *submitted*.

[82] C. A. Jayachandran, "Calculated effective atomic number and Kerma values for tissue-equivalent and dosimetry materials," *Phys. Med. Biol.*, vol. 16, no. 4, pp. 617–623, 1971.

[83] M. Kitazume, "A Simple Calculation for Air-Scattered Gamma-Rays," *Journal of Nuclear Science and Technology*, vol. 5, no. 9, pp. 464–471, 1968.

[84] M. Kitazume, "Gamma-Ray Scattering from Point Sources by Infinite Plane Surfaces," *Journal of Nuclear Science and Technology*, vol. 5, no. 3, pp. 98–103, 1968.

[85] G. G. Thoreson, D. J. Mitchell, L. A. Theisen, and L. T. Harding, "Environment Scattering in GADRAS," tech. rep., Sandia National Laboratory, Albuquerque, New Mexico, 2013.

[86] G. G. Thoreson, D. J. Mitchell, and L. T. Harding, "Simulating Higher-Dimensional Geometries in GADRAS Using Approximate One-Dimensional Solutions," tech. rep., 2013.

[87] T. Goorley, M. James, T. Booth, F. Brown, J. Bull, L. J. Cox, J. Durkee, J. Elson, M. Fensin, R. A. Forster, J. Hendricks, H. G. Hughes, R. Johns, B. Kiedrowski, S. Mashnik, G. Mckinney, D. Pelowitz, R. Prael, J. Sweezy, L. Waters, and T. Zukaitis, "Initial MCNP6 Release Overview," *Nuclear Technology*, vol. 180, no. 3, pp. 298–315, 2012.

[88] R. J. McConn, C. J. Gesh, R. T. Pagh, R. A. Rucker, and R. G. Williams, "Compendium of Material Composition Data for Radiation Transport Modeling," tech. rep., Pacific Northwest National Laboratory, 2011.

[89] M. Berger, J. Hubbell, S. Seltzer, J. Chang, J. Coursey, R. Sukumar, D. Zucker, and K. Olsen, "XCOM: Photon Cross Section Database (version 1.5)," 2010.

[90] D. L. Chichester, Personal communication, 2017.

[91] "Handbook for Responding to a Radiological Dispersal Device: First Responder's Guide-the First 12 Hours," tech. rep., Conference of Radiaton Control Program Directors Inc., 2006.

[92] L. Spencer, A. Chilton, and C. Eisenhauer, "Structure Shielding Against Fallout Gamma Rays From Nuclear Detonations," tech. rep., National Bureau of Standards, Gaithersburg, MD, 1980.

[93] R. T. Kouzes, J. H. Ely, E. L. Flumerfelt, W. K. Hensley, K. R. McCormick, and E. R. Siciliano, "Skyshine Interference with Radiation Detection Systems," in *IEEE Nuclear Science Symposium*, pp. 1259–1260, 2008.

[94] R. Tayama, K. Wakasugi, I. Kawanaka, Y. Kadota, and Y. Murakami, "Verification of BWR Turbine Skyshine Dose with the MCNP5 Code Based on an Experiment Made at SHIMANE Nuclear Power Station," *Journal of Power and Energy Systems*, vol. 4, no. 1, pp. 54–61, 2010.

[95] L. Lovborg, L. Botter-Jensen, P. Kirkegaard, and E. Christiansen, "Monitoring of Natural Soil Radioactivity with Portable Gamma-Ray Spectrometers," *Nuclear Instruments and Methods*, vol. 167, pp. 341–348, 1979.

[96] H3D, "H400: Gamma-Ray Imaging Spectrometer."

[97] A. Haefner, R. Barnowski, P. Luke, M. Amman, and K. Vetter, "Handheld real-time volumetric 3-D gamma-ray imaging," *Nuclear Instrument and Methods in Physics Research A*, vol. 857, pp. 42–49, 2017.

[98] C. Lyons and D. Colton, "Aerial Measuring System in Japan," *Health Physics*, vol. 102, no. 5, pp. 509–515, 2012.

[99] S. Okuyama, T. Torii, A. Suzuki, and M. Shibuya, "A Remote Radiation Monitoring System Using an Autonomous Unmanned Helicopter for Nuclear Emergencies," *Journal of Nuclear Science and Technology*, vol. 45, no. 5, pp. 414–416, 2014.

[100] C. M. Chen, L. E. Sinclair, R. Fortin, M. Coyle, and C. Samson, "In-flight performance of the Advanced Radiation Detector for UAV Operations (ARDUO)," *Nuclear Instruments and Methods in Physics Research A*, 2018.

[101] M. Lee, M. Hanczor, J. Chu, Z. He, N. Michael, and R. Whittaker, "3-D Volumetric Gamma-ray Imaging and Source Localization with a Mobile Robot," in *Waste Management Symposia*, 2018.

[102] S. Webber, "Emerging Nuclear Detection Technologies in the Department of Defense," in *Conference on Ionizing Radiation Measurements and Standards*, 2018.

[103] H3D, "A400: Handheld Radiation Identifer."

[104] R. Barnowski, A. Haefner, L. Mihailescu, and K. Vetter, "Scene data fusion: Real-time standoff volumetric gamma-ray imaging," *Nuclear Instruments and Methods in Physics Research A*, vol. 800, pp. 65–69, 2015.

[105] "Fission product yields: IAEA-NDS," tech. rep., IAEA, Vienna, Austria, 1996.

[106] "Aerial Measuring System (AMS)," tech. rep., NSTec, Las Vegas, NV, 2014.

[107] D. Hellfeld, T. Joshi, M. Bandstra, R. Cooper, and K. Vetter, "Additive Point Source Localization," *IEEE Transactions on Nuclear Science (in preparation).*

[108] DJI, "Spreading Wings S1000+," 2018.

[109] W. Hess, D. Kohler, H. Rapp, and D. Andor, "Real-Time Loop Closure in 2D LIDAR SLAM," in *2016 IEEE International Conference on Robotics and Automation*, pp. 1271–1278, 2016.

[110] J. M. Jaworski, *Compton Imaging Algorithms for Position-Sensitive Gamma-Ray Detectors in the Presence of Motion.* PhD thesis, University of Michigan, 2013.

[111] E. L. Haines and A. B. Whitehead, "Pulse height defect and energy dispersion in semiconductor detectors," *Review of Scientific Instruments*, vol. 37, no. 2, pp. 190–194, 1966.

[112] Y. Zhu and Z. He, "Performance of a 2-keV Digitizer ASIC for 3-D Position-Sensitive Pixelated Semiconductor Detectors," in *IEEE Nuclear Science Symposium and Medical Imaging Conference*, pp. 4109–4112, 2012.

[113] D. Goodman, M. Streicher, Y. Zhu, S. Brown, and Z. He, "1-D Fast Neutron Source Localization Using Digital Pixelated 3-D Position-Sensitive CdZnTe Detectors," *IEEE Transactions on Nuclear Science*, vol. 64, no. 9, pp. 2531–2535, 2017.

[114] J. E. M. Goldsmith, M. D. Gerling, and J. S. Brennan, "A compact neutron scatter camera for field deployment," *Review of Scientific Instruments*, vol. 87, 2016.

[115] A. Poitrasson-Rivière, M. C. Hamel, J. K. Polack, M. Flaska, S. D. Clarke, and S. A. Pozzi, "Dual-particle imaging system based on simultaneous detection of photon and neutron collision events," *Nuclear Instruments and Methods in Physics Research A*, vol. 760, pp. 40–45, 2014.

[116] P. A. Hausladen, M. A. Blackston, E. Brubaker, D. L. Chichester, P. Marleau, and R. J. Newby, "Fast-Neutron Coded-Aperture Imaging of Special Nuclear Material Configurations," in *Institute of Nuclear Materials Management 53rd Annual Meeting*, 2012.

[117] S. Agostinelli, "GEANT4-a simulation toolkit," *Nuclear Instruments and Methods in Physics Research A*, vol. 506, no. 3, pp. 250–303, 2003.

[118] H3D, "J6400 High-Energy High-Flux Spectrometer."

[119] J. Coursey, D. Schwab, J. Tsai, and R. Dragoset, "Atomic Weights and Isotopic Compositions (version 4.1)," 2015.

[120] A. A. Sonzogni, "NuDat 2.0: Nuclear Structure and Decay Data on the Internet," in *AIP Conference Proceedings*, vol. 769, pp. 574–577, 2005.

[121] D. Goodman, J. Xia, and H. Zhong, "Qualitative Measurement of Spatial Shielding Isotopics via Compton Imaging Neutron-Induced Gamma Rays using 3-D CdZnTe Detectors," *submitted*.

[122] Y. Zhu, *Digital Signal Processing Methods for Pixelated 3-D Position Sensitive Room-Temperature Semiconductor Detectors*. PhD thesis, University of Michigan, 2012.

[123] S. E. Boggs and P. Jean, "Event reconstruction in high resolution Compton telescopes," *Astron. Astrophys. Suppl. Ser.*, vol. 145, pp. 311–321, 2000.

[124] Y. A. Boucher, F. Zhang, W. Kaye, and Z. He, "Measurements of Gamma Rays above 3 MeV using 3D Position-Sensitive 20x20x15 mm^3 CdZnTe Detectors," in *IEEE Nuclear Science Symposium*, pp. 4540–4544, 2011.

[125] Y. A. Boucher, *Analysis of Cadmium Zinc Telluride Detector Performance and Characteristics for Applications in Gamma-Ray Imaging Spectrometers*. PhD thesis, University of Michigan, 2013.

[126] H. Chen, H. Chen-Mayer, D. Turkoglu, R. Benjamin, E. Draeger, and J. Polf, "Spectroscopic Compton Imaging of Prompt Gamma Emissions at the MeV Energy Range," *Journal of Radioanalytical and Nuclear Chemistry*, vol. 318, no. 1, pp. 241–246, 2018.

[127] S. A. Pozzi, E. Padovani, and M. Marseguerra, "MCNP-PoliMi: a Monte-Carlo code for correlation measurements," *Nuclear Instruments and Methods in Physics Research A*, vol. 513, pp. 550–558, 2003.

[128] A. J. Caffrey, "PINS Spectrum Identification Guide," tech. rep., Idaho National Laboratory, Idaho Falls, Idaho, 2012.

[129] A. J. Caffrey, J. D. Cole, R. J. Gehrke, and R. C. Greenwood, "Chemical warfare agent and high explosive identification by spectroscopy of neutron-induced gamma rays," *IEEE Transactions on Nuclear Science*, vol. 39, no. 5, pp. 1422–1426, 1992.

[130] D. L. Chichester, M. Lemchak, and J. D. Simpson, "The API 120: A portable neutron generator for the associated particle technique," *Nuclear Instruments and Methods in Physics Research B*, vol. 241, pp. 753–758, 2005.

[131] S. Fetter, V. A. Frolov, M. Miller, R. Mozley, O. F. Prilutsky, S. N. Rodionov, and R. Z. Sagdeev, "Detecting Nuclear Warheads," *Science & Global Security*, vol. 1, pp. 225–302, 1990.

[132] D. Goodman, J. Xia, J. Sanders, and Z. He, "FRAM v5.2 estimation of plutonium and uranium isotopics using digitized 3-D position-sensitive CdZnTe detectors," *Nuclear Instruments and Methods in Physics Research A*, 2018.

[133] ORTEC, "PROFILE S and C Series: P-type Semi-planar and Coaxial HPGe Detectors."

[134] D. T. Vo and P. A. Russo, "PC / FRAM plutonium isotopic analysis of CdTe gamma-ray spectra," *Nuclear Instruments and Methods in Physics Research A*, vol. 486, pp. 813–824, 2002.

[135] A. S. Hoover, R. Winkler, M. W. Rabin, D. T. Vo, J. N. Ullom, D. A. Bennett, W. B. Doriese, J. W. Fowler, R. D. Horansky, D. R. Schmidt, L. R. Vale, and K. Schaffer, "Determination of Plutonium Isotopic Content by Microcalorimeter Gamma-Ray Spectroscopy," *IEEE Transactions on Nuclear Science*, vol. 60, no. 2, pp. 681–688, 2013.

[136] D. Vo, "New Capabilities in FRAM v.6," in *INMM 58th Annual Meeting*, 2017.

[137] S. Walston, J. Burch, M. Cowan, G. Guethlein, P. Kerr, D. Mcavoy, L. Nakae, M. Prasad, G. Slavik, and N. Snyderman, "Benchmark Measurements of the BeRP Ball in Various Reflectors," tech. rep., Lawerence Livermore National Laboratory, 2014.

[138] R. B. Kidman, "Reckoning THOR," tech. rep., Los Alamos National Laboratory, 1981.

[139] J. A. Cantrell, "Uranium Enrichment Standards of the Y-12 Nuclear Detection and Sensor Testing Center," in *Proc. 52nd Annu. INMM Meeting*, 2012.

[140] D. L. Chichester, "Properties of Nuclear Fuel Used in Tests with the LLNL Gamma-Ray Mirror in September 2014," tech. rep., Idaho National Laboratory, 2014.

[141] D. L. Chichester, S. A. Pozzi, J. L. Dolan, M. Flaska, J. T. Johnson, E. H. Seabury, and E. M. Gantz, "Neutron Emission Characteristics of Two Mixed-Oxide Fuels: Simulations and Initial Experiments," tech. rep., Idaho National Laboratory, 2009.

[142] "CBNM Nuclear Reference Material 271," tech. rep., JRC, Geel, Belgium, 1989.

[143] W. Hsue, "SRP Isotopic Standards," tech. rep., Los Alamos National Laboratory, Los Alamos, NM, 1989.

[144] R. Redding, A. Mozahyev, J. Benz, and J. Stave, "Characterization of the Plutonium Sealed Source PSS-002," tech. rep., Pacific Northwest National Laboratory, Richland, Washington, 2013.

[145] T. Sampson, S. Hsue, J. Parker, S. Johnson, and D. F. Bowersox, "The Deterimination of Plutonium Isotopic Composition By Gamma-Ray Spectroscopy," *Nuclear Instruments and Methods in Physics Research A*, vol. 193, pp. 177–183, 1982.

[146] K. Koral, L. Rogers, and G. Knoll, "Digital Tomographic Imaging with Time-Modulated Pseudorandom Coded Aperture and Anger Camera," *Journal of Nuclear Medicine*, vol. 16, pp. 402–413, 1975.

[147] J. Giessen, M. Viergever, C. Graaf, and H. Dane, "Time-Coded Aperture Tomography: Experimental Results," *IEEE Transactions on Medical Imaging*, vol. 5, no. 4, pp. 222–228, 1986.

[148] B. R. Kowash, D. K. Wehe, and J. A. Fessler, "A rotating modulation imager for locating mid-range point sources," *Nuclear Instruments and Methods in Physics Research A*, vol. 602, no. 2, pp. 477–483, 2009.

[149] D. Goodman, J. Xia, S. Brown, D. L. Chichester, and Z. He, "High Resolution Time-Encoded Imaging of Plutonium and MOX using 3-D Position-Sensitive CdZnTe Detectors," in *IEEE Nuclear Science Symposium and Medical Imaging Conference*, 2018.

[150] S. C. Park, M. K. Park, and M. G. Kang, "Super-resolution image reconstruction: A technical overview," *IEEE Signal Processing Magazine*, vol. 20, no. 5, pp. 21–36, 2003.

[151] R. Accorsi, F. Gasparini, and R. C. Lanza, "Optimal coded aperture patterns for improved SNR in nuclear medicine imaging," *Nuclear Instruments and Methods in Physics Research A*, no. 474, pp. 273–284, 2001.

[152] M. C. Fleenor, M. A. Blackston, and K. P. Ziock, "Correlated statistical uncertainties in coded-aperture imaging," *Nuclear Instruments and Methods in Physics Research A*, vol. 784, pp. 370–376, 2015.

[153] C. Belanger-Champagne, H. Vainionpa, P. Peura, H. Toivonen, P. Eerola, and P. Dendooven, "Design of a novel instrument for active neutron interrogation of artillery shells," *PLoS ONE*, vol. 12, no. 12, 2017.

[154] L. Meng and Z. He, "Exploring the limiting timing resolution for large volume CZT detectors with waveform analysis," *Nuclear Instruments and Methods in Physics Research A*, pp. 435–445, 2005.

[155] R. Todd, J. Nightingale, and D. Everett, "A proposed γ camera," *Nature*, vol. 251, no. 5471, pp. 132–134, 1974.